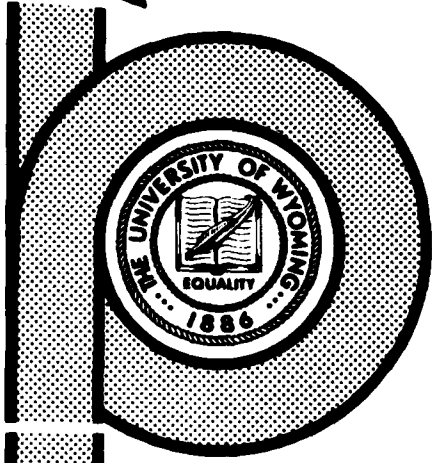


AD-A168 050

**FINITE ELEMENT MICROMECHANICS AND
MINIMECHANICS MODELING
OF A THREE-DIMENSIONAL
CARBON-CARBON COMPOSITE
MATERIAL**



David E. Walrath
Donald F. Adams

December 1985

DTIC
ELECTE
MAY 28 1986
S A D

DTIC FILE COPY

OFFICE OF NAVAL RESEARCH
ARLINGTON, VIRGINIA
ONR Contract No. N00014-77-C-0503

APPROVED FOR PUBLIC RELEASE; DISTRIBUTION UNLIMITED

86 5 27 170

COMPOSITE MATERIALS RESEARCH GROUP
DEPARTMENT of MECHANICAL ENGINEERING
University of Wyoming Laramie, Wyoming 82071

DEPARTMENT REPORT
UWME-DR-501-106-1

FINITE ELEMENT MICROMECHANICS AND MINIMECHANICS MODELING
OF A THREE-DIMENSIONAL CARBON-CARBON COMPOSITE MATERIAL

FINAL TECHNICAL REPORT

DAVID E. WALRATH
DONALD F. ADAMS

DECEMBER 1985

OFFICE OF NAVAL RESEARCH
ARLINGTON, VIRGINIA

ONR CONTRACT NO. N00014-77-C-0503

COMPOSITE MATERIALS RESEARCH GROUP
MECHANICAL ENGINEERING DEPARTMENT
UNIVERSITY OF WYOMING
LARAMIE, WYOMING 82071

APPROVED FOR PUBLIC RELEASE; DISTRIBUTION UNLIMITED

REPORT DOCUMENTATION PAGE		READ INSTRUCTIONS BEFORE COMPLETING FORM
1. REPORT NUMBER	2. GOVT ACCESSION NO. AD-A168050	3. RECIPIENT'S CATALOG NUMBER
4. TITLE (and Subtitle) Finite Element Micromechanics and Minimechanics Modeling of a Three-Dimensional Carbon-Carbon Composite Material	5. TYPE OF REPORT & PERIOD COVERED Final Technical Report September 1984-December 1985	
	6. PERFORMING ORG. REPORT NUMBER UWME-DR-501-106-1	
7. AUTHOR(s) David E. Walrath Donald F. Adams	8. CONTRACT OR GRANT NUMBER(s) N00014-77-C-0503	
	10. PROGRAM ELEMENT, PROJECT, TASK AREA & WORK UNIT NUMBERS NR 039-149	
9. PERFORMING ORGANIZATION NAME AND ADDRESS Composite Material Research Group Mechanical Engineering Department University of Wyoming, Laramie, WY 82071	12. REPORT DATE December 1985	
	13. NUMBER OF PAGES	
11. CONTROLLING OFFICE NAME AND ADDRESS Office of Naval Research Attn: Dr. L. H. Peebles, Jr. 800 N. Quincy Ave., Arlington, VA 22217	15. SECURITY CLASS. (of this report) Unclassified	
	15a. DECLASSIFICATION/DOWNGRADING SCHEDULE	
16. DISTRIBUTION STATEMENT (of this Report) Reproduction in whole or part is permitted for any purpose by the United States Government. Approved for public release, distribution unlimited.		
17. DISTRIBUTION STATEMENT (of the abstract entered in Block 20, if different from Report) Approved for public release; distribution unlimited		
18. SUPPLEMENTARY NOTES		
19. KEY WORDS (Continue on reverse side if necessary and identify by block number) Carbon-Carbon Composites Micromechanics Analysis Minimechanics Analysis		
20. ABSTRACT (Continue on reverse side if necessary and identify by block number) Emphasis of this work is to develop finite element micromechanics models to predict the thermomechanical material properties for unidirectional carbon-carbon composite materials. These properties are then used to define the fiber bundle properties in a finite element minimechanics analysis of a three-dimensional rectangular weave carbon-carbon unit cell. The objective of these analyses is to predict the mechanical properties of the three-dimensional carbon-carbon composite. Features of these analyses include		

to p. 2

fr. p. 2

capabilities to model nonlinear temperature-dependent constituent material behavior and procedures to predict damage initiation and crack propagation.

PREFACE

This final technical report summarizes work conducted as part of ONR Contract No. N00014-77-C-0503, Work Unit NR 039-149, (University of Wyoming Project No. 5-33106). Dr. L. H. Peebles, Jr. of the Office of Naval Research, Arlington, Virginia, served as the Program Technical Monitor.

Work reported in this document was performed by members of the Composite Materials Research Group within the Mechanical Engineering Department at the University of Wyoming. Mr. D. E. Walrath and Dr. D. F. Adams served as Co-Principal Investigators. Also contributing to this research effort were Messrs. J. M. Mahishi, R. L. Westberg, and G. J. Aust, graduate students in Mechanical Engineering, and K. M. Bauer, B. D. Brownlee, D. K. McCarthy, G. V. Morrison, C. E. Wyers, B. R. Miller, and R. W. Wakelee, undergraduate students in Mechanical Engineering.

Accession For	
NTIS GRA&I	<input checked="" type="checkbox"/>
DTIC TAB	<input type="checkbox"/>
Unannounced	<input type="checkbox"/>
Justification	
By _____	
Distribution/	
Availability Codes	
Dist	Avail and/or Special
A-1	



TABLE OF CONTENTS

Section	Page
1 INTRODUCTION	1
1.1 Previous Experimental	1
1.2 Summary of Present Work	2
2 PRIOR ANALYTICAL MODELS.	5
2.1 Background.	5
2.2 Levels of Analysis.	6
2.3 Micromechanics Analysis	8
2.4 Minimechanics Analyses.	9
2.4.1 Materials Science Corporation - DCAP	9
2.4.2 Science Applications Inc. - APIC	13
2.4.3 Analysis of Anomalies.	16
2.5 Macromechanics or Structural Analyses	17
2.6 Summary	20
3 DESCRIPTION OF THE ANALYSES.	23
3.1 Objective	23
3.2 Generalized Plane Strain Finite Element Micromechanics Analysis	24
3.3 Three Dimensional Finite Element Minimechanics Unit Cell Analysis	34
3.4 Summary of Modeling Procedure	43
4 MICROMECHANICS ANALYSIS.	45
4.1 Constituent Properties.	45
4.2 Micromechanics Predicted Thermal Residual Stresses.	66
4.3 Isotropic Carbon Matrix Micromechanics Model Results.	83
4.4 Axial Sheath Micromechanics Model Results	98

TABLE OF CONTENTS (Cont'd)

Section	Page
5 MINIMECHANICS UNIT CELL ANALYSIS.	115
5.1 Effective Material Properties.	115
5.2 Thermal Residual Stresses.	125
5.3 Thermoelastic Property Predictions	126
5.4 Comparison of Predicted Properties	134
6 SUMMARY AND CONCLUSIONS	143
REFERENCES.	145

SECTION 1

INTRODUCTION

1.1 Previous Experimental Efforts

An Office of Naval Research contract to study carbon-carbon materials was initiated at the University of Wyoming in August 1977. Work performed as part of this contract, prior to the present report, was primarily experimental, as reported in References [1-3].

Early emphasis was on the measurement of bulk mechanical properties of a specific three-dimensional cartesian weave carbon-carbon billet [1]. This billet, No. 2696, was fabricated by Fiber Materials Inc. (FMI) from HM-3000 PAN based graphite fibers and Ashland 240 pitch resin. Test methods were developed to measure uniaxial tensile, uniaxial compressive, and shear properties including both strengths and elastic moduli. Acoustic emission monitoring was also performed in order to estimate damage onset within the test specimens. A scanning electron microscope was used to examine failed specimens in an effort to identify specific damage mechanisms.

During a second phase of experimental testing, similar tests were conducted to measure the mechanical properties of three-dimensional cylindrical weave carbon-carbon materials [2]. Sections from two cylindrical weave billets were examined. The first billet section was a 60° arc taken from FMI Billet No. 2208, fabricated from Hercules HM graphite fibers and Ashland A240 pitch. The second billet segment was a complete ring section from General Electric (GE) Billet No. C4X P1-2, fabricated from HM graphite fibers and Allied CP277-15V coal tar pitch. An attempt to measure residual stresses in the complete ring segment indicated that little or no residual stress was present. Uniaxial tension and compression tests were conducted in all three principal material directions, i.e., the axial, radial, and circumferential directions. Shear tests in three of the six shear planes were also performed.

A third experimental effort was primarily concerned with studying the axial tensile response of cylindrical-weave carbon-carbon [3]. Because the tensile properties of carbon-carbon are typically dominated by the fiber bundle properties, emphasis was placed on measuring the

axial tensile properties of single fiber bundles extracted from FMI Billet No. 2208. Results from these single bundle tests were quite scattered, but generally the tensile moduli were higher and tensile strengths were lower than expected, based on rule-of-mixtures predictions and constituent fiber properties. Further axial compression and circumferential tension tests were also performed on the cylindrically woven GE Billet No. C4X P1-2.

fr. 1473
1.2 Summary of Present Work

to 1473
→ The objective of the present work was to analytically model a three-dimensionally reinforced carbon-carbon composite material in order to better understand previously obtained experimental results. Analysis of carbon-carbon materials may be conducted at three geometric levels, typically referred to as micromechanics, minimechanics, and macromechanics. ← Micromechanics models are concerned with the behavior of individual constituents within a composite material, e.g., single fibers and the surrounding matrix within a single fiber bundle. Minimechanics models are concerned with the interactions between fiber bundles and interactions with the matrix pockets present in multi-dimensional woven constructions. Usually minimechanics models study the smallest repeating volume element present in the material, a unit cell. Macromechanics or structural models deal with the largest geometric scale, an entire part or billet. Analyses at the structural scale are usually forced to ignore the details of unit cell construction, for economic or computational reasons. Thus the billet is usually assumed to be homogeneous, although anisotropic.

As part of this investigation, the available literature was reviewed in an effort to obtain as much information as possible on constituent (fiber and matrix) material properties as well as bulk carbon-carbon material properties. Published analytical approaches to modeling carbon-carbon composites were also examined. This literature review is included as Section 2 of the present report.

A generalized plane strain finite element analysis was used to conduct the micromechanics portion of this analytical study. Numerical micromechanics modeling techniques were used to obtain estimates of carbon-carbon unidirectional fiber bundle material properties for later use in the minimechanics unit cell analysis. This micromechanics finite

element analysis includes the effects of temperature-dependent nonlinear constituent material behavior. The analysis also includes a capability to model damage initiation and propagation in order to estimate stress-strain behavior and strength of carbon-carbon fiber bundles. The generalized plane strain finite element micromechanics analysis and associated computer implementation are described further in Section 3. Material properties of carbon-carbon fiber bundles predicted using this micromechanics analysis are summarized in Section 4.

With the predicted fiber bundle properties as input, a full three-dimensional finite element analysis was used to perform the unit cell micromechanics analysis. The three-dimensional analysis also includes capabilities for modeling temperature dependent nonlinear material behavior as well as damage initiation and propagation. This analysis and computer implementation are described in Section 3. Predicted bulk material properties for a rectangular weave carbon-carbon material, results of the three-dimensional micromechanics analysis, are discussed in Section 5.

Overall, the capabilities of these analyses to predict carbon-carbon composite material properties has been demonstrated. An advantage of the numerical techniques used here is the ability to predict the complete nonlinear stress-strain behavior of the bulk composite material. Further refinement of the computer programs implementing these analyses will continue. The choice of appropriate constitutive relationships for nonlinear orthotropic materials is also an area warranting further study. Conclusions of this present study, including a summary of present limitations and suggestions for further work, are discussed in Section 6.

SECTION 2

PRIOR ANALYTICAL MODELS

2.1 Background

An early paper describing the development history of carbon-carbon materials up to that time was published by Schmidt in 1972 [4]. According to Schmidt, carbon-carbon materials originated in the late 1950's, probably by accident. During an experiment to determine the fiber volume content of an oxide fabric/phenolic composite, a laboratory technician at the Chance Vought Corp. inadvertently covered the heated crucible. The phenolic matrix was not completely vaporized at high temperature, resulting in a "reduced resin laminate" which had relatively high strength. The advantages of carbon-carbon were, and still are, an ability to retain useful mechanical properties at high temperature, and resistance to thermal stress and thermal shock. Schmidt also supplied at that time a list of 162 related references, not keyed to the paper.

Because carbon-carbon materials remain useful at highly elevated temperatures, many applications for this material have been for components of reentry vehicle and rocket nozzle designs. Thus, much of the funding for carbon-carbon research has been supplied by the Department of Defense, primarily the Navy and the Air Force. While much of this funded research has been for applications, i.e., hardware oriented, more fundamental studies of material behavior have also been conducted.

Available literature on the subject of carbon would occupy a small library of its own. Even by restricting the subject to carbon fibers and carbon-carbon composite materials, the number of available papers and reports is still quite large, even with recent restrictions on publication of such research. Carbon-carbon materials research may be broadly (and with much overlap) grouped into four areas: processing, characterization, analytical modeling, and hardware. Processing studies are concerned with the production of high quality, consistent carbon-carbon billets. Many of these studies tend to be empirical in nature, involved with the effects of various processing parameters on final production material. Closely related to the processing studies are the

characterization studies. Characterization programs are concerned with measuring the material behavior under a variety of loading and environmental conditions. Topics of these characterization programs include test method development as well as material property response. Obviously, the processing and characterization studies are closely related; many research programs contain elements of both. Analytical modeling programs are concerned with developing mathematical models to describe the thermo-mechanical behavior of carbon-carbon composite materials. As analytical modeling is the subject of this present report, these studies were of most immediate interest. Finally, those programs grouped as hardware studies involve the design, fabrication, and performance of a specific hardware component, e.g., a reentry vehicle nose tip. These studies are more application oriented.

It was the purpose of the present research program to attempt to analytically model three-dimensionally reinforced carbon-carbon composite materials in order to improve understanding of the behavior governing the thermomechanical performance of the composite. Therefore, previous analytical material modeling studies were of immediate interest to this work, and are briefly reviewed in this present section. Material characterization studies were also very important to the present work, providing input data for the models developed here as well as data for correlation tests of the model. The characterization studies used to provide constituent material properties are described in more detail in Section 4. While processing effects are of great importance in determining the final properties of a carbon-carbon composite, modeling of the processing environment was beyond the scope of the present investigation. Finally, the present research was concerned with modeling the thermomechanical response of the carbon-carbon composite material itself, rather than the design of a specific hardware component. Thus specific hardware oriented studies are not summarized here.

2.2 Levels of Analysis

Analytical modeling of realistic carbon-carbon materials is a very challenging task. Carbon-carbon composites are heterogeneous on a large scale when compared to many other materials. Carbon-carbon composites exhibit inelastic behavior, possess irregular phase geometries, and sustain cracking damage during fabrication. The matrix material may be

highly oriented in various regions and contains nonuniformly distributed cracks and voids. Finally, the constituent material properties are difficult to measure experimentally and may differ radically between in-situ composite properties and bulk material response.

Despite these difficulties, various modeling approaches have been attempted, with subsequent increases in the level of understanding of the material behavior. These analytical efforts may be loosely grouped into three classes based on the scale of the attempted model. The first class, usually called micromechanics in the literature, deals with the interactions between individual fibers and between fibers and the surrounding matrix material. A major difficulty in analyzing carbon-carbon materials at this level is a lack of sufficient constituent material properties data in order to conduct such an analysis. In-situ material properties at the micromechanics level are experimentally very difficult (and therefore expensive) to measure, particularly over the temperature ranges encountered by carbon-carbon composites during fabrication and use. Furthermore, voids and cracks larger than several fiber diameters may be present. Broken or twisted fibers may also occur. These difficulties aside, micromechanics approaches are useful in estimating the response of unidirectional carbon-carbon materials. A micromechanics analysis may be used to predict effects of processing on composite properties as well as the effect of poor (or good) interface bonding between fiber and matrix. The thermomechanical response predicted by a micromechanics analysis may then be used to generate a set of consistent thermomechanical properties for unidirectional carbon-carbon fiber bundles for use in a second level minimechanics analysis.

At the minimechanics level, an analysis is performed on the smallest repeating geometric volume element within the composite material, termed a unit cell. The level of abstraction is such that individual fibers are not explicitly modeled. Instead, the interactions between fiber bundles and matrix material, as well as fiber bundle-fiber bundle interactions, are of interest. Constituent material behavior at this scale is still very difficult to measure experimentally. However, one source of material properties information is a micromechanics analysis, as previously discussed.

A third level of analysis is at the macromechanics or structural scale. At the structural level an actual part or structure is modeled, subjected to in service loads and environmental conditions. At this level it is not possible to include unit cell geometry nor individual constituent behavior. At the structural level, the carbon-carbon material is treated as a homogeneous anisotropic solid. Mechanical properties at this scale are more easily measured. However, deriving an appropriate constitutive relation capable of describing the complex material behavior at this level is difficult. Experimental characterization is used to provide material properties data, although testing is time consuming and of course requires that the actual composite first be fabricated.

2.3 Micromechanics Analysis

Early attempts to model carbon-carbon composites began separately at the micromechanics and macromechanics levels. Investigators studying the material response of carbon-carbon composites as a material system approached the problem from the micromechanics viewpoint. Rule-of-mixtures techniques were used by Butler, et al. [5] to examine the role of fiber-matrix and matrix-matrix interfaces affecting the properties of unidirectional carbon-carbon composites. Attempts to correlate strengths using the rule-of-mixture approach were unsuccessful. A similar approach was used by Perry, et al. [6], who also studied unidirectional carbon-carbon materials.

Evangelides [7] examined the influence of "microstructural factors" that influence failure of carbon-carbon. In particular, orientation of the matrix material was identified as an important influence on the bulk Young's modulus of the composite. Observations of this oriented matrix "sheath" were presented, as well as rule-of-mixtures predictions for its influence on composite properties. A statistical model for composite strength, including the influence of bent fibers and a wavy sheath, was developed. Analytical predictions of stress-strain behavior in unidirectional carbon-carbon composites were also shown. Limited correlations of analytical predictions with experimental data did indicate good agreement.

To further study processing induced stresses and strains, Evangelides, et al. used the SAAS III finite element program to model

unidirectional carbon-carbon composites [8]. Possible combinations of fiber, bulk matrix, and sheath were investigated. Predicted stress levels were high due to the assumption of fiber-matrix interface integrity. However, the influence of temperature changes on internal stress states was demonstrated. Furthermore, the type of matrix was shown to have significant influence on stress levels within the composite.

An analysis of fiber bundle strength was performed by Evans and Adler [9], who used a thermodynamics and mechanics approach to analyze "kinking" or fiber bundle micro-buckling in carbon-carbon composites. Observations of this kinking in a three-dimensional carbon-carbon were presented. These authors found the matrix yield strength and fiber fracture strength to be the most important parameters influencing fiber bundle failure in this kinking mode. No comparisons of their analytical results with experimental data were presented.

A model incorporating interfacial friction between fiber and matrix was presented by Jortner [10]. The effect of frictional load transfer on strength and thermal expansion was shown. The effect of fiber bundle rotation during shear loading was also examined.

Micromechanics approaches are most often used for modeling stress states and damage mechanisms in unidirectional composites. As applied to three-dimensionally reinforced carbon-carbon materials, these analyses are useful for predicting the behavior of a fiber bundle within the multi-dimensionally woven material. However, most micromechanics analyses do not correctly model the response of multi-dimensionally woven carbon-carbon composites. Many investigators have made use of micromechanics analyses to provide input material properties to a second level minimechanics analyses.

2.4 Minimechanics Analyses

2.4.1 Materials Science Corporation - DCAP

During the middle and late 1970's, investigators at the Materials Science Corporation (MSC) developed a combined micromechanics/minimechanics analysis to model three-dimensionally reinforced carbon-carbon composite materials [11-13]. Their minimechanics model used a carbon-carbon unit cell divided into five subregions. Three of the subregions corresponded to the three unidirectional fiber bundle

composites oriented parallel to the principal material axes. The remaining two subregions represented the two interstitial carbon matrix pockets. This micromechanics model admitted linear elastic constituent properties which were functions of temperature. A fiber bundle subregion within the unit cell was considered to consist of transversely isotropic fibers and matrix material which could contain oriented cylindrical voids. The interstitial matrix regions were orthotropic and could contain dispersed spherical voids. Finally, the contact or interface areas between the subregions could be weakened or partially failed, resulting in a degraded load transfer capability across that interface.

Properties for each subregion were calculated based on properties of the constituents making up that subregion, using a micromechanics approach. Fiber bundle subregions consisted of transversely isotropic fibers and transversely isotropic matrix. The matrix within a fiber bundle was transversely isotropic due to the presence of cylindrical voids. First, a set of thermoelastic properties was calculated for the isotropic matrix material based on an assumed void volume fraction. This set of matrix thermoelastic properties was then combined with the fiber properties to calculate a set of thermoelastic properties for the fiber bundle. Thus the calculation of the fiber bundle subregion properties was performed using a micromechanics approach.

Specific micromechanics techniques used in the MSC analysis followed procedures developed by Hashin and Rosen for estimating upper and lower bounds on composite material properties [14]. Effects of cylindrical voids within the fiber bundle matrix material were discussed in Reference [11]. However, no further discussion of voids in the bundle matrix material was included in later reports [12,13], nor was any mention made of measured or assumed void volume values. Averaged with-grain and across-grain material properties for ATJ-S graphite were used in the numerical computations. Thus, it is not clear that porosity in fiber bundle matrix material was actually included in the results of References [11-13]. The effect of this porosity was probably small when compared to other damage processes occurring within the carbon-carbon unit cell, and was subsequently neglected.

It has been shown that the carbon matrix material within fiber bundles may become oriented during fabrication of the carbon-carbon

material [7]. One technique for modeling this orientation is to increase the fiber volume content of the fiber bundle. The MSC analysis allowed for varying combinations of fiber-matrix-void volume content in the fiber bundle subregions and different matrix-void combinations in the interstitial matrix subregions.

The effect of cracking within a unit cell model was also included in the analysis. Cracks were modeled as planes of weakness occurring at interfaces between the various subregions as well as within the interstitial matrix subregions. The effect of these cracks was included in the form of a load transfer efficiency parameter, i.e., the ability to transfer some proportion of loading across a degraded interface. Cracking in the classical fracture mechanics sense was not included.

Analytical techniques used to solve the MSC model included a combination of approaches. The micromechanics models were solved as boundary value problems in which the internal details of material structure were included. The minimechanics model used a combination of a self-consistent approach and variational principles. In all of these analyses, material properties were assumed to be linear elastic and temperature-dependent.

The MSC analysis summarized in Reference [12], contained two parameters which had the effect of tailoring the analysis to fit experimental data. These parameters were the sheath content and the unit cell efficiency parameter. With appropriate choices of these two values, excellent agreement was obtained between analytically predicted and experimentally measured thermoelastic properties for three-dimensionally reinforced carbon-carbon. As was pointed out in Reference [12], similar values for sheath content and unit cell efficiency were applicable to several different three-dimensional carbon-carbon composite material systems.

The addition of various failure criterion for strength prediction within the MSC models was described in Reference [12]. Primary failure mechanisms were identified, based on stress states within the unit cell. For various loading conditions the most probable failure modes were analyzed for their effect on the material failure surface.

For uniaxial tension, the tensile strength was assumed to be fiber-dominated, therefore transverse fiber bundles and interstitial

matrix played only a secondary role in determining a composite strength. The occurrence of extensive interfacial cracking resulted in low composite Poisson's ratios. Thus the contribution of subregions other than the fiber bundles in the direction of loading to the tensile strength was argued to be negligible. Hence, the composite tensile strength used in the analysis was dominated and predicted by failure of the impregnated fiber bundle lying in the direction of tensile loading.

Failure of the impregnated fiber bundle could occur by two principal mechanisms, both due to the existence of flaws along an individual fiber length. If the bundle failed by an accumulation of scattered fiber breaks, the mode of failure was by the "cumulative weakening" mode. However, if the stress concentrations due to local fiber breakage became large, a crack could propagate transversely across the bundle causing failure. This was termed the "fiber break propagation" mode.

Based upon the idea that the actual mode of failure was dependent upon the matrix properties, the mode of failure for impregnated bundles used in the analysis was the cumulative weakening mode. Failure of fiber bundles at high temperatures (above 4000°F) was modeled by plastic flow in the direction of loading, called "limit" behavior. The oriented or "sheath" matrix strongly influenced the Young's modulus of the fiber bundle. However, the sheath in actual carbon-carbon fiber bundles is likely to be discontinuous, and was neglected in tensile strength predictions.

Like tensile failure, compressive failure can occur by several different mechanisms, including fiber or matrix fracture, fiber buckling in shear or extension, or complete macrobuckling of the impregnated yarn bundle. Based upon the mode of failure with the lowest corresponding compressive strength, shear mode buckling of the impregnated fiber bundle was included as the compressive failure mechanism for temperatures below 4000°F. Plastic limit failure was the modeled compressive failure mechanism above 4000°F.

Shear stress-strain response in carbon-carbon materials is nonlinear. Failures occur at the fiber bundle-fiber bundle and the fiber bundle-matrix interface regions. An overall composite shear strength is dependent on the interfacial shear strength and the degree of interface

slippage. Linear shear stress-shear strain behavior limited by the shear yield strength was assumed in the MSC analysis.

For the modeled failure mechanisms, equations were developed in Reference [12] which allowed the computation of composite ultimate strengths given constituent material properties and geometric data. Effects of combined loading were explored in Reference [12] to determine the influence of multiaxial stress states on the failure envelope. Based on this investigation, a failure envelope in stress space for three-dimensional carbon-carbon composites was developed and incorporated into the MSC minimechanics analysis.

Overall, the MSC analysis, implemented as a computer program named DCAP, is probably the most versatile and useful predictive tool for modeling three-dimensional carbon-carbon composite materials developed to date. This model incorporated the necessary micromechanics detail into a minimechanics unit cell geometry in order to predict global or effective thermomechanical properties for bulk three-dimensional carbon-carbon. These estimates included values for stiffnesses as well as for strengths. Results computed using this model indicated good agreement with experimental data [12,13] and were used for evaluation purposes on materials with actual hardware applications [15,16]. The model was limited in that it was linear elastic, while some loading modes, particularly shear, produce distinctly nonlinear material behavior. Also, the unit cell efficiency and the sheath content had to be evaluated by correlation with experimental data on bulk three-dimensional carbon-carbon materials.

2.4.2 Science Applications Inc. - APIC

A second major effort to analytically predict material properties for three-dimensionally woven carbon-carbon was conducted by Science Applications, Inc. (SAI), results of which were summarized in References [17-19]. This comprehensive analytical and experimental effort was called Analytical Processing for Improved Composites (APIC). A basic premise of the study was that processing parameters control the final thermomechanical properties of a three-dimensional carbon-carbon material. Thus models were developed to predict the influence of the entire processing environment on final material properties. In a separate task, model composites were tested in order to measure the

material properties of the constituent fiber bundles and matrix forming the unit cell.

The analytical effort was divided into two parts, a process environment model and a mechanical model [18]. The primary purpose of the process environment model was to predict the pressure and temperature present in the processing vessel. Once the environment was determined, the mechanical model predicted displacements, strains and stresses. Given a stress state, a failure analysis was performed to determine the possibility and extent of any damage that occurred. These analyses were repeated incrementally until an entire process had been modeled.

The process environment model was composed of four computer programs. The largest and most important computer code was a two-dimensional finite element analysis of the time-dependent primary variables, i.e., pressure, temperature, and gas volume fraction. A second computer program predicted the three-dimensional thermal and diffusion properties. A third computer program performed a degree of graphitization analysis by evaluating the graphite layer spacing achieved compared to a theoretically possible spacing. Finally, a graphics postprocessor provided contour and section plots of the primary variables at prescribed time points.

The mechanical model was centered around a computer program called MIPAC (MICromechanics Processing Analysis Code). This program modeled the progressive mechanical damage occurring during processing and predicted the modified composite properties resulting from this damage. This analysis, on the scale of the composite unit cell, was a mini-mechanics analysis. The computer program was a three-dimensional finite element analysis incorporating features to accurately model interfacial behavior. The analysis used three-dimensional 27 node brick elements with three degrees of freedom per node for a total of 81 degrees of freedom per element. Nodes were located at the 8 corners, 12 mid-edges, 6 mid-faces and the centroid of the element. A quadratic shape function was employed along with generally anisotropic material properties.

Structural configuration, damage effects, and material properties of the constituents were defined by input to MIPAC. Plastic strain or displacement fields resulting from shrinkage, swelling or externally

applied loads were permitted. The program output included elemental displacements and forces, system displacements and forces, and mechanical strains and stresses.

Element formulation was based upon standard variational principles [18]. Displacement compatibility was altered to model possible complex interfacial failure and sliding between interfaces. The mathematical methodology for these compatibility conditions was described in detail in Reference [17].

The entire APIC analysis was conducted on three geometric scales, from a micromechanics approach, to a minimechanics unit cell, to a macromechanics analysis of a complete carbon-carbon billet. The first level of abstraction used in the analysis was at the constitutive level, to provide properties data for use at the unit cell level. If stresses in the unit cell model were severe, a failure analysis was performed at the constitutive or micromechanics level and the resulting corrected constitutive properties were returned to the unit cell model.

The minimechanics unit cell was the main focus of the mechanical model, for it is here that constituent interaction occurred due to processing effects or service conditions. Behavior of the unit cell was dependent upon the boundary conditions stipulated at the billet level and constituent properties predicted by the micromechanics model. The process environment model was used to generate temperature and pressure information. Failure was simulated in the MIPAC program by a change in connectivity of the system. Healing of failed interfaces was possible through recovery of interfacial strength.

The final level of analysis was a macromechanics model of the billet used to determine a general state of stress and overall billet deformation. The strain response of the billet was imposed on unit cell models at various positions within the billet. Internal pressure and temperature conditions were obtained from the process environment model. The billet was treated as a homogeneous continuum with properties that varied from point to point, as obtained from the minimechanics unit cell models.

Interaction between the billet level and unit cell level was on a real time basis when necessary. However, this coupling was minimized by interpolating between widely spaced time steps during essentially

elastic material response and backtracing to points where inelastic response had begun to occur if nonlinear behavior was encountered. After location of an intermediate time point at which inelastic behavior had begun, coupling between unit cell level and billet level was performed at time increments designated by the analyst. Accuracy of the solution was thus a function of the time steps taken.

Recommendations to improve carbon-carbon processing were made in Reference [19]. Property predictions for various processing environments were also included. However, little correlation between analytically predicted properties and experimental data was presented, even though extensive experiments were performed on a model carbon-carbon material, summarized in Reference [17].

The APIC analysis was a very versatile but complex approach. Emphasis was on predicting the processing environment and subsequent effects on material properties. It appeared that this analysis was very time consuming to use, and was not verified by comparison to experimental data. However, understanding the effects of process environment on final carbon-carbon material properties was enhanced by this work.

2.4.3 Analysis of Anomalies

The minimechanics analyses approaches previously discussed did not normally consider anomalous regions within a carbon-carbon material. Such regions contain flaws in the material, e.g., distortions of the weave, density gradients, and microcracking. Anomalies such as these have been carefully catalogued and described by Jortner [20]. Jortner also modeled these anomalies and conducted experiments to verify his models [21]. His work resulted in the development and use of three computer programs, BOUND, KSLANT, and WAVETEC, designed to predict thermomechanical properties and failure for three-dimensional carbon-carbon composite materials containing reinforcement distortions.

The BOUND computer program was used to calculate estimates for elastic constants, thermal expansion coefficients, and thermal conductivities by use of bounding techniques. Like the MSC DCAP program described earlier, BOUND used a degradation factor to model weak or partially failed interfaces within a unit cell. This analysis could

model unit cells with nonorthogonal fiber bundles oriented in as many as seven directions.

The KSLANT computer program was written as a specialized analysis to calculate thermal conductivities. It included a mechanism designed to modify the yarn volume of the unit cell based on distortions caused by "slanting" of one fiber bundle.

The WAVETEC computer program was used to predict the thermomechanical properties and thermal conductivities for materials containing wrinkles or waves. Two types of distortion were examined, rotation of an ideal orthogonal orthotropic unit cell, and unit cells containing slanted fiber bundles.

Experiments conducted on three carbon-carbon materials to measure compression Young's moduli and thermal expansion coefficients were compared with WAVETEC predictions [21]. Considerable scatter was apparent in the thermal expansion results. Even so, predicted and measured thermal expansion coefficients did not follow similar trends. Predictions of Young's moduli were in reasonable agreement with experimental data.

2.5 Macromechanics or Structural Analyses

A goal of any of the previously discussed minimechanics analyses was to predict the bulk thermomechanical behavior of the carbon-carbon material. These material properties could then be provided to a macromechanics or structural analysis as a consistent set of homogeneous anisotropic material data.

At the structural scale, entire components of carbon-carbon are modeled. Thus, it is not usually feasible to include the detail of micromechanics or minimechanics modeling. This is not to say that such detail cannot be included. Investigators have in the past, conducted analyses at all three levels, using results at one level to refine input to a different level of analysis. Problem solution became a step-by-step process, proceeding from micromechanics to minimechanics to macromechanics. The macromechanics stress-strain state was then imposed on the minimechanics model to identify possible failure modes and material property changes.

Early investigators, lacking or not believing in micromechanics and minimechanics analyses, modeled carbon-carbon as a homogeneous

anisotropic material. Because some applications for three-dimensionally woven carbon-carbon materials were as replacements for pyrolytic graphite, these analysts made use of the structural analysis tools (often finite element programs) already available to them. Constitutive material models were altered to use appropriate properties for the three-dimensional carbon-carbon. One such example is the work by Pardoen [22,23]. Pardoen used an approximate technique to modify the polar coordinate constitutive relations of an existing axisymmetric finite element analysis (SAAS III) in order to accommodate a rectangularly orthotropic material. Accuracy of the approximation was verified by modeling a rotating orthotropic disk and a thermally loaded orthotropic disk, for which analytical solutions were known. In Reference [23], the modifications to an asymmetric stress analysis of axisymmetric solids (ASAAS) in order to model an anisotropic material were presented.

Geiler also used a modified ASAAS computer code to account for nonradially orthotropic material behavior [24]. Geiler used this modified computer program to analyze a pressurized ring and a ring subjected to a radial temperature distribution. Kotlensky [25] analyzed carbon-carbon substrates for throat inserts of solid propellant rocket nozzles using a one-dimensional thermal stress analysis and the Stress Analysis of Axisymmetric Solids (SAAS III) finite element computer program. His work resulted in specifications for candidate substrate materials using different fabrication techniques.

In the above mentioned macromechanics analyses, material properties were presumed to be linearly elastic. The models provided reasonable estimates of the stress states present. Strength or failure predictions were not attempted in these macromechanics models.

Jones attempted to model the nonlinear material behavior of three-dimensionally reinforced carbon-carbon composites [26] using a constitutive relation developed earlier for use with ATJ-S graphite [27-29]. The constitutive model was based on a deformation theory of orthotropic plasticity and allowed for differing nonlinear stress-strain responses for different stress components. Varying Poisson's ratios were also admissible, allowing for modeling of a "biaxial softening" phenomenon due to microcracking. This constitutive relation permitted finite plastic volume changes, differing from the usual restriction in

plasticity theories of no plastic volume change. Material properties were related to the multiaxial state of stress and strain by the strain energy. An interaction procedure is used to simultaneously satisfy the nonlinear stress-strain relations and the material property versus energy equations. In Reference [28], Jones and Nelson extended this model to initial loading of graphite under mixed tension and compression using the same fundamental procedure for calculation of the basic material properties. The model was extended to thermal loading of nonhomogeneous bodies of graphite in Reference [29]. The model was adapted for carbon-carbon composites in Reference [26], and compared to experimental data with good agreement.

Although Jones, et al. [26-28] addressed the nonlinear aspects of graphite and carbon-carbon, they did not attempt to predict damage onset and eventual failure.

Stanton and Kipp used a similar approach in their models of two-dimensional woven carbon-carbon involute structures [30,31]. In their work, the material model of Batdorf [32] was incorporated into a finite element analysis of involute cones. Verification of their model was demonstrated by comparison with tests on coupons, cylinders, and cones fabricated specifically for correlation purposes. These authors concluded that two-dimensionally woven carbon-carbon was quite different in behavior from three-dimensional materials. The thrust of this present research was to model three-dimensionally woven carbon-carbon materials. However, useful insight to carbon-carbon material behavior was provided by References [30,31].

A recent study of yield and failure in three-dimensional carbon-carbons was performed by Pollock and Sun [33]. These authors conducted off-axis tension and compression tests on two different three-dimensional carbon-carbon materials. The Tsai-Hill and Tsai-Wu failure criteria were used to evaluate yield strength versus fiber bundle angle in the off-axis tests. Generally nonlinear stress-strain response was described by a single equation using a form suggested by Ramberg and Osgood [34]. This effective stress-strain behavior, as well as the yield and failure criteria were then used in two-dimensional linear elastic and inelastic finite element models to study tensile specimens containing holes.

Pollock and Sun's results confirmed some of the results of Waeber and Hagen, who discussed failure theories as applied to carbon-carbon [35]. Both macromechanics and micromechanics failure theories were investigated, including limitations of each. Waeber and Hagen noted that macromechanics or phenomenological theories required large data bases for accurate characterization, that had to be updated each time processing variations changed material properties. Micromechanics theories, on the other hand, were exceedingly complex if general enough to handle various material designs and processing techniques. Mathematical formulations for some of the failure theories were presented, with emphasis placed on the macromechanics phenomenological approaches.

In a following report, Waeber and Hagen applied the Wu-Tsai failure criterion to a three-dimensional orthogonal weave carbon-carbon composite [36]. After simplifications, a second order tensor polynomial failure surface was obtained. They concluded that with the state of characterization of carbon-carbons at that time, the additional complexity of the Tsai-Wu criterion added little increased ability to carbon-carbon composite failure prediction.

2.6 Summary

From the preceding paragraphs, one can sense the complexities involved in modeling carbon-carbon materials. The various analyses previously discussed approached the problem from different geometric scales and included (or excluded) many different material factors. It is clear that three-dimensionally reinforced carbon-carbon materials can be modeled using combined micromechanics/minimechanics approaches, perhaps best demonstrated by investigators at Materials Science Corporation [11-13] with their DCAP computer program. The significance of processing parameters on final material performance was exhaustively modeled by investigators at Science Applications, Inc. [17-19]. Jortner demonstrated the influence of defects in modeling these materials [10, 20]. Finally, Jones [26-29], Pardoen [22], Pollock [33], and others showed that three-dimensional carbon-carbon materials could be analyzed for structural applications as long as sufficient materials characterization data were available.

An attempt has been made in this section to briefly summarize the previous analytical approaches to modeling carbon-carbon. The intent was to provide some representation of these previous modeling efforts as background for describing the modeling approach used in the present research.

SECTION 3

DESCRIPTION OF THE ANALYSES

3.1 Objective

The objective of the present research, as stated earlier, was to develop a combined micromechanics/minimechanics analysis to model three-dimensional orthogonal weave carbon-carbon materials. The overall approach was similar to the previously discussed work by Materials Science Corporation [11-13] in that a micromechanics analysis was used to predict fiber bundle constitutive properties for use in a minimechanics unit cell model. The overall goal of these analyses was to predict bulk carbon-carbon material properties, thermomechanical stress-strain behavior, and damage progression. The present approach differed from the MSC work in that finite element methods were used to perform both the micromechanics and the minimechanics analyses. Use of these methods permitted inclusion of nonlinear temperature-dependent inelastic material properties in modeling the complex geometries present in carbon-carbon. Both finite element computer programs described in subsequent paragraphs contain schemes for modeling damage initiation and propagation.

Processing effects on final material properties were included in the micromechanics analysis in the sense that cooldown from a final graphitization temperature was modeled. Thus the effects of thermal residual stress-induced cracking on fiber bundle properties were included. No attempt was made in this present research to model an actual material processing environment prior to the final elevated fabrication temperature. It was entirely feasible to model the effects of geometric anomalies, similar to the spirit of Jortner's work [20]. However, to limit the overall program scope, analysis of anomalous weave geometries was not included in the present work.

Both the micromechanics and the unit cell minimechanics analysis were performed with finite element computer programs developed and written by the Composite Materials Research Group (CMRG) at the University of Wyoming. These computer programs were developed as part of this present research effort, and other externally and internally sponsored research. The micromechanics analysis is a two-dimensional

generalized plane strain finite element computer program, specifically written for analyzing unidirectional, continuous fiber composite materials. The unit cell micromechanics analysis model is a full three-dimensional finite element computer program. Specific capabilities and features of both computer programs are discussed in subsequent paragraphs.

3.2 Generalized Plane Strain Finite Element Micromechanics Analysis

The micromechanics analysis used in this present research employs the finite element method to predict the thermomechanical behavior of continuous unidirectional fiber-reinforced composite materials. The finite element method is selected because it can be readily applied to complex geometries as represented by a fiber embedded in a matrix material, as illustrated in Figure 1. Various packing geometries for fibers within the matrix may be assumed. A square packing array has been demonstrated to provide good correlation with experimental data [37]. Via symmetry arguments, the region of interest to be modeled may be reduced from that shown in Figure 1, to the region shown in Figure 2, a quadrant of one fiber and the surrounding matrix material.

It is assumed that displacements may occur in all three coordinate directions. Specifically, each displacement is dependent on the 2 and 3 coordinate directions (see Figures 1 and 2) and the displacement in the 1-direction (fiber direction) has an additional linear dependence in the 1-direction. Including 2 and 3 dependence of the displacements in the fiber coordinate direction allows a form of axial (longitudinal) shear deformation corresponding to generalized plane strain [38,39]. Therefore, although the analysis is basically two-dimensional, five components of directly applied stress can be modeled, specifically σ_1 , σ_2 , σ_3 , τ_{12} , and τ_{13} . Biaxial tension and compression normal stresses may be applied in the 2 and 3 directions to simulate a τ_{23} applied shear stress loading as well.

If the unidirectional composite material is assumed to be transversely isotropic in the 2-3 plane, it is then possible to predict the mechanical properties of the composite with four applied stress loading cases. These four cases, σ_1 , $\sigma_2 = \sigma_3$, $\tau_{12} = \tau_{13}$, and τ_{23} are illustrated in Figure 3. The σ_1 , σ_2 , and τ_{12} stresses shown in Figures 3a, 3b and 3c can be applied directly. Transverse shear stress, τ_{23} , is

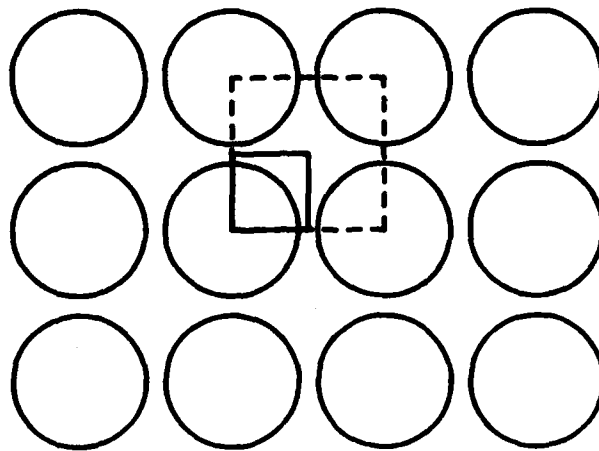


Figure 1. Unidirectional Fiber-Reinforced Composite Material with a Square Fiber Packing Array.

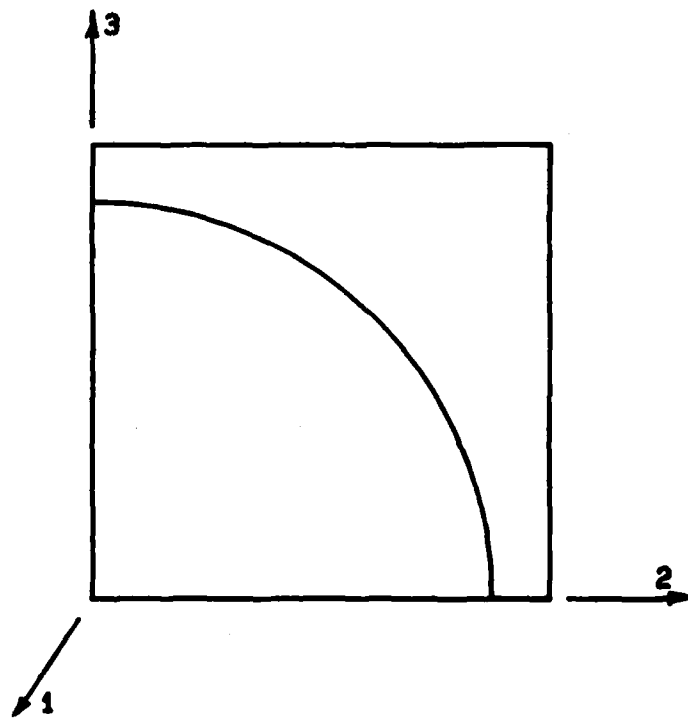
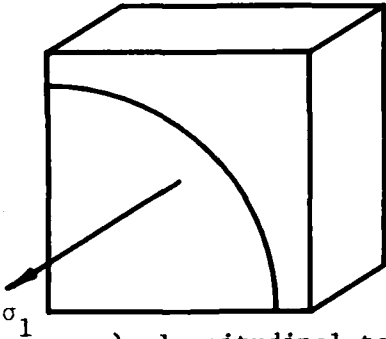
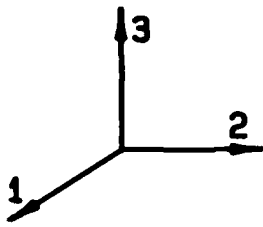
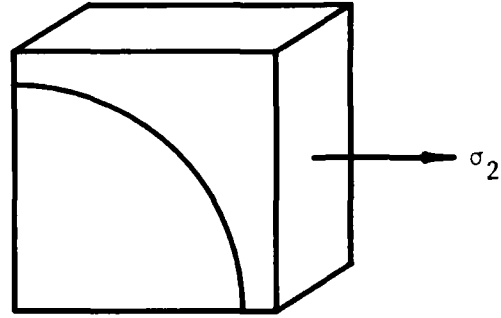


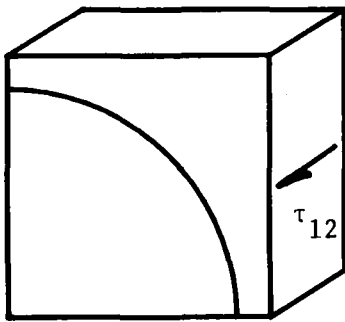
Figure 2. Quarter Fiber Micromechanics Model.



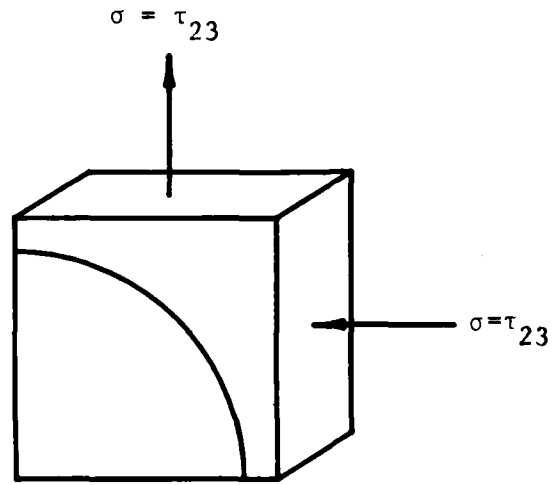
a) longitudinal tension



b) transverse tension



c) longitudinal shear



d) transverse shear

Figure 3. Micromechanics Applied Loads for Unidirectional Composite Stress-Strain Characterization.

simulated by applying biaxial normal stresses in which the stress components are equal in magnitude and opposite in sign, as shown in Figure 3d. The induced τ_{23} shear stress is

$$\tau_{23} = \frac{\sigma_2 - \sigma_3}{2} = \frac{\sigma - (-\sigma)}{2} = \sigma \quad (1)$$

The τ_{23} shear stress produced in this manner is not rigorously correct in that the shear stress is parallel to a line at 45° from the material 2 or 3 coordinate axes, as shown in Figure 4. Thus, the τ_{23} shear is actually being applied to a composite material with the fiber packing array shown in Figure 4 rather than the fiber packing array shown in Figures 1 and 2. However, the difference in predicted composite material properties has been shown to be small, [37]. Therefore, the difference was neglected in this work.

This generalized plane strain finite element micromechanics analysis permits orthotropic or isotropic constitutive material behavior, which may be temperature- and/or moisture-dependent. These features of the analysis were described in References [40,41]. Orthotropic materials are assumed to be linearly elastic. Isotropic materials are assumed to be elastoplastic, obeying an octahedral shear stress yield criterion with plastic strains following a Prandtl-Reuss flow rule. Loads (including changes in temperature or moisture content) are applied incrementally, and material behavior is calculated using a tangent modulus method.

Nonlinear octahedral stress-strain constitutive behavior is entered into the analysis in a form first suggested by Richard and Blacklock [42], i.e.,

$$\sigma = \frac{E\epsilon}{[1 + |\frac{E\epsilon}{\sigma_0}|^n]^{1/n}}$$

where ϵ = strain (2)
 E = initial modulus
 n = curvature parameter
 σ_0 = asymptotic stress

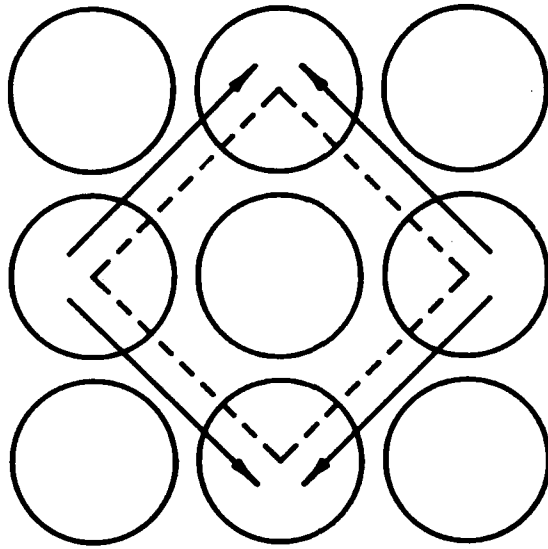


Figure 4. Transverse Shear Stress Applied as Biaxial Normal Stress Loading of a Unidirectional Composite Material with a Square Fiber Packing Array.

Three parameters, E , n , and σ_0 , describe the nonlinear stress-strain response for a material at a particular temperature. These three parameters themselves may be functions of temperature (and moisture). Thus the complete isothermal stress-strain description of a material is contained within one equation. A more detailed discussion of this analysis along with citations of the appropriate literature, was presented in Reference [40]. Representation of the specific constituent material properties used in this present work is described in Section 4.

Damage initiation and propagation are modeled within the analysis by use of a "failed element" technique described by Adams, *et al.* in References [43-48]. When an element in an area of high stress exhausts its ability to bear additional stress, as determined by an appropriate failure criterion, it fails. It is assumed that a "crack" has thus formed and has the dimensions of the failed element. This approximation has two implications, the most important of which is that a finite amount of material is removed from the system, which in an actual material is not the case. The second implication is that the crack is not likely to close up on itself in subsequent loading due to its exaggerated width. These effects can be minimized to a practical degree by making the finite element grid very fine and uniform in areas of anticipated crack initiation.

An element cannot simply be deleted from the finite element mesh when it reaches its ultimate stress. Force equilibrium at every node point in the mesh must be maintained. Thus at element failure, node point loads equal in magnitude and opposite in direction to the element stress equivalent node point loads must be applied. The failed element material properties are also set to zero, or near zero to avoid numerical singularities, such that the element makes no further contribution to the global stiffness matrix.

In the present analysis, element failure can occur as defined by one of four installed failure criteria, viz., maximum normal stress, maximum shear stress, maximum octahedral shear stress and strain, and a Tsai-Hill failure criterion. Obviously not all criteria are appropriate for all materials. Furthermore, selection of the appropriate failure criterion can significantly affect the predicted composite material

stress-strain response. Specific failure criteria used in this present analysis are discussed in Section 4.

Although loading increments are kept small once element stresses near their ultimate values, it is unlikely that an element will fail exactly at the maximum value of an applied load increment. The applied load increment will probably be greater than the load necessary to just cause failure in any given element. For this reason, when an element failure is detected, the load increment is automatically scaled back to the point of first element failure. The appropriate element or elements are "failed", by applying equal and opposite node forces and by reducing the element stiffness values. The analysis then recalculates the stress state. Remaining elements are checked to ensure the redistribution of stresses has not caused additional elements to fail. When no further element failures are detected, loading proceeds with the next increment. Thus, incremental loading of the model, incorporating appropriate failure criteria for determining element strength, and a scheme for "failing" elements and redistributing the stresses, constitutes the damage progression and crack propagation portion of this finite element micromechanics analysis. Catastrophic failure is assumed to occur when a crack has divided the finite element model into two separate segments.

The present version of this finite element micromechanics analysis is implemented in a computer program called WYO2D, written by Cilensek [49]. The analytical features briefly summarized here are incorporated into a finite element computer program designed around an architecture similar to that used by Hinton and Owen [50]. Loading increments are defined in one input file. Finite element mesh information is input as a second file. Constituent material properties data are included as subroutines in the computer program. The main controlling program reads a loading increment from an input file and calls subroutines to assemble the global load vector and stiffness matrices. A reduced integration or frontal solution technique is used to find the displacement field for the current loading increment. A separate set of subroutines then calculates the stress state, checks for element failure to model crack initiation and propagation, and performs the necessary global load vector and stiffness matrix reassembly and re-solution. The crack propagation subroutines continue to automatically recalculate stresses

and monitor crack propagation until a crack becomes stable or the entire model fails. Once a crack becomes stable, control is returned to the main computer program to read the next loading increment. Thus, each load step in this analysis is treated as a separate problem requiring solution of the entire model. The size of a typical micromechanics model is normally less than 3000 degrees of freedom. However, during a given loading simulation, that model may be solved 30-40 times, depending on the number of loading increments and crack propagation iterations.

Three different two-dimensional finite element meshes were used for this present micromechanics analysis. Each mesh was composed of constant strain triangular elements. All three meshes modeled composite materials containing a 60 percent fiber volume fraction. The first mesh, shown in Figure 5, is a coarse model used to predict stressfields from which the composite elastic constants and thermal expansion coefficients may be calculated. This mesh contains only 113 nodes and 192 elements. It is not suitable for conducting crack propagation studies as a single element represents a significant portion of the model. However, problems analyzed with this mesh can be solved very quickly for initial estimates of stress states and composite material properties.

The finite element mesh shown in Figure 6 is composed of 384 nodes and 704 elements. Because these elements are much smaller relative to the size of the entire finite element model, failure of one element is much more representative of the microcracks occurring in real composite materials. Note that there are three distinct regions, i.e., the fiber, the matrix, and the interface in the mesh shown as Figure 6. For the carbon-carbon micromechanics model, the fiber was assumed to be linear elastic orthotropic carbon fiber and the matrix was assumed to be isotropic carbon. The interface was assumed to be perfectly bonded. Therefore the interface zone in Figure 6 is isotropic matrix material. This model will be referred to as the isotropic carbon matrix model throughout the remainder of this report.

In order to model the effects of an oriented matrix sheath, the interface region of Figure 6 was extended and enlarged for the mesh shown in Figure 7. The axial sheath model shown in Figure 7 is composed of 417 nodes and 768 elements, including 384 elements in the sheath region. The sheath was assumed to consist of transversely isotropic

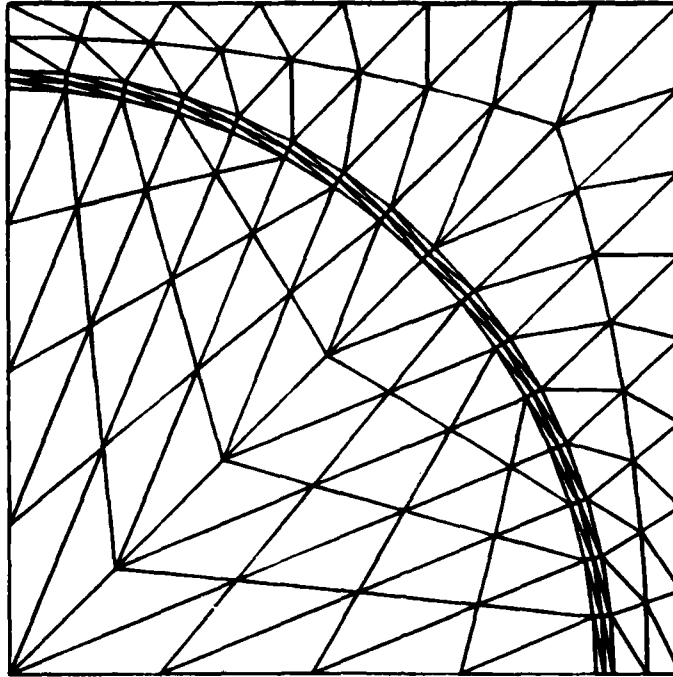


Figure 5. Quarter Fiber Finite Element Micromechanics Mesh Used for Initial Stress State and Composite Material Property Estimates.

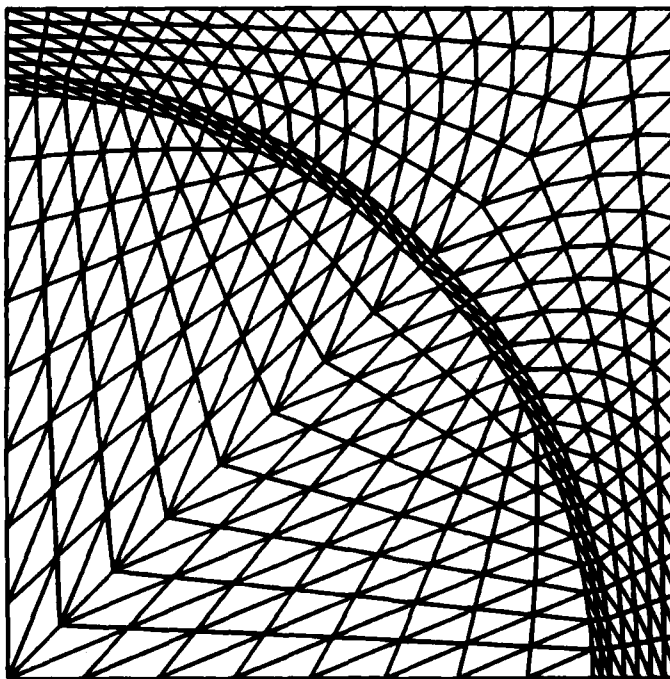


Figure 6. Finite Element Mesh Used for the Isotropic Carbon Matrix Micromechanics Model.

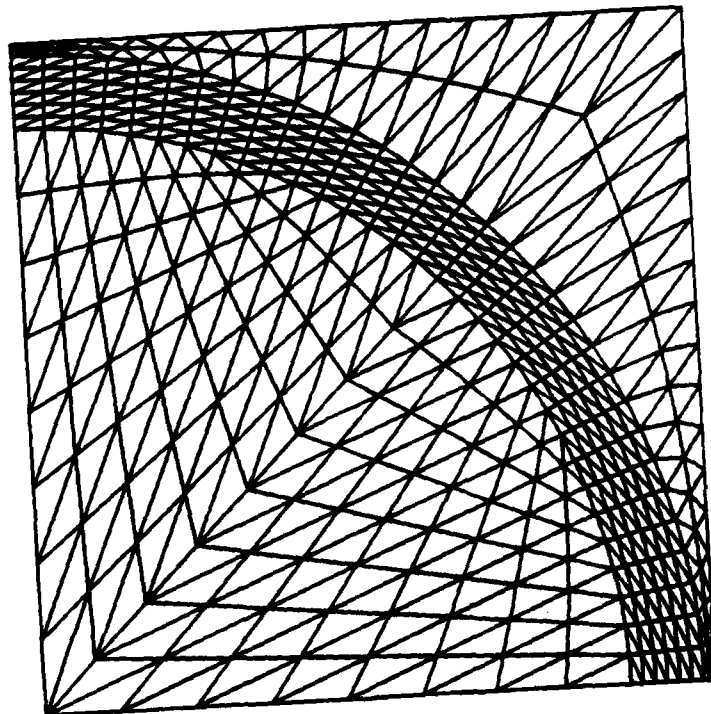


Figure 7. Finite Element Mesh Used for the Axial Sheath
Micromechanics Model.

carbon oriented parallel to the axial or fiber direction. Thus it was directly analogous to a micromechanics model of greater fiber volume. However, strength values assumed for the interface region had a significant effect on the predicted carbon-carbon fiber bundle properties because these values controlled crack propagation in the model. Discussion of the constituent material properties used in this present work is presented in Section 4 of this report along with the results of the micromechanics analysis.

The carbon-carbon composite fiber bundles modeled in this present micromechanics work were assumed to be globally transversely isotropic. Thus it was necessary to simulate four types of mechanical loading previously shown in Figure 3, in order to describe thermomechanical response of these composite fiber bundles. The mechanical loads represented longitudinal tension (σ_1), transverse tension (σ_2), longitudinal shear (τ_{12}), and transverse shear (τ_{23}). Prior to initiating mechanical loading increments, temperature increments were used to simulate cooldown from the final processing temperature. Simulation of specimen reheating to a desired temperature was then performed as necessary. Thus, the stress-strain response of a unidirectional composite material was predicted, due to any of the four types of applied stress in any selected hygrothermal environment, including effects of processing-induced thermal residual stresses and cracks. For composite materials possessing sensitivity to absorbed moisture, moisture increments may also be included. However, moisture loading increments were not used in this present analysis as moisture does not influence the strain state in carbon-carbon composites.

Predicted stress-strain response including elastic coefficients, thermal expansion coefficients, and strengths for unidirectional carbon-carbon fiber bundles were then used as input for the three-dimensional minimechanics finite element analysis. Input constituent material properties and results of the micromechanics analysis are summarized in Section 4.

3.3 Three Dimensional Finite Element Minimechanics Unit Cell Analysis

A three-dimensional finite element analysis was used to perform the minimechanics unit cell analysis presented in this report. The computer program implementing this analysis, called WY03D, was written at the

University of Wyoming as part of this present research effort. The finite element program contains many of the features present in the generalized plane strain analysis described previously. These features, extended to three-dimensional analysis, include temperature dependent elastoplastic material properties, incremental loading, and crack initiation and propagation schemes.

The carbon-carbon unit cell model used to perform the micromechanics analysis for this present program is shown in Figure 8. This unit cell is composed of three orthogonal fiber bundles oriented in the x-, y-, and z-coordinate directions. The z-direction fiber bundle is 2.5 times larger than the x- or y-fiber bundles, to model the construction of Fiber Materials, Inc. Billet No. 2696 tested during an earlier phase of this present research effort [1]. The unit cell dimensions for this billet are also shown in Figure 8.

A finite element mesh used to represent the unit cell model of Figure 8 is shown in Figure 9. This mesh is composed of 425 nodes and 64 elements. These elements are 20-node quadratic isoparametric brick elements. Nodes are positioned at the 8 corners and 12 mid-edges of each element. A higher order element was used in this three-dimensional model in order to obtain better estimates of the local stress state within the material model. Crack propagation takes place via a node division technique, rather than a failed element technique as was used in the generalized plane strain micromechanics analysis. Therefore, modeling detail does not require a large number of elements.

Elastoplastic stress-strain behavior can only be modeled for isotropic materials using the generalized plane strain micromechanics analysis described previously. In the three-dimensional finite element analysis, elastoplastic behavior is extended to anisotropic materials as well.

Details of the analysis have been described elsewhere [51,52]; therefore a detailed explanation will not be repeated here. This three-dimensional analysis method uses an "effective stress-effective strain" constitutive relation to represent inelastic behavior in an anisotropic region. A quadratic form in the six components of stress, similar to Hill's yield condition [53], is chosen in the form

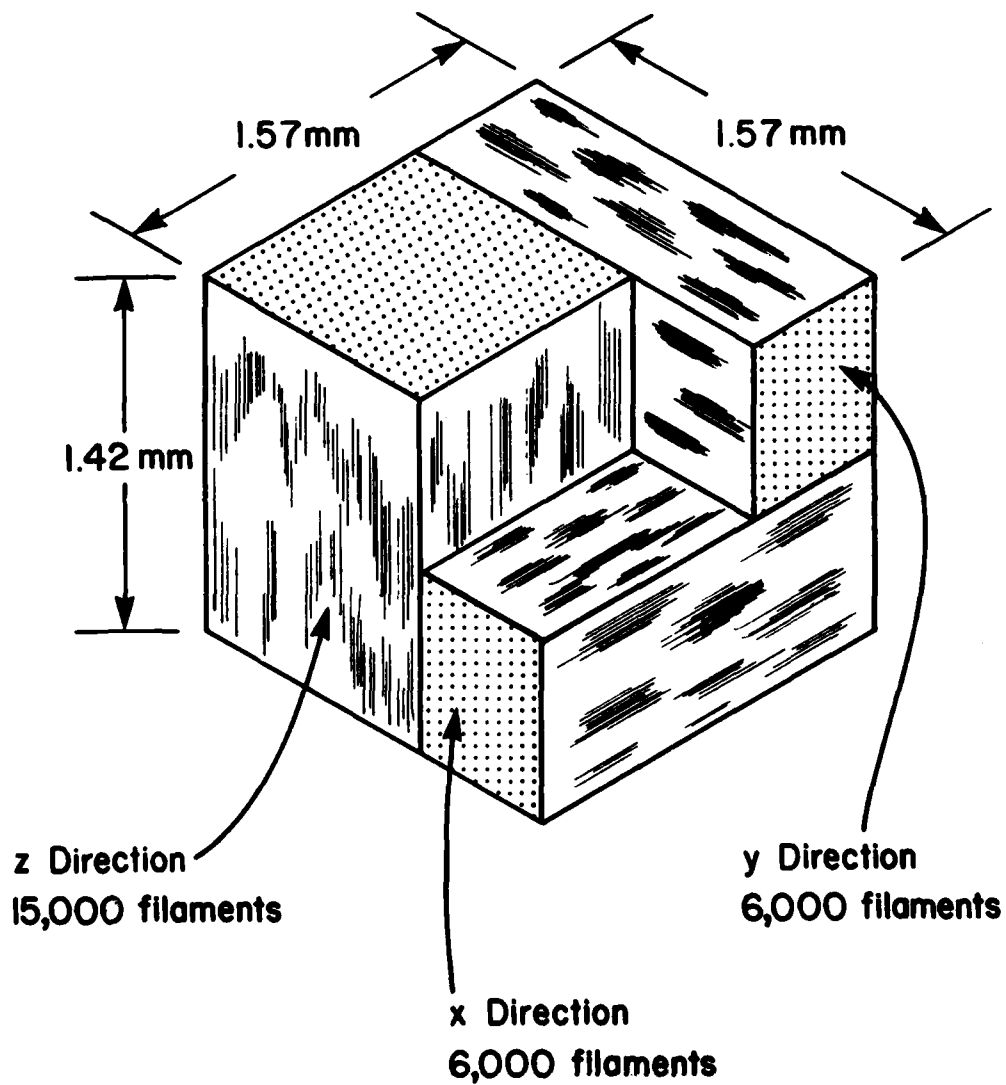


Figure 8. Three-Dimensional Cartesian Weave Carbon-Carbon Unit Cell. (Representative of FMI Billet No. 2696).

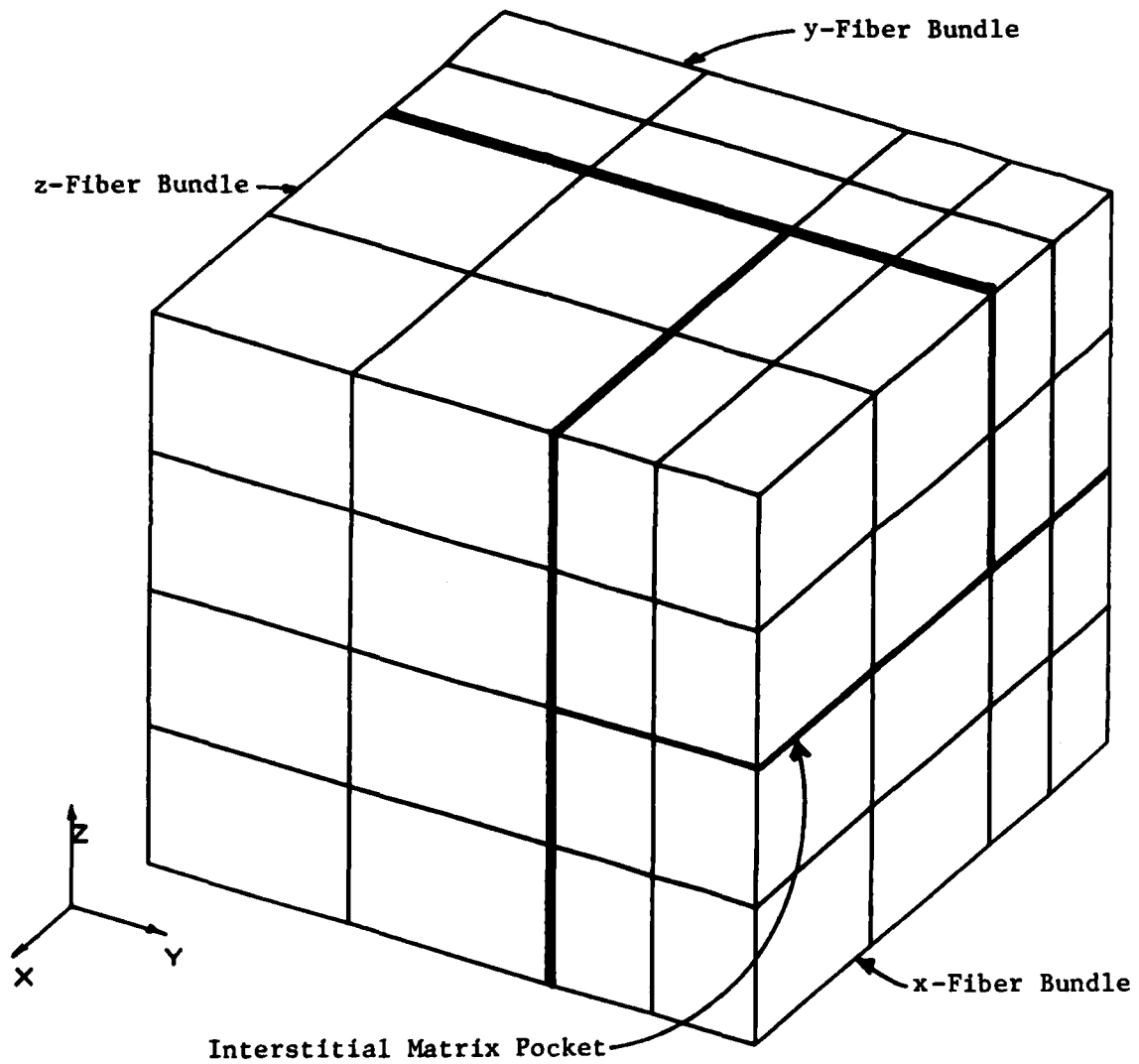


Figure 9. Minimechanics Unit Cell Finite Element Mesh.

$$2f(\sigma_{ij}) = F(\sigma_2 - \sigma_3)^2 + G(\sigma_3 - \sigma_1)^2 + H(\sigma_1 - \sigma_2)^2 \quad (3)$$

$$+ 2L r_{23}^2 + 2M r_{13}^2 + 2N r_{12}^2 = 1$$

where F, G, H, L, M, and N are parameters characteristic of the current state of anisotropy. In the present study, these parameters of anisotropy are allowed to vary with changes in temperature. Inelastic stress-strain behavior need not be only plastic deformation but can also represent permanent deformation due to microcracking.

The form of Eq. (3) is valid only when the principal axes of anisotropy are taken to be the axes of reference; otherwise the stress components must be transformed. The functional dependence of the parameters of anisotropy on temperature (and moisture, if necessary) follows directly when the yield stresses are expressed as functions of temperature (and/or moisture content).

The obvious association, implied by the term "work-hardening," between the work used to produce plastic flow and the hardening created, suggests a hypothesis that the degree of hardening is a function only of the total plastic work, and is otherwise independent of the strain path. In order for plastic work to be performed, the state of stress must be on the yield surface, i.e., the stress state must also satisfy the condition given by Eq. (3). To enforce this constraint, the Lagrange multiplier $d\lambda$ is used [54].

Relating the six parameters of anisotropy to the strain history is a complicated problem. It can be simplified, however, by the assumption that the yield stresses must increase in proportion with strain hardening. This assumption is justified by the fact that the directions of anisotropy in fibrous composites remain effectively the same during deformation. By analogy with the von Mises criterion for isotropic materials, Hill [51] suggested that if there is a functional relation between the equivalent stress $\bar{\sigma}$ and the work W , there must be one between $\bar{\sigma}$ and the effective (or equivalent) strain increment $d\bar{\epsilon}$. This is the analogue of the equivalent stress-equivalent strain curve for isotropic materials, the area under which is equal to the work per unit volume. These equations are of the form

$$\begin{aligned} \bar{\sigma}^2 &= \frac{3}{2} \left[\frac{h^2}{F + G + H} \right] \\ &= \frac{3}{2} \left[\frac{F(\sigma_2 - \sigma_3)^2 + G(\sigma_3 - \sigma_1)^2 + H(\sigma_1 - \sigma_2)^2}{F + G + H} \right. \\ &\quad \left. + \frac{2Lr_{23}^2 + 2Mr_{13}^2 + 2Nr_{12}^2}{F + G + H} \right] \end{aligned} \quad (4)$$

and

$$\begin{aligned} d\bar{\epsilon} &= \frac{2}{3} \left[F + G + H \right]^{1/2} \left[\frac{F(Gd\epsilon_2 - Hd\epsilon_3)^2 + G(Hd\epsilon_3 - Fd\epsilon_1)^2 + H(Fd\epsilon_1 - Gd\epsilon_2)^2}{(FG + GH + HF)^2} \right. \\ &\quad \left. + \frac{2(dy_{23})^2}{L} + \frac{2(dy_{13})^2}{M} + \frac{2(dy_{12})^2}{N} \right]^{1/2} \end{aligned} \quad (5)$$

If an effective stress-effective plastic strain curve is then constructed, the slope of such a curve at any point will be

$$H' = \frac{d\bar{\sigma}}{d\bar{\epsilon}^P} \quad (6)$$

Continuing in this manner, as described in [51], yields the desired form for the stress-strain relation, i.e.,

$$(d\sigma) = [C^P] (d\epsilon) \quad (7)$$

where

$$[C^P] = \begin{bmatrix} C_{11} - \frac{A_1^2}{B} & C_{12} - \frac{A_1 A_2}{B} & C_{13} - \frac{A_1 A_3}{B} & -\frac{A_1 A_4}{B} & -\frac{A_1 A_5}{B} & -\frac{A_1 A_6}{B} \\ & C_{22} - \frac{A_2^2}{B} & C_{23} - \frac{A_2 A_3}{B} & -\frac{A_2 A_4}{B} & -\frac{A_2 A_5}{B} & -\frac{A_2 A_6}{B} \\ & & C_{33} - \frac{A_3^2}{B} & -\frac{A_3 A_4}{B} & -\frac{A_3 A_5}{B} & -\frac{A_3 A_6}{B} \\ \text{Symmetric} & & & C_{44} - \frac{A_4^2}{B} & -\frac{A_4 A_5}{B} & -\frac{A_4 A_6}{B} \\ & & & & C_{55} - \frac{A_5^2}{B} & -\frac{A_5 A_6}{B} \\ & & & & & C_{66} - \frac{A_6^2}{B} \end{bmatrix} \quad (8)$$

is the plastic stiffness matrix, and

$$B = \frac{4}{9} \bar{\sigma}^2 H' + A_1 \sigma_1^* + A_2 \sigma_2^* + A_3 \sigma_3^* + 2A_4 \tau_{23}^* + 2A_5 \tau_{13}^* + 2A_6 \tau_{12}^* \quad (9)$$

where the A_i ($i = 1, \dots, 6$) are elements of the (A) vector, and

$$\begin{aligned} \sigma_1^* &= [H(\sigma_1 - \sigma_2) + G(\sigma_1 - \sigma_3)] / (F + G + H) \\ \sigma_2^* &= [F(\sigma_2 - \sigma_3) + H(\sigma_2 - \sigma_1)] / (F + G + H) \\ \sigma_3^* &= [G(\sigma_3 - \sigma_1) + F(\sigma_3 - \sigma_2)] / (F + G + H) \\ \tau_{23}^* &= L\tau_{23} / (F + G + H) \\ \tau_{13}^* &= M\tau_{13} / (F + G + H) \\ \tau_{12}^* &= N\tau_{12} / (F + G + H) \end{aligned} \quad (10)$$

For an orthotropic material, i.e., a material with three planes of symmetry,

$$(A) = \begin{pmatrix} C_{11}\sigma_1^* + C_{12}\sigma_2^* + C_{13}\sigma_3^* \\ C_{12}\sigma_1^* + C_{22}\sigma_2^* + C_{23}\sigma_3^* \\ C_{13}\sigma_1^* + C_{23}\sigma_2^* + C_{33}\sigma_3^* \\ 2C_{44}\tau_{23}^* \\ 2C_{55}\tau_{13}^* \\ 2C_{66}\tau_{12}^* \end{pmatrix} \quad (11)$$

To apply this method of analysis to fiber-reinforced composites, the material properties in the 1-, 2-, and 3- directions are obtained from the previously described micromechanics analysis in this research. If the material is transversely isotropic as in the present work, the properties in the 2- and 3-directions are equal. For mathematical consistency with the formulation, a relationship between the effective stress and the effective strain is required. Furthermore, the dependence of the material properties on temperature (moisture) is required if hygrothermal loadings are to be studied, and the actual material response under varying conditions of environment is to be considered.

Since the shape of an effective stress-effective strain curve is similar to a uniaxial tensile or shear stress-strain curve, an equation similar to the Richard-Blacklock form shown as Eq. (2) was written,

$$\bar{\sigma} = \frac{\bar{E}\bar{\epsilon}}{\left[1 + \left|\frac{\bar{E}\bar{\epsilon}}{\bar{\sigma}_0}\right|^n\right]^{\frac{1}{n}}} \quad (12)$$

where $\bar{\sigma}$ is the effective stress and $\bar{\epsilon}$ is the effective strain, as defined previously. The two independent parameters $\bar{\sigma}_0$ and n , together

with the third parameter \bar{E} , which is the initial slope of the curve, were selected to best fit the data.

By fitting Eq. (12) to effective stress-effective strain curves obtained for different temperatures, a functional relationship of the parameters \bar{E} , $\bar{\sigma}_0$, and n in temperature was established. In a similar manner, functional relationships were also found for all other material properties.

The generalized plane strain micromechanics analysis was used to predict stress-strain response for longitudinal tension, transverse tension, longitudinal shear and transverse shear loadings at room temperature, 815°C, and 1649°C. The anisotropy parameters F, G, H, L, M and N were calculated as in Reference [51], i.e.,

$$\begin{aligned}
 2F &= \frac{1}{(\sigma_2^y)^2} + \frac{1}{(\sigma_3^y)^2} - \frac{1}{(\sigma_1^y)^2} \\
 2G &= \frac{1}{(\sigma_3^y)^2} + \frac{1}{(\sigma_1^y)^2} - \frac{1}{(\sigma_2^y)^2} \\
 2H &= \frac{1}{(\sigma_1^y)^2} + \frac{1}{(\sigma_2^y)^2} - \frac{1}{(\sigma_3^y)^2} \\
 2L &= \frac{1}{(\tau_{23}^y)^2}, \quad 2M = \frac{1}{(\tau_{13}^y)^2}, \quad 2N = \frac{1}{(\tau_{12}^y)^2}
 \end{aligned} \tag{13}$$

where σ_i^y and τ_i^y are "yield" stresses with respect to the material coordinate axes. Ideally the four curves, representing each of the four different types of loading, should merge into one effective stress-effective strain curve with the proper selection of the anisotropy parameters in Eq. (12). Numerical results generated by the generalized plane strain micromechanics analysis, converted to effective stress-effective strain form, are discussed in Section 5 of this report.

Damage initiation and propagation in this three-dimensional micromechanics analysis was modeled by use of a node separation technique as opposed to the failed element approach used in the generalized plane strain micromechanics analysis. As in the generalized plane strain analysis, incremental steps were used to apply thermal or mechanical

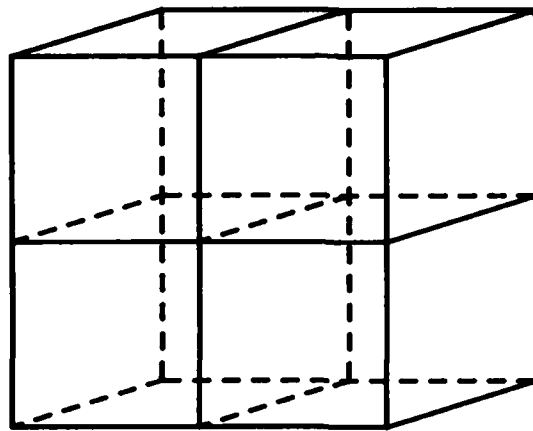
loads. During each load increment the stress state within the model was computed. By use of an appropriate failure criterion, the condition of each node was determined. For the present minimechanics analysis, a maximum stress failure criterion was used. If a node was determined to have failed, the plane of failure was then determined. A new node was created at the same position as the previous node and the connectivity arrays were altered to divide the elements on either side of the failure plane. This process is shown for four elements in Figure 10. Friction due to sliding at the failure plane was not included in the analysis, nor was there a capability for modeling crack closure. These are important considerations and are being studied for future modifications to this finite element analysis computer program.

3.4 Summary of Modeling Procedure

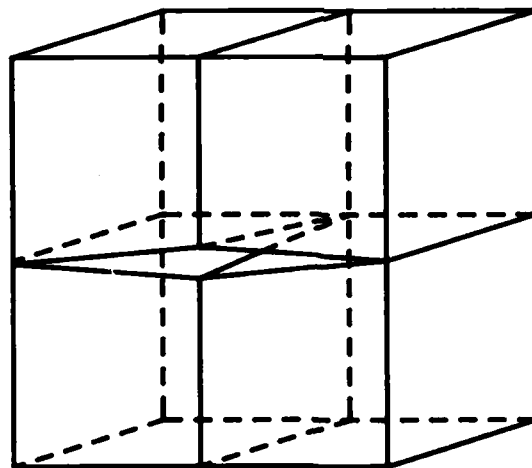
Modeling of the bulk thermomechanical behavior for a three-dimensional cartesian-weave carbon-carbon was accomplished by the following steps:

- 1) Appropriate constituent material properties for use in the generalized plane strain micromechanics analysis WYO2D were chosen. These properties included elastic coefficients, thermal expansion coefficients, and stress strain behavior for the fiber, matrix, and sheath constituents.
- 2) Thermomechanical properties of the fiber bundles under appropriately chosen environmental and loading conditions were calculated. Effects which were modeled included variations in fiber volume content, presence of an oriented sheath, and parametric variations of constituent material properties.
- 3) A set of micromechanics calculated fiber bundle material properties as well as material properties for the bulk carbon matrix were used in the three-dimensional unit cell minimechanics analysis to predict the material properties for a three-dimensional orthogonal carbon-carbon material.

Constituent material properties and micromechanics results are presented in Section 4 of this report. Results of the unit cell minimechanics analysis are included in Section 5.



a) Uncracked Model



b) Separated Node

Figure 10. Crack Propagation by a Node Separation Technique.

SECTION 4

MICROMECHANICS ANALYSIS

4.1 Constituent Properties

A major difficulty in conducting this micromechanics and mini-mechanics modeling of carbon-carbon materials was determining consistent sets of constituent material properties for use in the analyses. For example, tests to measure the axial strength and stiffness of individual graphite fibers have been performed and data were available in the literature, but transverse properties for these same fibers have not been directly measured. Both sets of properties were needed for the micromechanics analysis. For this analysis, it was necessary to rely on the use of limited existing information, plus educated estimates for those fiber properties which have not been measured.

Matrix constituent material properties were more easily obtained. For organic matrix composites it is possible to find or measure all of the pertinent material properties. Indeed properties for a large number of different polymer matrix systems have been measured at the University of Wyoming [55-57] in order to perform similar micromechanics modeling studies. However, measuring the properties of a carbon matrix poses additional difficulties. First, carbon can exist in different forms, with bulk material properties ranging from isotropic to highly oriented anisotropic. Second, the temperature range of interest for carbon is much greater than for many other materials. This makes characterization over the temperature range of use more difficult. The number of laboratories capable of routinely making such measurements is correspondingly smaller. Finally, micromechanical behavior, particularly the strength of carbon as a matrix material, is probably quite different from the bulk behavior of carbon as measured by tests on ATJ-S graphite.

For purposes of this present research, the most complete documented set of constituent material property values available was obtained from References [11-13]. The investigators at Materials Science Corporation assembled a set of thermoelastic data for Hercules HM fibers and carbon matrix, the latter based on properties measured for ATJ-S graphite. Where possible, values used in this present work were taken from experimental data. When experimental data were not available, best

estimates were used. During this present research an extensive effort was made to find the best available sets of experimentally verified constituent material properties. Overall, it was difficult to improve upon the values used by the MSC investigators [11-13]. Therefore, many of the constituent material property values used in this present research correspond to those used in the MSC work. Where possible, original references for the MSC data were examined. Other sources of information were also found in subsequently available literature.

Thermomechanical properties for Hercules HM fibers used in the present numerical calculations are listed in Table 1. Axial modulus values at room temperature were taken from manufacturer's reported data [58], extrapolated to higher temperatures using trends similar to those reported in Reference [12]. Shear moduli and Poisson's ratio values were obtained directly from Reference [13]. The original experimental work was presented in Reference [59]. Axial strengths were assumed to be the same as reported for Thornal 50 fibers in Reference [12].

For use in the WYO2D generalized plane strain micromechanics analysis, these material values were converted to polynomial equations in temperature using regression techniques. Resulting functions are of the form

$$P = C_0 + C_1T + C_2T^2 + C_3T^3$$

where P is a specific material property of interest, T is the temperature, and the C_i are regression coefficients. Equations defining the Hercules HM fiber longitudinal tensile modulus E_{11} , transverse tensile modulus E_{22} , longitudinal shear modulus G_{12} , longitudinal Poisson's ratio ν_{12} and transverse Poisson's ratio ν_{23} are plotted as functions of temperature in Figures 11 through 14, respectively. Longitudinal tensile strengths S_{11}^{ut} are plotted in Figure 15. Values from Table 1 used to find the regression coefficients are also plotted in the appropriate figures marked with triangles. As can be seen in Figures 11 through 15, the polynomial equations describe the assumed input data values well.

Thermal expansion data for the HM carbon fiber are listed in Table 2, taken from Reference [13]. Longitudinal thermal expansion data were originally from Reference [59]. The MSC investigators estimated transverse thermal expansion behavior. Thermal strain values listed in

TABLE 1

Mechanical Properties for Hercules HM Carbon Fibers [12,13,58,59]

Temperature (°C)	Tensile Moduli		Shear Modulus G_{12} (GPa) (Msi)	Poisson's Ratios		Tensile Strength S_{11}^{ut} (ksi) (GPa)
	E_{11} (GPa) (Msi)	E_{22} (GPa) (Msi)		ν_{12}	ν_{23}	
24	359	10.3	14.4	0.26	0.36	1.86
538	372	10.7	14.8	0.26	0.36	1.63
1093	363	11.4	15.9	0.26	0.36	1.52
1649	323	13.0	18.1	0.32	0.39	1.63
2204	245	11.7	16.3	0.39	0.44	-
2760	108	6.8	9.5	0.45	0.47	-

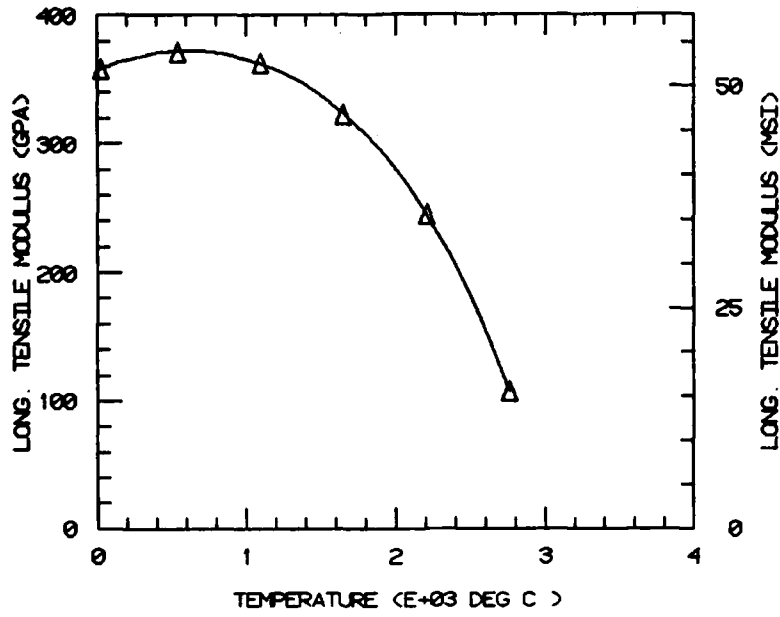


Figure 11. Longitudinal Tensile Modulus E_{11} as a Function of Temperature for Hercules HM Carbon Fiber.

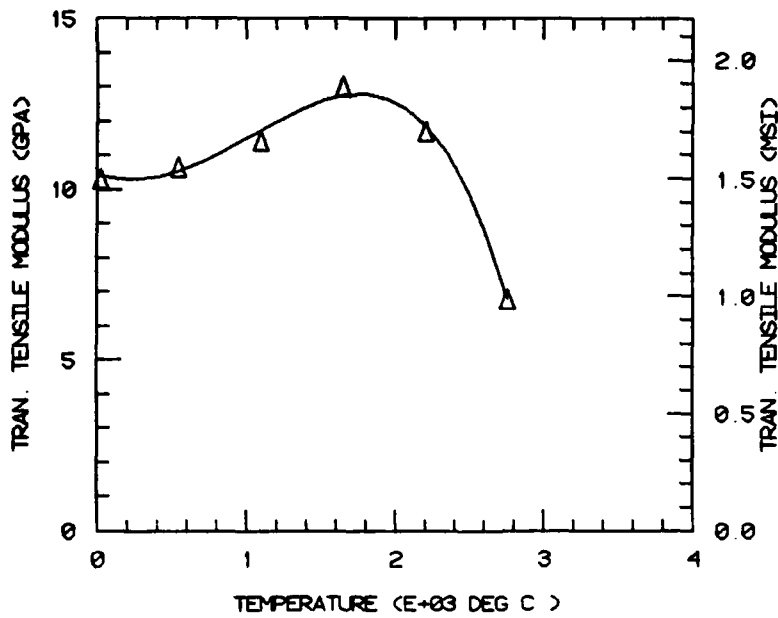


Figure 12. Transverse Tensile Modulus E_{22} as a Function of Temperature for Hercules HM Carbon Fiber.

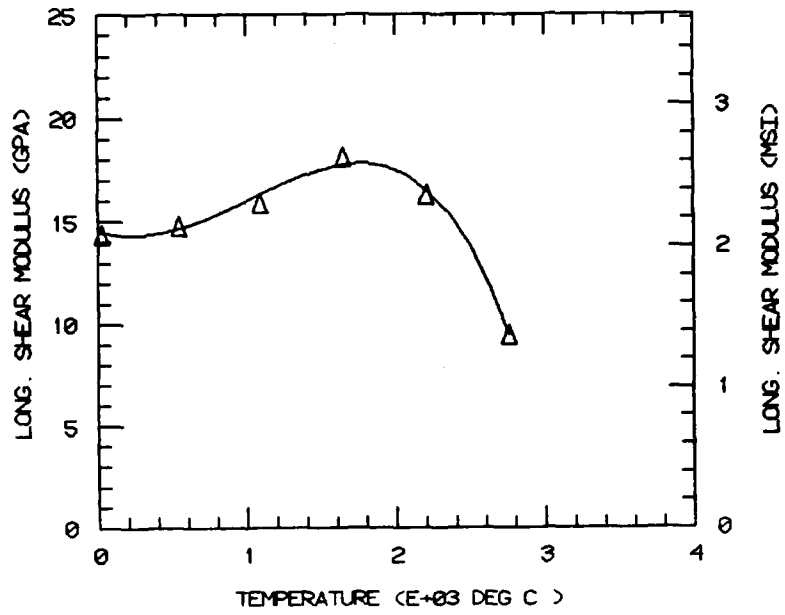


Figure 13. Longitudinal Shear Modulus G_{12} as a Function of Temperature for Hercules HM¹² Carbon Fiber.

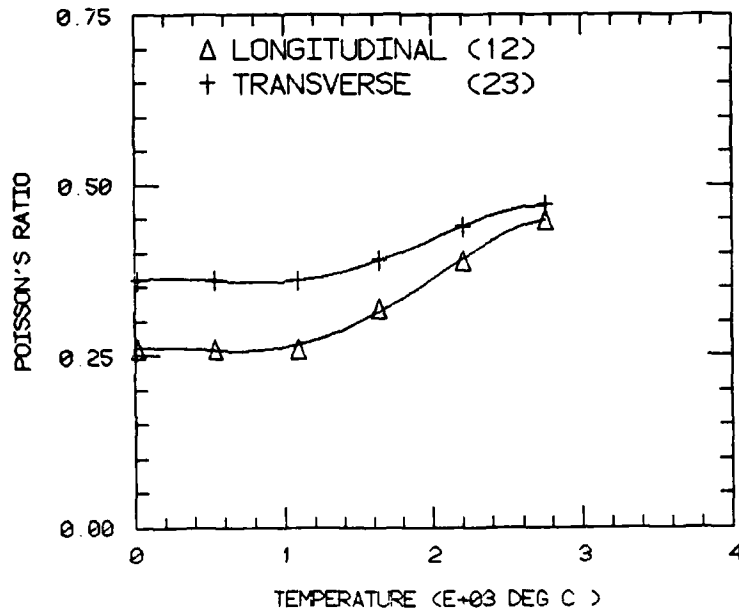


Figure 14. Longitudinal and Transverse Poisson's Ratios ν_{12} and ν_{23} as Functions of Temperature for Hercules HM¹² Carbon Fiber.

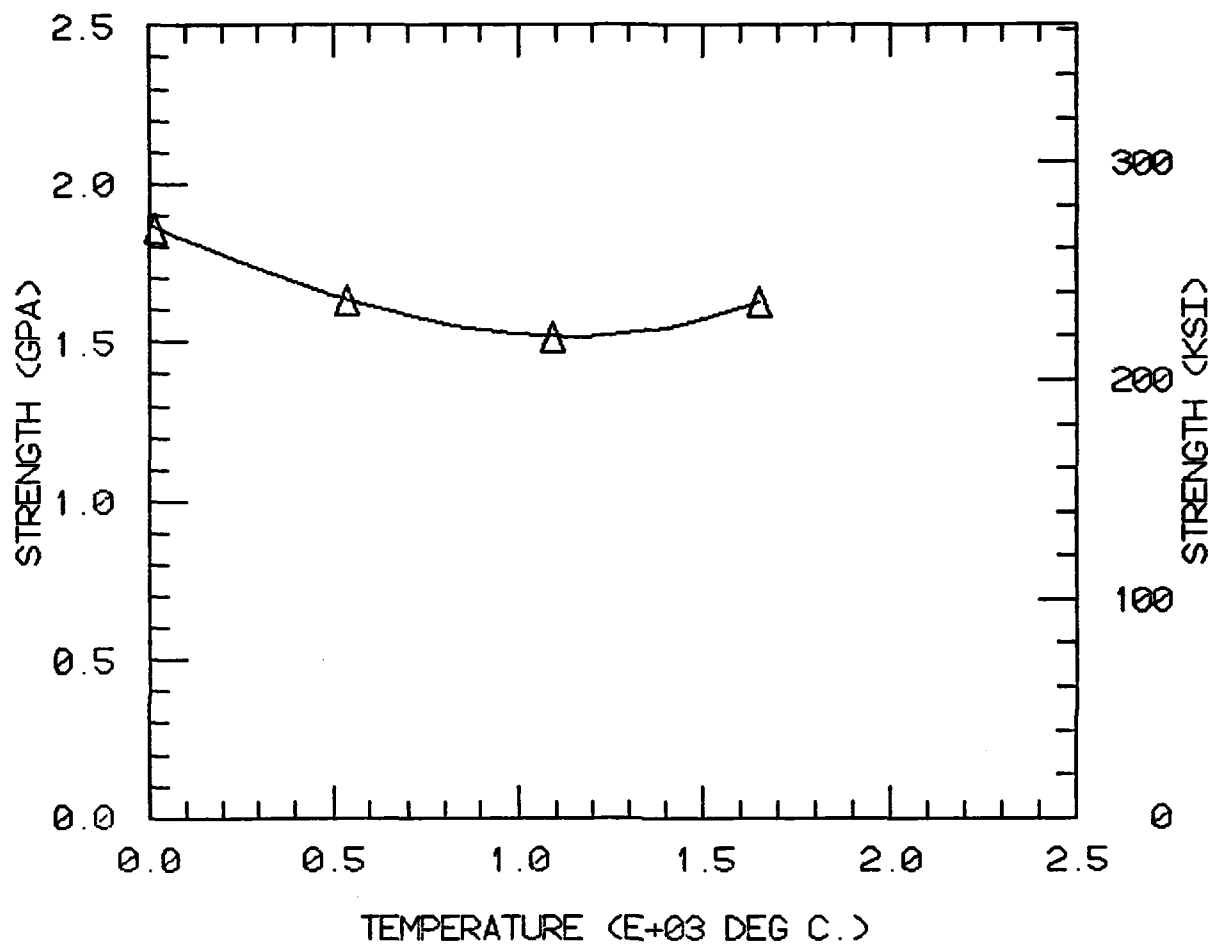


Figure 15. Longitudinal Tensile Strength S_{11}^{ut} as a Function of Temperature for Hercules HM Carbon Fiber.

TABLE 2

Thermal Expansion Properties for Hercules HM Carbon Fibers [13]

Temperature °C	Thermal Strain		Thermal Expansion Coefficient	
	ϵ_{11} (10^{-3})	ϵ_{22} (10^{-3})	α_{11} ($10^{-6}/^{\circ}\text{C}$)	α_{22} ($10^{-6}/^{\circ}\text{C}$)
24	0.00	0.0	-0.76	7.9
538	-0.19	5.0	0.03	11.4
1093	0.05	12.2	0.74	13.5
1649	0.63	20.0	1.43	16.0
2204	1.66	30.3	2.25	20.9
2760	3.29	44.2	3.34	30.4

Table 2 are plotted as functions of temperature in Figures 16 and 17. As was done for the stiffness coefficients, polynomials in temperature were regression fit to the strain data and are plotted as solid curves in Figures 16 and 17. The first derivatives of these polynomials represent functions describing the thermal expansion coefficients α_{11} and α_{22} , plotted as functions of temperature in Figures 18 and 19, with selected values listed in Table 2.

As can be seen in Figure 19, the assumed transverse thermal expansion coefficient at 1000°C is approximately $13.2 \times 10^{-6}/^{\circ}\text{C}$. Marciniak and Rozploch [60] reported measured transverse thermal expansion coefficients for carbon fibers ranging from 22 to $34 \times 10^{-6}/^{\circ}\text{C}$ at 1000°C. These investigators used a transmission electron microscope with a furnace stage to measure radial dimensional changes of a PAN precursor based carbon fiber. Thus, the assumed HM carbon fiber transverse thermal expansion coefficient plotted in Figure 19 agrees reasonably well with these experimentally measured values. The authors of Reference [60] reported major difficulties in making their measurements due to the fibers having noncircular cross sections, which also tended to twist on heating.

In the present generalized plane strain micromechanics analysis, fiber material properties were assumed to be linearly elastic and transversely isotropic. Only axial fiber failure was permitted. Transverse failure of the unidirectional carbon-carbon composite was assumed to occur within the matrix material. Therefore, fiber failure was defined by a maximum longitudinal stress failure criterion. Regression coefficients used to define the polynomial functions of temperature for each of the Hercules HM carbon fiber material properties are listed in Table 3.

Material properties for carbon as a matrix in carbon-carbon composites have usually been derived from test data on bulk ATJ-S graphite. Two sources of information on ATJ-S were reports by Jortner [61] and Starret, et al. [62]. Investigators at MSC [11-13] derived sets of elastic properties and strength estimates from data reported in Reference [62] by averaging "with-grain" and "cross-grain" results. A complete set of estimated thermomechanical elastic data based on Reference [62] was available in Reference [13], and with some

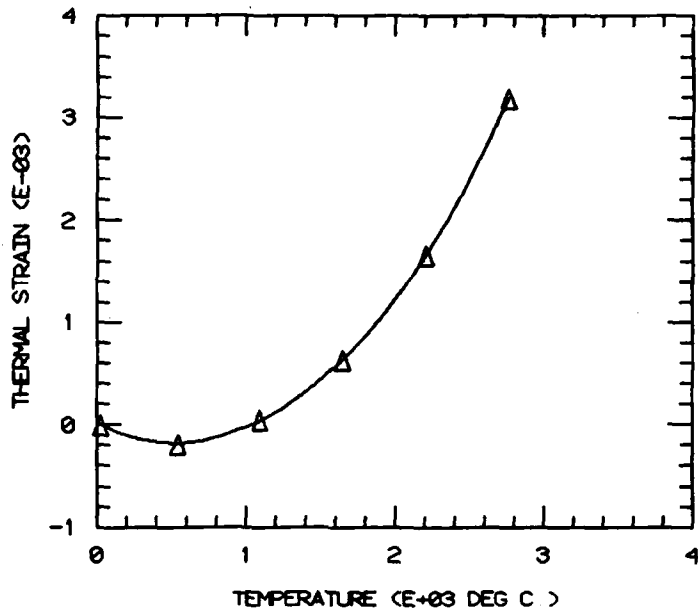


Figure 16. Longitudinal Thermal Strain as a Function of Temperature for Hercules HM Carbon Fiber.

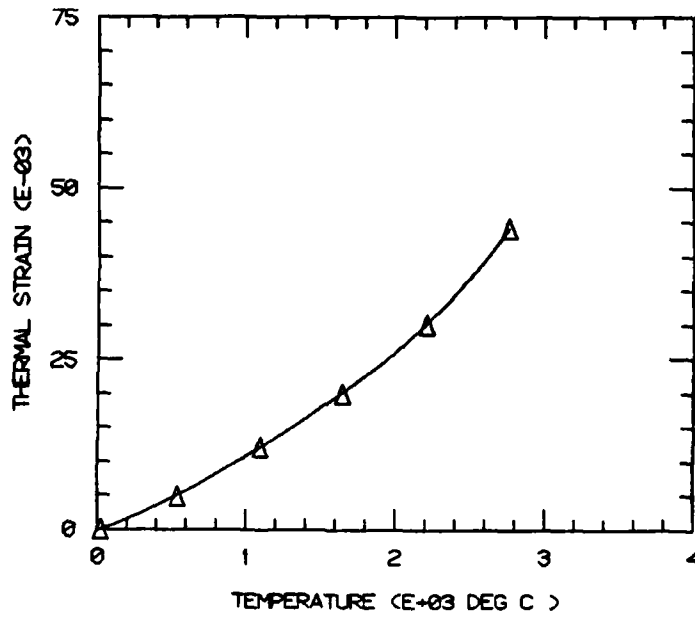


Figure 17. Transverse Thermal Strain as a Function of Temperature for Hercules HM Carbon Fiber.

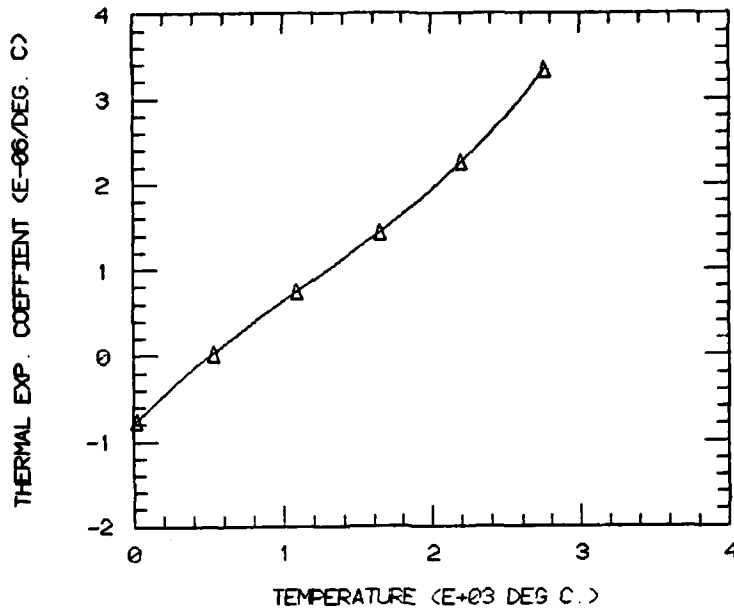


Figure 18. Longitudinal Thermal Expansion Coefficient α_{11} as a Function of Temperature for Hercules HM Carbon Fiber.

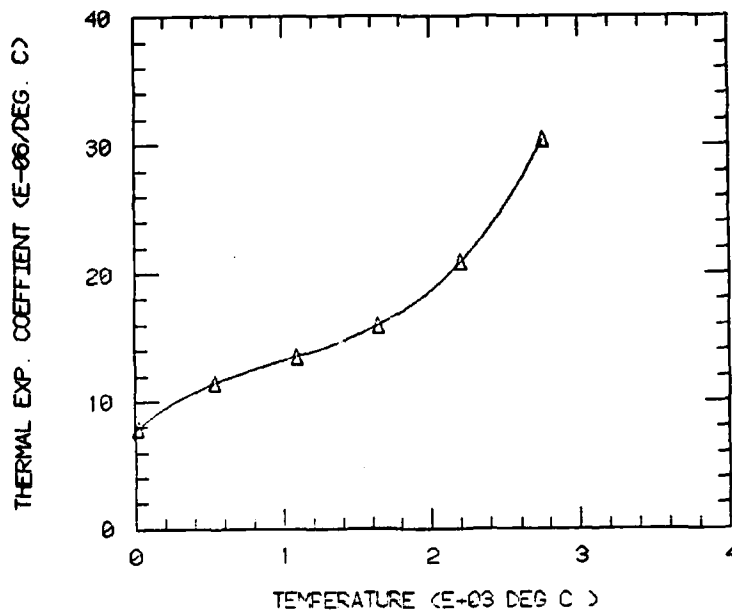


Figure 19. Transverse Thermal Expansion Coefficient α_{22} as a Function of Temperature for Hercules HM Carbon Fiber.

TABLE 3

Thermomechanical Properties for Hercules HM Carbon Fiber
as Functions of Temperature ($^{\circ}\text{C}$)

$$\text{Property} = C_0 + C_1T + C_2T^2 + C_3T^3 + C_4T^4$$

Property	C_0	C_1	C_2	C_3	C_4
E_{11} (psi)	5.18×10^7	7.35×10^3	-6.69×10^0	1.04×10^{-3}	-4.74×10^{-7}
E_{22} (psi)	1.51×10^6	-1.67×10^2	4.29×10^{-1}	-6.95×10^{-5}	-3.22×10^{-8}
G_{12} (psi)	2.10×10^6	-2.70×10^2	6.46×10^{-1}	-1.18×10^{-4}	-4.18×10^{-8}
ν_{12}	2.60×10^{-1}	1.70×10^{-5}	-8.37×10^{-8}	8.55×10^{-11}	-1.75×10^{-14}
ν_{23}	3.59×10^{-1}	3.18×10^{-5}	-9.58×10^{-8}	7.88×10^{-11}	-1.56×10^{-14}
α_{11} ($^{\circ}\text{C}$) $^{-1}$	-7.99×10^{-7}	1.76×10^{-9}	-4.71×10^{-13}	1.38×10^{-16}	-
α_{22} ($^{\circ}\text{C}$) $^{-1}$	7.73×10^{-6}	9.72×10^{-9}	-6.21×10^{-12}	2.07×10^{-15}	-
S_{11}^t (psi)	2.71×10^5	-7.25×10^1	8.13×10^{-3}	1.38×10^{-5}	-

modification, was adopted for use in this present work. However, neither the generalized plane strain micromechanics analysis nor the present three-dimensional micromechanics analysis was limited by an assumption of linear elastic material behavior. Stress-strain behavior reported in Reference [62] was definitely nonlinear, especially at elevated temperatures. Therefore, it was necessary to define the complete stress-strain response for the carbon matrix as well as defining its elastic properties.

The twisted, wrinkled ribbon-like structure of the matrix in a carbon-carbon fiber bundle is not isotropic in localized regions around individual carbon fibers. Indeed, the degree of anisotropy in pyrolytic graphite may be as high as $C_{22}/C_{33} = 30$ or higher [63]. However, it was assumed that the overall micromechanical behavior of the matrix could be approximated as isotropic due to the random orientation of the aligned structure. Near the fibers, this oriented matrix phase is more aligned, forming a sheath, as observed by Evangelides [7,8], Zimmer [64,65] and many others. Indeed, Zimmer has actually tried to control the orientation of this sheath by processing material in the presence of a magnetic field [66]. While Zimmer's procedure did not appear to produce significant improvements in overall fiber bundle material performance, it is an interesting concept.

A final concern in defining constituent material properties was obtaining an estimate for the strength of the matrix phase at the micromechanics scale. Most materials, particularly brittle materials, exhibit far greater strengths when tested as small whiskers than when tested in bulk form. At a micromechanics level, the carbon matrix strength is probably greater than strengths obtained from measurements on bulk ATJ-S material. Matrix strength at a micromechanics scale is still at best only an "educated engineering judgment."

Sets of isotropic carbon matrix material data, from which properties as functions of temperature were derived, are listed in Table 4. These data were taken from Reference [13], based on experiments reported in Reference [62]. Polynomial functions in temperature, regression fit to these numbers, are plotted in Figures 20 through 23. As with the HM fiber thermal strain data reported earlier, a polynomial equation describing isotropic graphite thermal strain behavior, plotted

TABLE 4

Material Properties for the Carbon Matrix
Derived from ATJ-S Graphite Properties [13,62]

Temperature (°C)	Tensile Modulus E (GPa)	Modulus E (Msi)	Poisson's Ratio ν	Thermal Strain ϵ^T (10^{-3})	Thermal Expansion Coefficient α ($10^{-6}/^{\circ}\text{C}$)
24	9.1	1.32	0.11	0.0	2.2
538	9.4	1.36	0.12	1.5	3.6
1093	10.1	1.46	0.13	3.8	4.3
1649	11.4	1.66	0.14	6.2	4.9
2204	10.3	1.50	0.15	9.4	6.4
2760	6.0	0.87	0.17	13.7	9.5

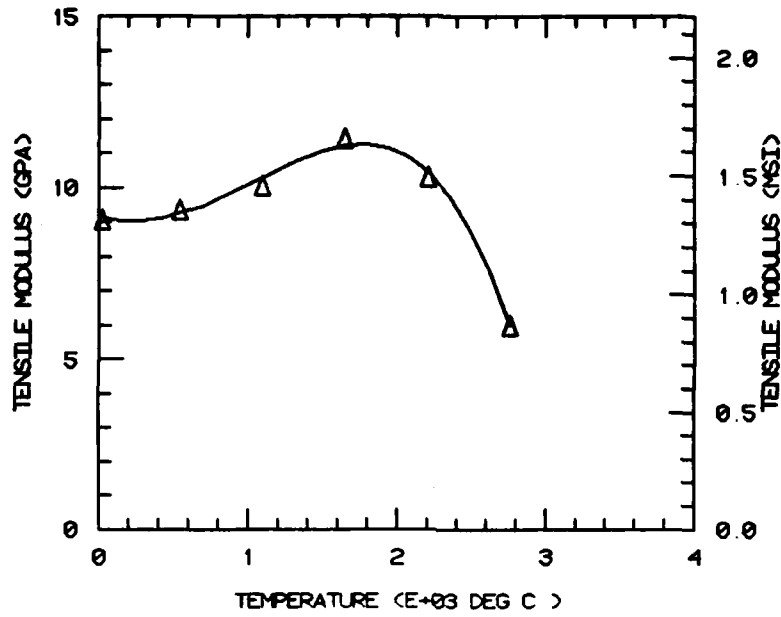


Figure 20. Tensile Modulus E as a Function of Temperature for the Carbon Matrix.

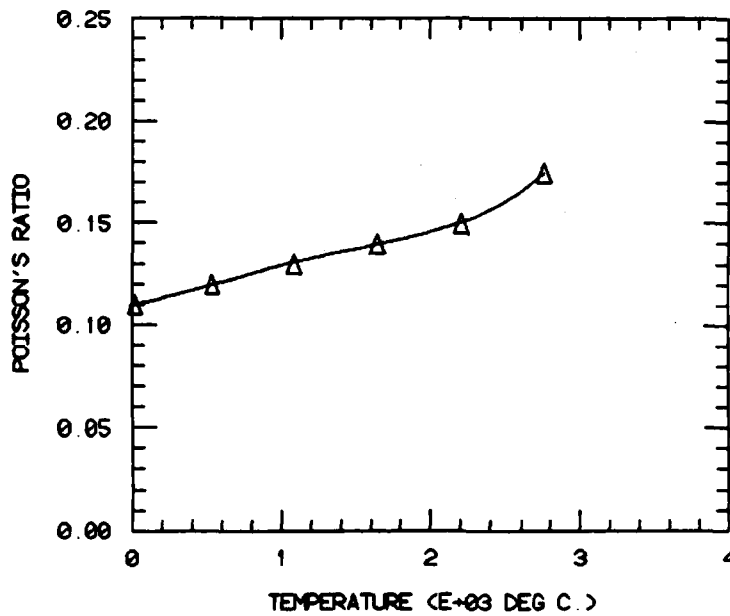


Figure 21. Poisson's Ratio ν as a Function of Temperature for the Carbon Matrix.

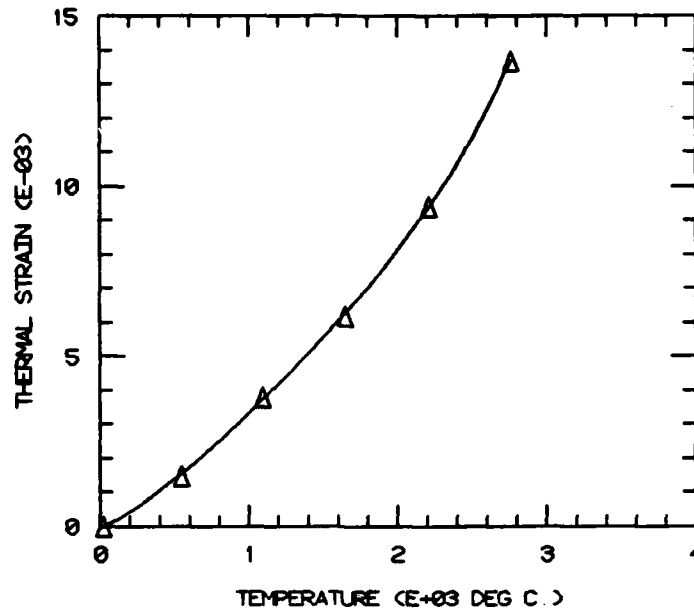


Figure 22. Thermal Strain ϵ^T as a Function of Temperature for the Carbon Matrix.

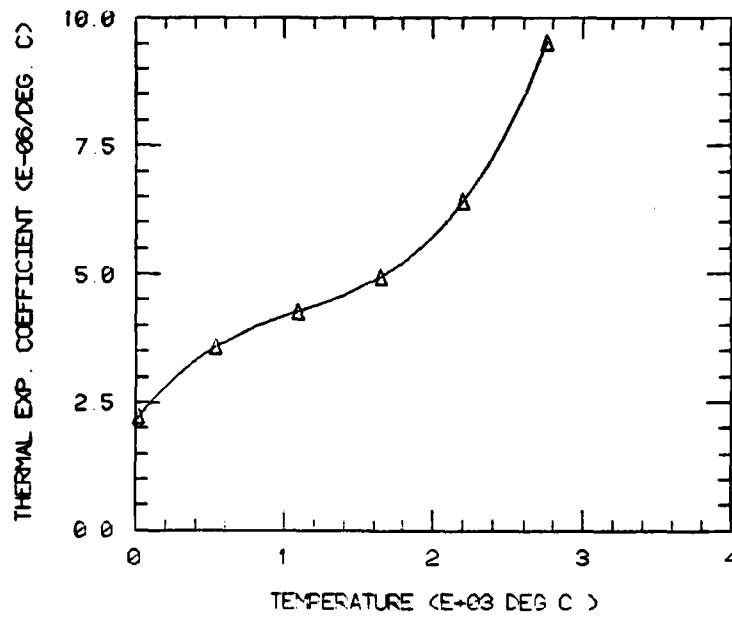


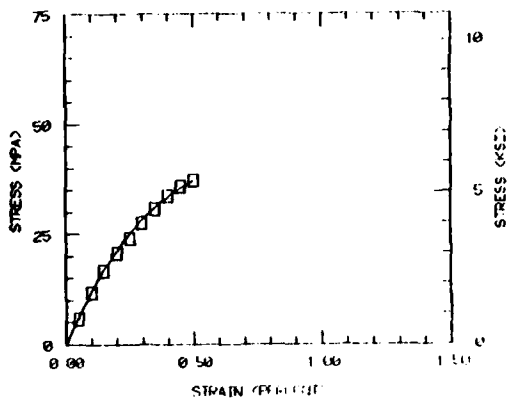
Figure 23. Thermal Expansion Coefficient α as a Function of Temperature for the Carbon Matrix.

in Figure 22, was differentiated to obtain the thermal expansion coefficient α as a function of temperature, plotted in Figure 23.

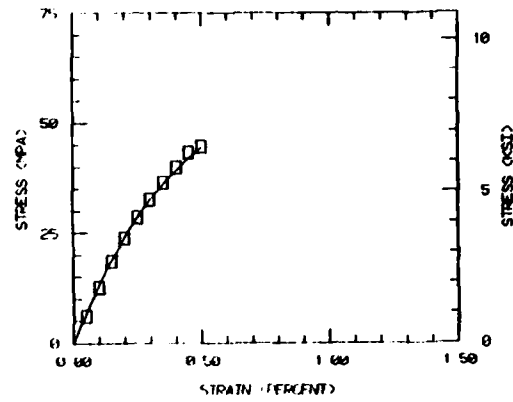
As discussed in Section 3, nonlinear stress-strain behavior is described in the micromechanics and minimechanics analyses by means of a three-parameter exponential Richard-Blacklock equation; the form was previously shown as Eq. (2). With-grain tensile stress strain plots taken from Reference [62] were digitized and plotted in Figure 24 with the Richard-Blacklock description for that data. Stress-strain curves for room temperature, 1093°C, 1649°C and 2204°C are plotted in Figure 24. The three Richard-Blacklock parameters, E_R , n and σ_o , used to represent stress-strain plot shown in Figure 24, as well as the ultimate strain values were in turn regression fit to polynomial functions of temperature and plotted in Figures 25 through 28. These functions were then used to describe stress-strain behavior for the carbon matrix at any temperature, as plotted in Figure 29 for four specific temperatures. It should be noted in Figures 20, 24 and 29 that carbon becomes both stronger and stiffer at elevated temperatures, a trend opposite that of most other engineering materials.

Multiaxial stress-states within the matrix were modeled by use of an octahedral shear stress-octahedral shear strain constitutive relation. This relation is based on energy principles and works very well for modeling metal matrix and polymer matrix composite materials. It has been argued that energy methods based constitutive models do not work well for modeling carbon or carbon-carbon composites [30-32]. Yet the work of Pollock [33] appears to model carbon-carbon mechanical behavior quite well using principles based on energy methods. Other models for behavior of carbon under multiaxial stress states were available, e.g., that of Batdorf [32], and could be used in modeling such as attempted in this program.

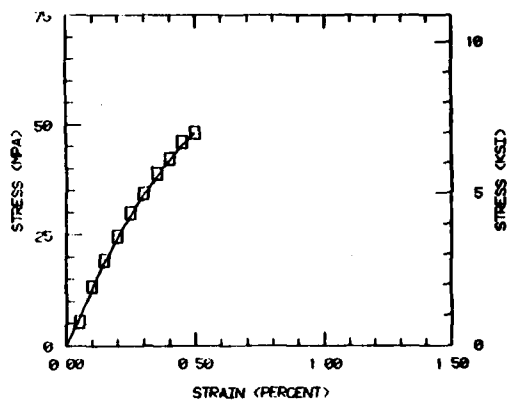
In the MSC work and [11-13] averaged with-grain and across-grain ATJ-S Graphite tensile strength values were used. With-grain tensile strength values were used in the present research, based on an assumption that the matrix should be stronger at the micromechanical scale as opposed to bulk ATJ-S measured strengths. Tensile strength data at various temperatures, taken from References [62,67], are listed in Table 5. Shear strength estimates from Reference [13] were also used.



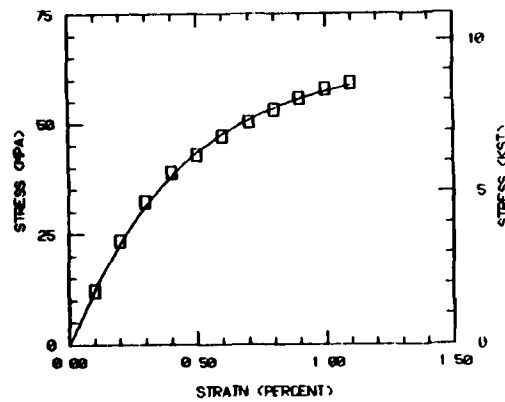
a) Room Temperature



b) Temperature=1093°C



c) Temperature=1649°C



d) Temperature=2204°C

Figure 24. Tensile Stress-Strain Behavior for the Carbon Matrix (ATJ-S Graphite With-Grain Data [58]).

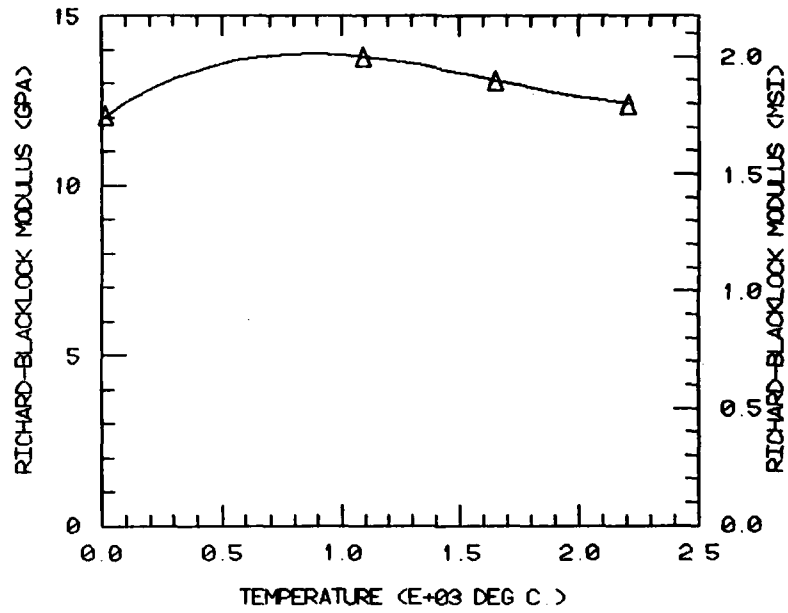


Figure 25. Richard-Blacklock Parameter E_R as a Function of Temperature for the Carbon Matrix.

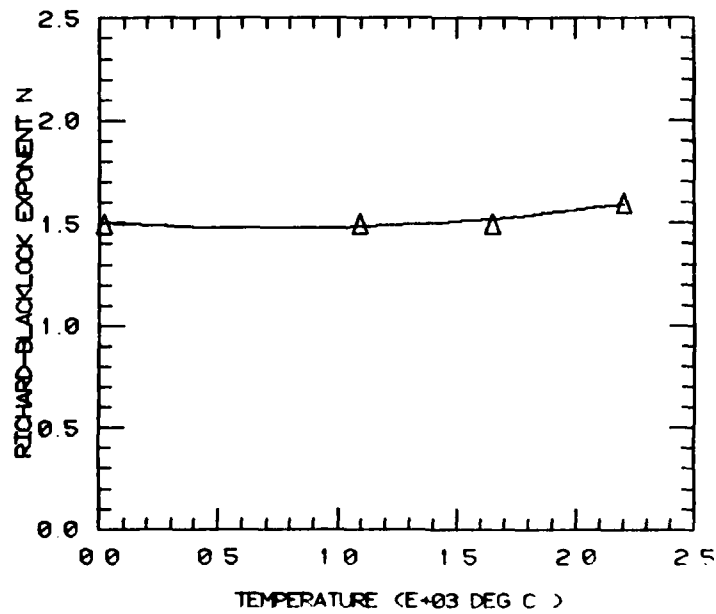


Figure 26. Richard-Blacklock Parameter n as a Function of Temperature for the Carbon Matrix.

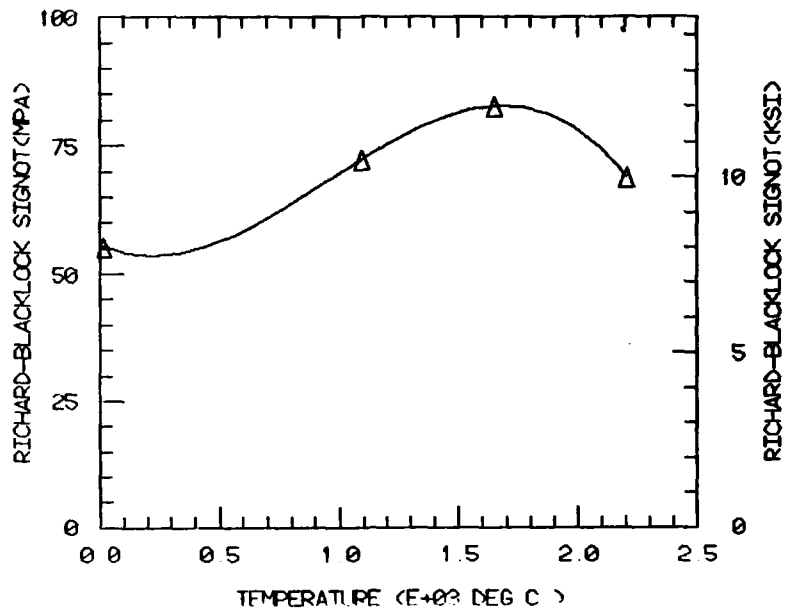


Figure 27. Richard-Blacklock Parameter σ_0 as a Function of Temperature for the Carbon Matrix.

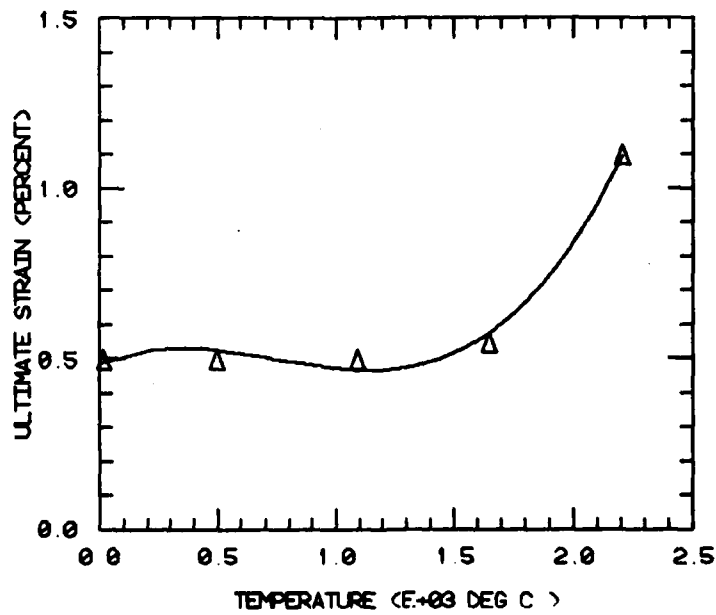


Figure 28. Ultimate Strain e^{ult} as a Function of Temperature for the Carbon Matrix.

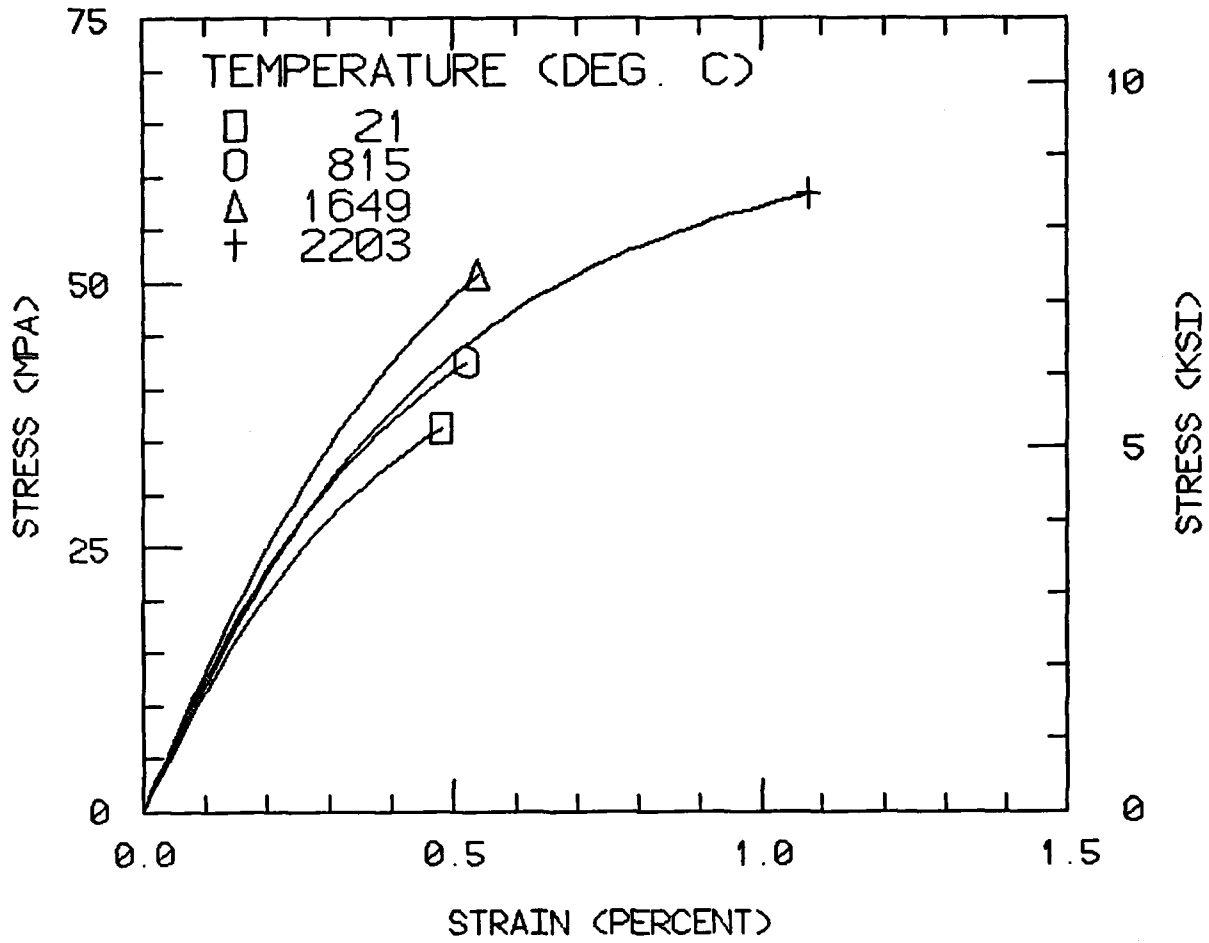


Figure 29. Richard-Blacklock Representation of Isotropic Carbon Tensile Stress-Strain Behavior at Various Temperatures.

TABLE 5

Strength Values for the Carbon Matrix,
Derived from ATJ-S Graphite Strengths

Temperature °C	Tensile Strength [67] (With-Grain)		Shear Strength [62] S_{us}	
	(MPa)	(ksi)	(GPa)	(ksi)
24	38.6	5.60	20.1	2.92
772	41.4	6.00		
815			17.8	2.58
1056	46.2	6.70		
1602	50.0	7.25		
1649			17.1	2.48
2136	63.7	9.24		
2204			21.7	3.15
2482			24.8	3.60

These values are plotted as functions of temperature in Figures 30 and 31 for the tensile and shear strengths respectively.

Material properties for matrix carbon were also described by sets of polynomial equations in temperature. The polynomial coefficients describing the carbon matrix material properties are listed in Table 6.

Properties of the oriented sheath material were assumed to be the same as the properties of the carbon fiber except that the sheath longitudinal strength was arbitrarily assumed to be one-half that of the fiber. The transverse sheath strength was assumed to be the same as the matrix carbon. These sheath properties, along with the carbon matrix and HM fiber properties were initially defined for use in the generalized plane strain micromechanics analysis to predict properties for unidirectional carbon-carbon fiber bundles.

4.2 Micromechanics Predicted Thermal Residual Stresses

Carbon-carbon materials experience temperature changes on the order of 2000 to 3000°C during fabrication and use. Modeling of the complete fabrication processing history was beyond the scope of the present research program. However, due to the large temperature changes that occur during fabrication, it was necessary to include the effects of thermally induced strains. Therefore, an attempt was made to model the temperature change experienced by the carbon-carbon material during cooldown from the final processing temperature.

An initial stress-free temperature of 2204°C was assumed. Temperature increments of -50°C were used in the initial micromechanics analysis of the isotropic carbon matrix model. This model, previously shown in Figure 6 of Section 3, contained no sheath material. The interface region was assumed to consist of isotropic carbon.

Model status plots at four temperatures during the incremental cooling are shown in Figure 32. At 2104°C, shown as Figure 32a, stresses in the matrix are such that elements in the region of closest fiber spacing are behaving inelastically. In Figure 32 these elements appear gray, marked with diagonal hatching. At 2004°C most of the matrix elements are inelastic, as shown in Figure 32b. At 1904°C, Figure 32c, all of the matrix is predicted to be inelastic by the micromechanics analysis. At 1754°C, matrix elements begin to fail, shown as black in Figure 32d. The first elements fail in the regions of closest fiber

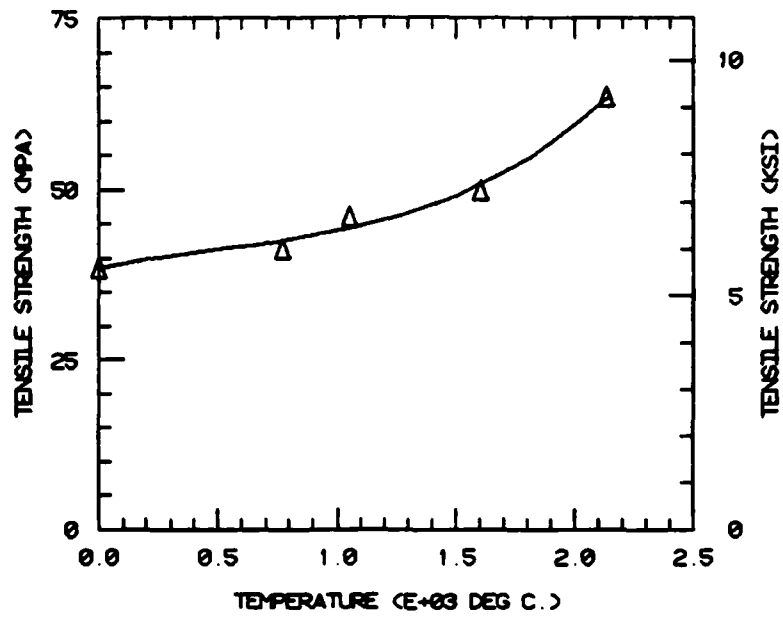


Figure 30. With-Grain Tensile Strength S^{ut} as a Function of Temperature for the Carbon Matrix.

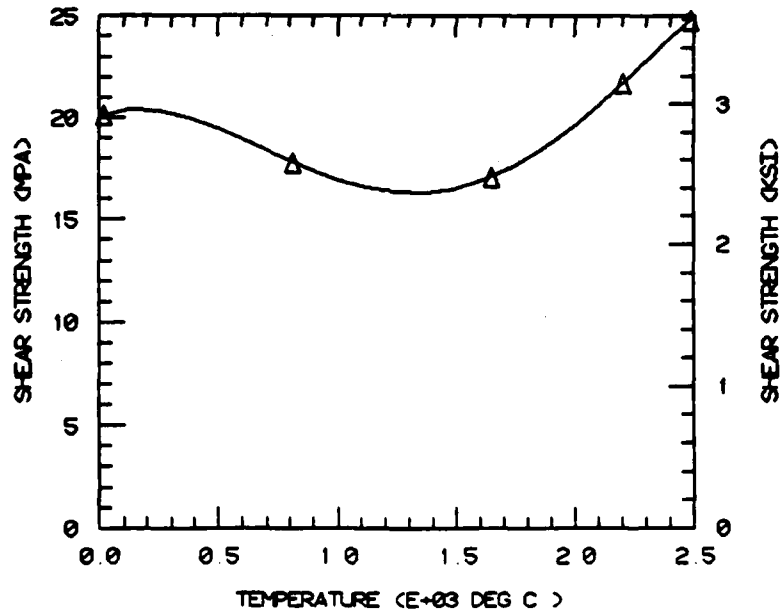


Figure 31. Shear Strength S^{us} as a Function of Temperature for the Carbon Matrix.

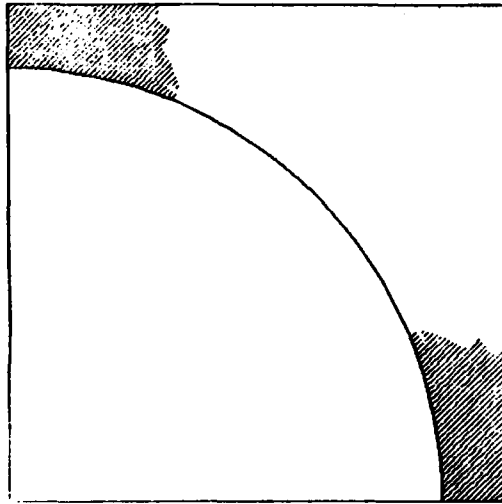
TABLE 6

Thermomechanical Properties of the Carbon Matrix
as Functions of Temperature ($^{\circ}\text{C}$)

$$\text{Property} = C_0 + C_1T + C_2T^2 + C_3T^3 + C_4T^4$$

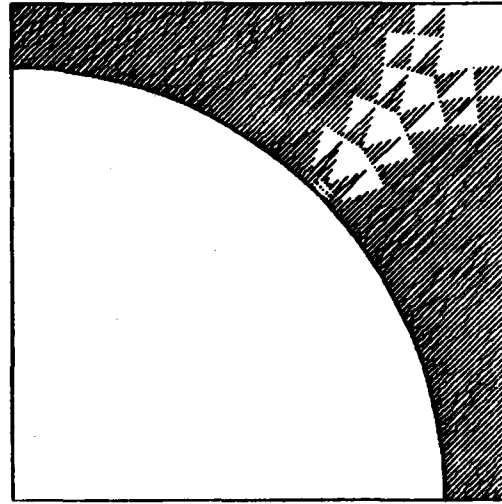
Property	C_0	C_1	C_2	C_3	C_4
E (psi)	1.33×10^6	-1.50×10^2	3.71×10^{-1}	-5.27×10^{-5}	-3.04×10^{-8}
ν	1.10×10^{-1}	1.30×10^{-5}	1.63×10^{-8}	-1.33×10^{-11}	3.18×10^{-15}
α ($^{\circ}\text{C}$) $^{-1}$	2.14×10^{-6}	3.83×10^{-9}	-2.60×10^{-12}	7.90×10^{-16}	-
E_R (psi)	1.75×10^6	2.38×10^2	8.60×10^{-2}	-8.30×10^{-5}	-
n	1.51×10^0	-1.54×10^{-4}	1.06×10^{-7}	-	-
σ_o (psi)	8.37×10^3	-3.22×10^0	8.45×10^{-3}	-3.02×10^{-6}	-
ϵ^t	4.88×10^{-3}	5.82×10^{-6}	-9.01×10^{-9}	3.46×10^{-12}	-
S^{ut} (psi)	5.58×10^3	1.09×10^0	-8.00×10^{-4}	5.07×10^{-7}	-
S^{us} (psi)	2.91×10^3	6.95×10^{-1}	-2.44×10^{-3}	1.55×10^{-6}	-

FINITE ELEMENT DISPLACEMENT GRID
 TEMP - 2104. DEG. C MODS - .00 N INCREMENT NO - 2 PLOT NO - 2
 SX1 - .00 KSI SY1 - .00 KSI SZ1 - .00 KSI SY2 - .00 KSI
 SX2 - .00 KSI
 ELASTIC ELEMENTS ARE WHITE PLASTIC ELEMENTS ARE GRAY
 FAILED ELEMENTS ARE BLACK



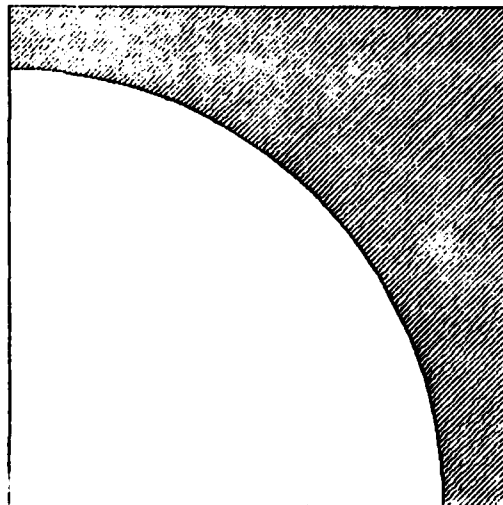
a) Temperature=2104°C

FINITE ELEMENT DISPLACEMENT GRID
 TEMP - 2004. DEG. C MODS - .00 N INCREMENT NO - 4 PLOT NO - 4
 SX1 - .00 KSI SY1 - .00 KSI SZ1 - .00 KSI SY2 - .00 KSI
 SX2 - .00 KSI
 ELASTIC ELEMENTS ARE WHITE PLASTIC ELEMENTS ARE GRAY
 FAILED ELEMENTS ARE BLACK



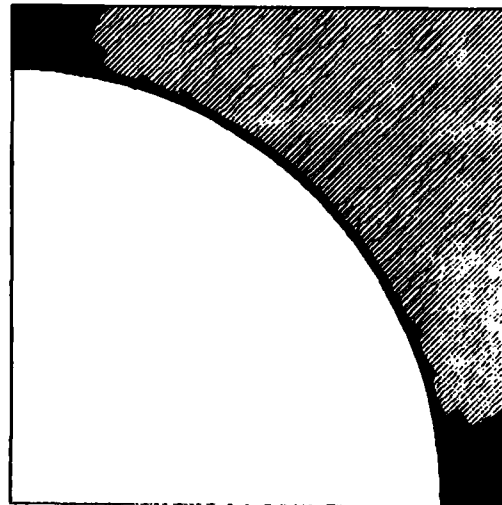
b) Temperature=2004°C

FINITE ELEMENT DISPLACEMENT GRID
 TEMP - 1904. DEG. C MODS - .00 N INCREMENT NO - 6 PLOT NO - 6
 SX1 - .00 KSI SY1 - .00 KSI SZ1 - .00 KSI SY2 - .00 KSI
 SX2 - .00 KSI
 ELASTIC ELEMENTS ARE WHITE PLASTIC ELEMENTS ARE GRAY
 FAILED ELEMENTS ARE BLACK



c) Temperature=1904°C

FINITE ELEMENT DISPLACEMENT GRID
 TEMP - 1754. DEG. C MODS - .00 N INCREMENT NO - 8 PLOT NO - 8
 SX1 - .00 KSI SY1 - .00 KSI SZ1 - .00 KSI SY2 - .00 KSI
 SX2 - .00 KSI
 ELASTIC ELEMENTS ARE WHITE PLASTIC ELEMENTS ARE GRAY
 FAILED ELEMENTS ARE BLACK



d) Temperature=1754°C

Figure 32. Crack Propagation in the Isotropic Carbon Matrix Model Due to Residual Thermal Stresses, $\alpha_{22}/\alpha_m = 3.0$.

spacing, at the lower right and upper left corners of Figure 32d. Failure in this specific analysis was defined by a maximum octahedral shear stress failure criterion. Subsequent redistribution of element stresses causes additional elements to fail, propagating two cracks within the matrix around the fiber-matrix interface region. The two cracks meet at the 45° diagonal, separating the model into two separate pieces. This defines total failure of the model as it is incapable of sustaining transverse tension or shear loading. Thus the model experienced an abrupt, catastrophic failure due to a temperature excursion of only -450°C.

This abrupt catastrophic failure of the matrix was caused by large thermally-induced stresses resulting from a large mismatch between the fiber transverse thermal expansion coefficient and the matrix thermal expansion coefficient. Referring to Figures 19 and 23 shown previously, it can be seen that the assumed transverse thermal expansion coefficient for the HM fiber was approximately three times the matrix thermal expansion coefficient at all temperatures. Temperature decreases in the model caused the fiber to shrink more rapidly in the radial direction than the matrix, inducing tensile stresses at the fiber-matrix interface. When these stresses exceeded the strength of the matrix carbon, failure occurred. As is shown in Figure 32, this failure takes place as cracks initiating and propagating at the fiber-matrix interface.

It is possible to extract intact fiber bundles from three-dimensionally woven carbon-carbon materials; they do have some residual strength at room temperature. Thus, there must be an inconsistency in the model as initially defined here.

Four possibilities are suggested. First, the model may actually be "stress-free" at a lower temperature than first assumed. Second, some stress relieving mechanism present in the actual material may not be included in the micromechanics model, e.g. viscoelastic behavior. Third, high stresses may indeed be present but the assumed constitutive strength values are too low, or the choice of failure criterion is incorrect. Finally, the assumed material properties, particularly the thermal expansion coefficient values, may be incorrect and the assumed mismatch is too large.

The "stress-free" temperature is an assumed initial state for any micromechanics analysis which includes processing-induced thermal stresses. Most linear elastic micromechanics analyses assume a stress-free temperature that is lower than the final processing temperature. These analyses assume that the thermally-induced strains caused by cooling from the final processing temperature to the "stress free" temperature produce no thermally-induced stress due to inelastic material behavior. Thus, these types of micromechanics analysis are actually assuming elastic-perfectly plastic material behavior. The value used as a "stress-free" temperature then becomes one of the selectable parameters of the analysis, to be chosen by "engineering judgment," i.e., by what works best.

The generalized plane strain finite element micromechanics analysis used in this present work is capable of modeling the actual stress-strain behavior of the constituent materials throughout the entire applicable temperature range. Therefore, use of the final processing temperature as a starting point for the analysis was appropriate. Selection of a lower initial temperature only resulted in calculation of lower estimates for fabrication-induced thermal residual stresses than might actually be present in the real material. If the present micromechanics model totally failed while cooling from 2204°C, then it also fails if cooled from any higher initial temperature.

In a second set of computer calculations, the initial (supposedly stress free) temperature was arbitrarily lowered by 50 percent to 1100°C. Even using this much lower initial temperature, cooling towards room temperature resulted in total failure of the model. Referring back to the constituent material properties plotted previously in Figures 11 through 14 and 20 through 24, it can be seen that both constituents retain significant stiffness even at 2204°C. Therefore, the composite could not be stress-free at 1100°C due only to inelastic deformations of the constituents. Referring to the work at MSC [13], it was found that thermal residual stresses were not modeled. These authors reasoned that carbon-carbon materials are essentially stress-free at room temperature, and therefore began their analysis at that point. The presence of cracks was included in their micromechanics model by use of degraded interfaces within the unit cell, as discussed in Section 2. Thus, the mismatch

between matrix and fiber transverse thermal expansion coefficients did not affect their micromechanics model because processing temperature excursions were not included.

It was apparent from this initial modeling attempt that a problem existed. If the modeled thermal expansion mismatch was correct, then the large induced stresses had to be relieved by some mechanism, or the micromechanics strength of matrix carbon had to be far greater than the strength of bulk ATJ-S graphite. Inelastic deformation alone did not provide sufficient stress relief for the model to survive an entire processing temperature excursion. The modeled stress-strain behavior of the matrix material, shown in Figure 29, was based on experimental data [62], which did exhibit some nonlinearity. However, ATJ-S is far from being an elastic-perfectly plastic material.

A second possible mechanism producing relief of fabrication-induced thermal stresses is viscoelastic behavior of the constituents. Viscoelastic behavior in carbon-carbon has been examined by Feldman [68,69] and by Quan, *et al.* [70]. These investigators found evidence that significant viscoelastic deformation (creep) occurred in graphite fibers at elevated temperatures, particularly above 2500°C. However, at lower temperatures, viscoelastic deformation was minimal. Thus, it is likely that time-dependent stress relaxation accounts for appreciable reduction of fabrication-induced thermal residual stresses only at highly elevated temperatures. However, if significant viscoelastic behavior takes place only at highly elevated temperatures, one method of modeling this effect is to again use a lower "stress-free" initial temperature. Stresses are then assumed to be relieved by time-dependent material behavior at temperatures above this stress-free temperature. As was already discussed, however, an assumed initial "stress free" temperature as low as 1100°C still resulted in total failure of the micromechanics model during cooling. It is unlikely that significant short term viscoelastic behavior takes place in carbon-carbon at temperatures below 1100°C.

A third possibility to account for the discrepancy between modeled and real carbon-carbon material behavior is an inaccuracy in the assumed matrix strengths, coupled with a poor choice of failure criterion. The isotropic carbon matrix strength values used in the present analysis are

plotted in Figures 30 and 31. These plotted values actually tend to be optimistic for ATJ-S graphite as they represent across-grain strengths rather than the averaged across- and with-grain strengths as used in Reference [13]. However, one may argue that these are strengths of "bulk" carbon and do not accurately reflect the potential constituent matrix material strength at the micromechanics scale.

It is useful at this point to examine the stress state within the isotropic carbon matrix prior to the onset of failure. Figure 33 presents eight quantities plotted for the isotropic carbon matrix region around an individual HM carbon fiber. The quantities plotted in Figure 33 are for a state of stress existing in the matrix after the unidirectional carbon-carbon composite has been cooled from 2204°C to 1804°C. A total of eight increments of -50°C have been applied, representing a total temperature change of -400°C. Constituent material properties were adjusted at the beginning of each increment to include variations in constituent material properties with temperature. Only temperature increments have been applied at this point, no external, mechanically-induced stresses are present. Contour lines shown in Figure 33 are as output by the micromechanics analysis and have not been smoothed for presentation.

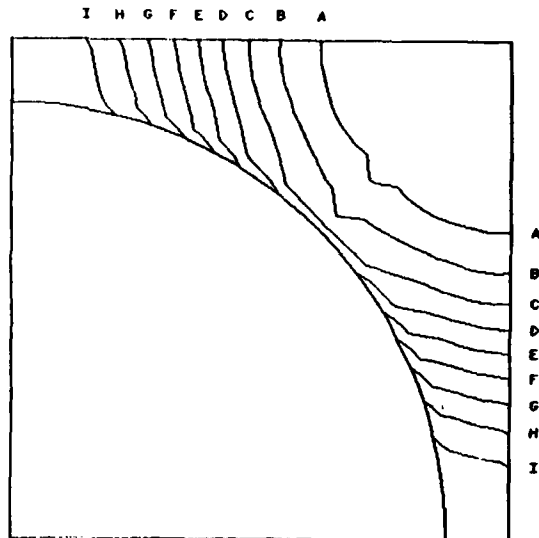
Figure 33a is a contour plot of the octahedral shear stress distribution in the matrix. Contour lines have not been plotted for the fiber although they are available from the analysis. As can be seen in Figure 33a, the stress distribution is symmetrical about the 45° diagonal as would be expected from the assumption of a square fiber packing array. The octahedral shear stress is greatest in the region of closet fiber spacings, i.e., along the horizontal and vertical axes. There the octahedral shear stress is 25.7 MPa (3.73 ksi), which is very near the 25.8 MPa (3.74 ksi) assumed octahedral shear strength of the matrix at 1804°C. A key to the contour labels, giving stress values, is printed above each plot in Figure 33. Along the 45° diagonal, the direction of greatest fiber spacing, the stress is lowest. The octahedral shear stress is of special interest as this is the criterion for yield in this elastoplastic micromechanics analysis formulation. Maximum octahedral shear stress (distortional energy) is also one

OCTAHEDRAL SHEAR STRESS CONTOURS

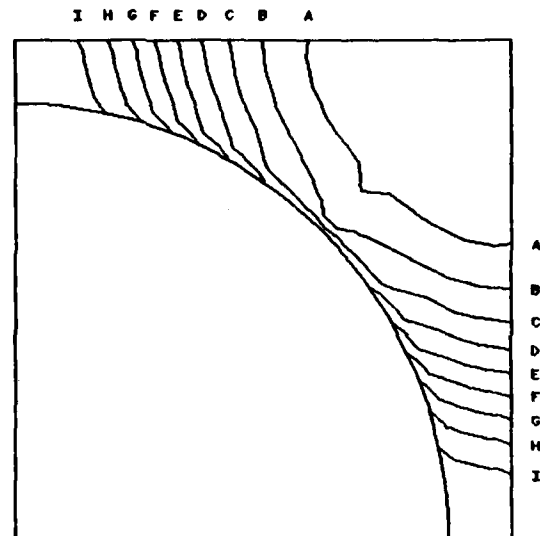
TEMP - 1804 DEG C	INCRS - .00 N	INCREMENT NO - 8	PLOT NO - 21
SX1 - .00 KSI	SY1 - .00 KSI	SZ1 - .00 KSI	SYZ - .00 KSI
SX2 - .00 KSI	MIN - 1.73 KSI	MAX - 3.73 KSI	A - 1.00 KSI
B - 2.13 KSI	C - 2.39 KSI	D - 2.63 KSI	E - 2.73 KSI
F - 2.99 KSI	G - 3.13 KSI	H - 3.33 KSI	I - 3.53 KSI

OCTAHEDRAL SHEAR STRAIN CONTOURS X1000

TEMP - 1804 DEG C	INCRS - .00 N	INCREMENT NO - 8	PLOT NO - 22
SX1 - .00 KSI	SY1 - .00 KSI	SZ1 - .00 KSI	SYZ - .00 KSI
SX2 - .00 KSI	MIN - 2.74	MAX - 6.30	A - 3.30
B - 3.97	C - 4.49	D - 5.09	E - 5.66
F - 6.19	G - 6.69	H - 7.26	I - 7.82



a) Octahedral Shear Stress



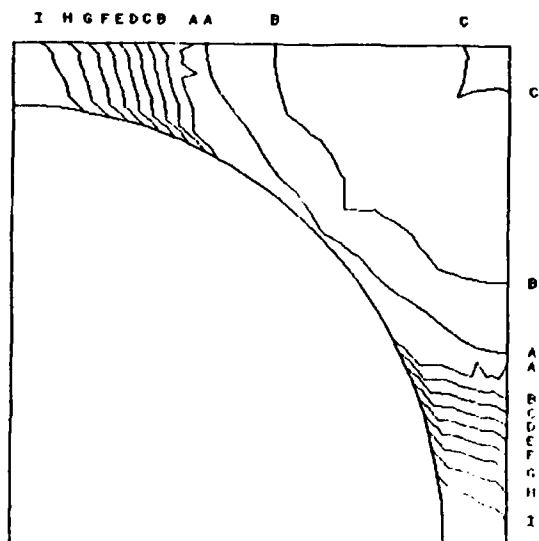
b) Octahedral Shear Strain

FIRST PRINCIPAL STRESS CONTOURS

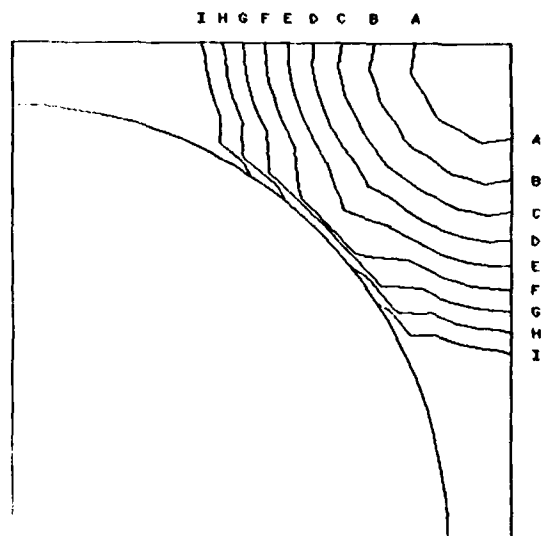
TEMP - 1804 DEG C	INCRS - .00 N	INCREMENT NO - 8	PLOT NO - 17
SX1 - .00 KSI	SY1 - .00 KSI	SZ1 - .00 KSI	SYZ - .00 KSI
SX2 - .00 KSI	MIN - .93 KSI	MAX - 2.74 KSI	A - 1.11 KSI
B - 1.29 KSI	C - 1.47 KSI	D - 1.66 KSI	E - 1.83 KSI
F - 2.01 KSI	G - 2.19 KSI	H - 2.37 KSI	I - 2.60 KSI

SECOND PRINCIPAL STRESS CONTOURS

TEMP - 1804 DEG C	INCRS - .00 N	INCREMENT NO - 8	PLOT NO - 18
SX1 - .00 KSI	SY1 - .00 KSI	SZ1 - .00 KSI	SYZ - .00 KSI
SX2 - .00 KSI	MIN - -2.18 KSI	MAX - 1.62 KSI	A - -1.66 KSI
B - -1.64 KSI	C - -1.22 KSI	D - -.80 KSI	E - -.59 KSI
F - -.26 KSI	G - .66 KSI	H - .38 KSI	I - .70 KSI



c) Maximum Principal Stress



d) Intermediate Principal Stress

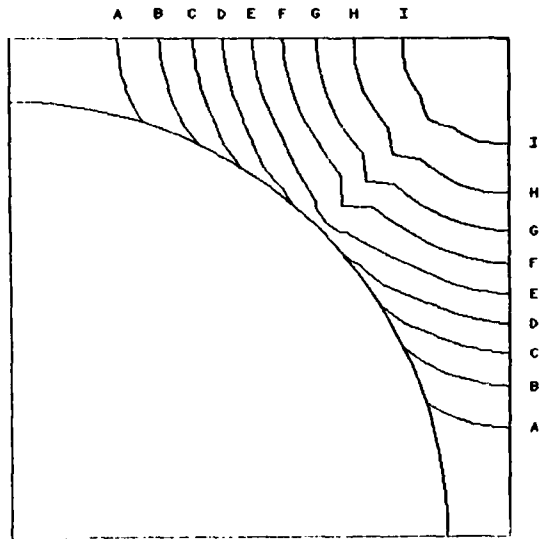
Figure 33. Stress-Strain State of the Isotropic Carbon Matrix Model at 1804°C, Maximum Octahedral Shear Stress Failure Criterion, Thermal Loading.

THIRD PRINCIPAL STRESS CONTOURS

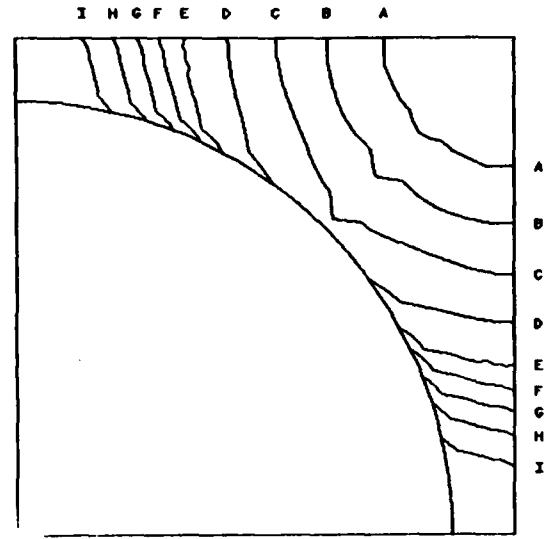
TEMP - 1804 DEG. C	MOIS - .00 X	INCREMENT NO - 0	PLOT NO - 19
SIX - .00 KSI	SYX - .00 KSI	SZZ - .00 KSI	SYZ - .00 KSI
SXZ - .00 KSI	MIN - -6.66 KSI	MAX - -2.21 KSI	A - -5.66 KSI
B - -3.23 KSI	C - -4.91 KSI	D - -4.52 KSI	E - -4.14 KSI
F - -3.75 KSI	G - -3.37 KSI	H - -2.60 KSI	I - -2.60 KSI

MAXIMUM SHEAR STRESS CONTOURS

TEMP - 1804 DEG. C	MOIS - .00 X	INCREMENT NO - 0	PLOT NO - 20
SIX - .00 KSI	SYX - .00 KSI	SZZ - .00 KSI	SYZ - .00 KSI
SXZ - .00 KSI	MIN - 1.65 KSI	MAX - 4.35 KSI	A - 2.10 KSI
B - 2.35 KSI	C - 2.60 KSI	D - 2.65 KSI	E - 3.10 KSI
F - 3.35 KSI	G - 3.60 KSI	H - 3.65 KSI	I - 4.10 KSI



e) Minimum Principal Stress



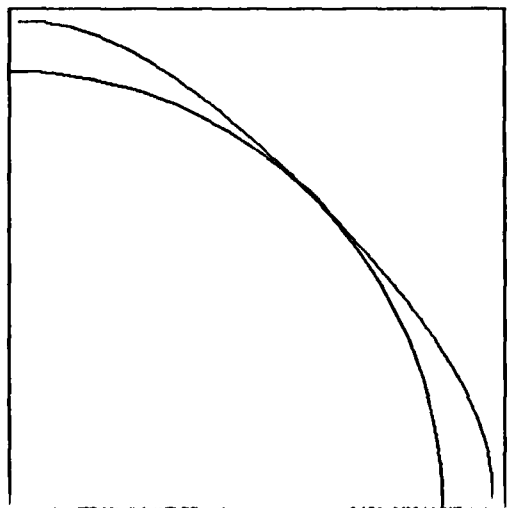
f) Maximum Shear Stress

INTERFACE NORMAL STRESSES

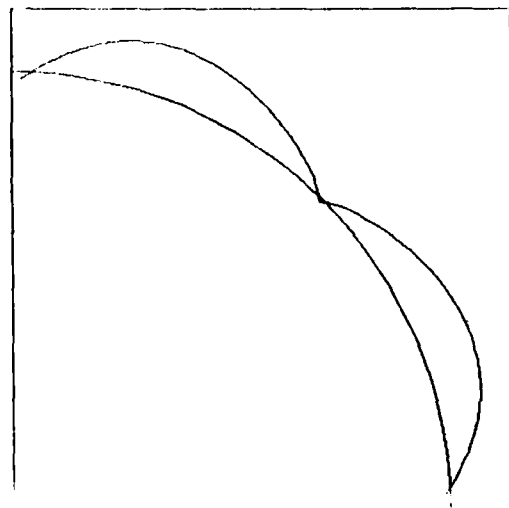
TEMP - 1804 DEG. C	MOIS - .00 X	INCREMENT NO - 0	PLOT NO - 23
SIX - .00 KSI	SYX - .00 KSI	SZZ - .00 KSI	SYZ - .00 KSI
SXZ - .00 KSI	MIN - -2.72 KSI	MAX - 2.72 KSI	

INTERFACE SHEAR STRESSES

TEMP - 1804 DEG. C	MOIS - .00 X	INCREMENT NO - 0	PLOT NO - 24
SIX - .00 KSI	SYX - .00 KSI	SZZ - .00 KSI	SYZ - .00 KSI
SXZ - .00 KSI	MIN - -1.61 KSI	MAX - 1.61 KSI	



g) Interface Normal Stress



h) Interface Normal Stress

Figure 33 (continued). HM/Isotropic Carbon-Carbon Unidirectional Composite, 1804°C, No Mechanical Loading.

possible failure criterion, and was used to define matrix failure in the results of Figure 33.

Figure 33b is a contour plot of the octahedral shear strain. These contours follow trends similar to the octahedral shear stresses plotted in Figure 33a. However, the relationship between octahedral shear stress and octahedral shear strain is not linear.

The maximum (most positive), intermediate, and minimum (most negative) principal stresses are plotted in Figures 33c, 33d, and 33e, respectively. Since a temperature change alone will not induce longitudinal shear, the maximum and minimum principal stresses are in the plane of the plot and the intermediate principal stress is perpendicular to the plane of the plot. In general this is not true if longitudinal shear stress is present. The largest principal stresses again tend to occur in regions of closest fiber spacing. The maximum tensile principal stress, shown in Figure 33c, is 18.9 MPa (2.74 ksi), well below the 54.7 Mpa (7.93 ksi) assumed normal tensile strength at 1804°C.

Maximum shear stress contours are plotted in Figure 33f. Again due to the absence of longitudinal shear stress in this loading case, the maximum shear stresses plotted in Figure 33f occur in the plane of the plot. The maximum shear stress present is 30.0 MPa (4.35 ksi), again located in the region of closest fiber spacing. It will be noted that this value is greater than the assumed matrix shear strength at 1804°C, as plotted in Figure 31. However, as the octahedral shear strengths are derived from tensile data, and a maximum shear stress failure criterion is not being used, no element failures occur. Otherwise, cracking would have taken place prior to this state in the thermal cooldown during final processing of this carbon-carbon fiber bundle.

Frequently it is the normal or shear stress at the fiber-matrix interface which reaches a critical value first, and initiates failure of the composite. Figure 33g is a plot of the thermally-induced normal stress distribution around the fiber-matrix interface. Values plotted outside the interface indicate tensile normal stress (as is the case for all values plotted in Figure 33g). Values plotted inside the interface would indicate negative interface normal stresses. As can be seen in Figure 33c, the interface is subjected to tensile stress everywhere

because the fiber transverse thermal expansion coefficient is greater than that of the matrix. Thus on cooling, the fiber tends to pull away from the matrix. The normal stress distribution is not uniform around the interface, again due to the assumed packing array. The maximum tensile normal stress at the interface is 18.8 MPa (2.72 ksi), in the region of closest fiber spacing.

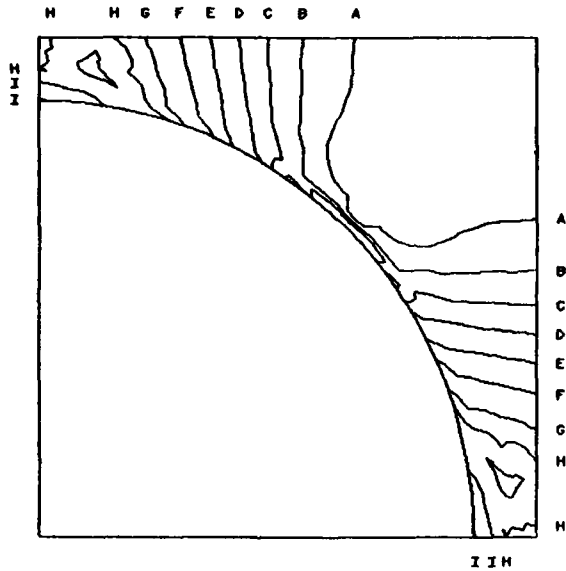
The interface shear stress distribution is shown in Figure 33h. The interface shear stress is near zero at the horizontal, vertical and 45° diagonal axes of symmetry. A sign change (change in shear stress direction) is not reflected in the plot since interface shear stresses do not generally lie in the plane of the plot (due to the presence of longitudinal shear stress). The maximum shear stress along the fiber matrix interface is 11.1 MPa (1.61 ksi).

As indicated in the plots of Figure 33, the matrix stresses are quite high relative to the matrix strengths after a temperature excursion of only 40°C. This temperature change is small relative to the total temperature change experienced by the material during cooling from the final fabrication temperature. An octahedral shear stress failure criterion was used to predict the cracking of Figure 33 where the composite failed at 1754°C. As is shown in Figure 33, the maximum normal stress present in the matrix is less than the assumed ultimate tensile strength of 54.7 MPa (7.93 ksi) at 1804°C. For brittle materials, a maximum normal stress criterion may be a more appropriate choice of failure criterion. In a second computer simulation, the thermal cooldown was again modeled, beginning at 2204°C and cooling in increments of -50°C. For this second modeling of the isotropic carbon matrix finite element mesh, a maximum normal stress failure criterion was selected. For this thermal cooling case, all results prior to first element failure were exactly the same as for the first thermal cooling case as only the matrix failure criterion was different. Crack initiation and total failure of the model took place at 804°C after a total temperature change of 1400°C. The crack propagation pattern was the same as that plotted for the maximum octahedral shear stress failure criterion case in Figure 32.

The stress state in the model at 854°C, just prior to the increment in which failure occurs, is shown in Figure 34. As in Figure 33, all

OCTAHEDRAL SHEAR STRESS CONTOURS

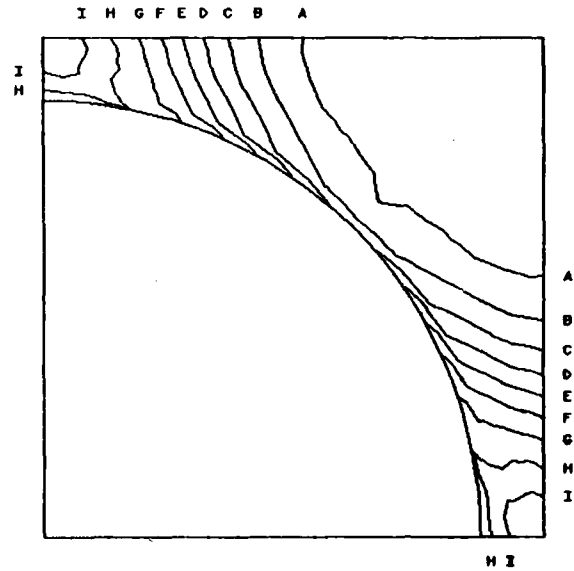
TEMP - 854 DEG. C	MOIS - .00 %	INCREMENT NO. - 27	PLOT NO. - 25
SIX - .00 KSI	SIY - .00 KSI	SZZ - .00 KSI	SVZ - .00 KSI
SHZ - .00 KSI	MIN - 3.16 KSI	MAX - 5.45 KSI	A - 3.41 KSI
B - 3.64 KSI	C - 3.86 KSI	D - 4.00 KSI	E - 4.31 KSI
F - 4.64 KSI	G - 4.77 KSI	H - 4.90 KSI	I - 5.22 KSI



a) Octahedral Shear Stress

OCTAHEDRAL SHEAR STRAIN CONTOURS K1000

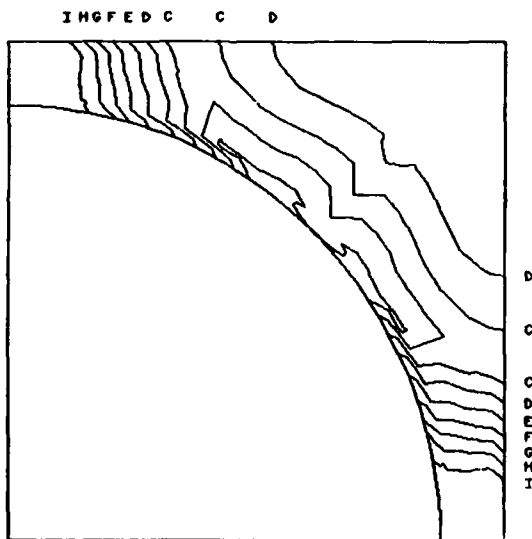
TEMP - 854 DEG. C	MOIS - .00 %	INCREMENT NO. - 27	PLOT NO. - 26
SIX - .00 KSI	SIY - .00 KSI	SZZ - .00 KSI	SVZ - .00 KSI
SHZ - .00 KSI	MIN - 7.95	MAX - 30.30	A - 10.20
B - 12.44	C - 14.68	D - 16.93	E - 19.17
F - 21.42	G - 23.66	H - 25.91	I - 28.15



b) Octahedral Shear Strain

FIRST PRINCIPAL STRESS CONTOURS

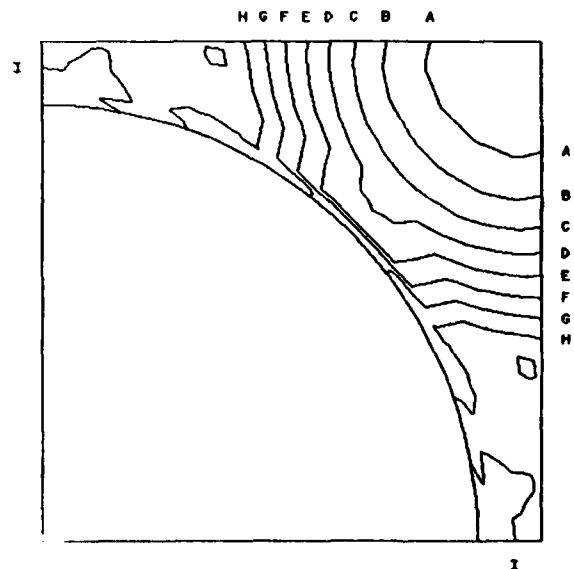
TEMP - 854 DEG. C	MOIS - .00 %	INCREMENT NO. - 27	PLOT NO. - 21
SIX - .00 KSI	SIY - .00 KSI	SZZ - .00 KSI	SVZ - .00 KSI
SHZ - .00 KSI	MIN - .40 KSI	MAX - 5.00 KSI	A - .00 KSI
B - 1.40 KSI	C - 1.00 KSI	D - 2.40 KSI	E - 2.00 KSI
F - 3.00 KSI	G - 4.00 KSI	H - 4.00 KSI	I - 5.00 KSI



c) Maximum Principal Stress

SECOND PRINCIPAL STRESS CONTOURS

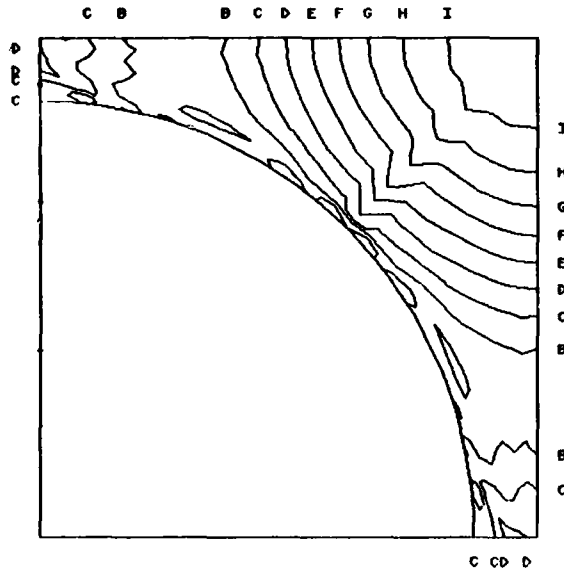
TEMP - 854 DEG. C	MOIS - .00 %	INCREMENT NO. - 27	PLOT NO. - 22
SIX - .00 KSI	SIY - .00 KSI	SZZ - .00 KSI	SVZ - .00 KSI
SHZ - .00 KSI	MIN - -4.67 KSI	MAX - 2.00 KSI	A - -3.46 KSI
B - -2.66 KSI	C - -2.25 KSI	D - -1.64 KSI	E - -1.03 KSI
F - -43 KSI	G - .18 KSI	H - .79 KSI	I - 1.40 KSI



d) Intermediate Principal Stress

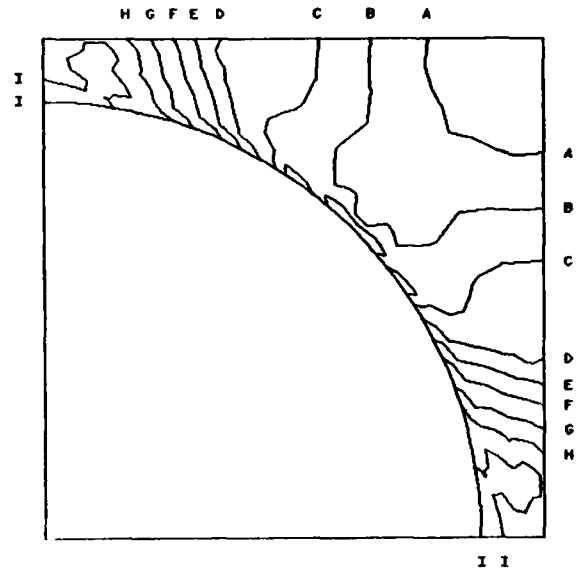
Figure 34. Stress-Strain State of the Isotropic Carbon Matrix Model at 854°C, Maximum Normal Stress Failure Criterion, Thermal Loading.

THIRD PRINCIPAL STRESS CONTOURS
 TEMP - 854. DEG C MZIS - .00 N INCREMENT NO - 27 PLOT NO. - 23
 SXX - .00 KSI SYY - .00 KSI SZZ - .00 KSI SYZ - .00 KSI
 SXY - .00 KSI SMN - -8.29 KSI MAX - -4.11 KSI A - -7.00 KSI
 B - -7.46 KSI C - -7.04 KSI D - -6.62 KSI E - -6.20 KSI
 F - -5.78 KSI G - -5.37 KSI H - -4.95 KSI I - -4.53 KSI



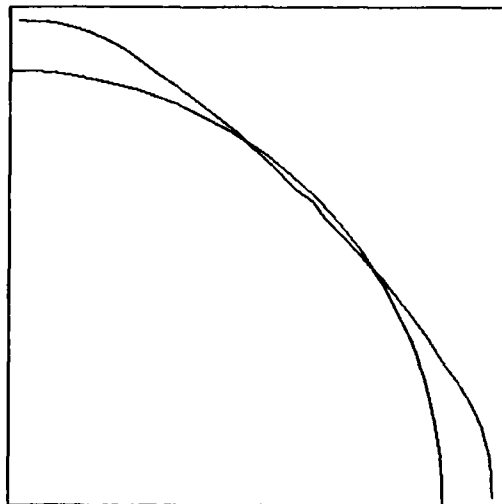
e) Minimum Principal Stress

MAXIMUM SHEAR STRESS CONTOURS
 TEMP - 854 DEG C MZIS - .00 N INCREMENT NO - 27 PLOT NO - 24
 SXX - .00 KSI SYY - .00 KSI SZZ - .00 KSI SYZ - .00 KSI
 SXY - .00 KSI SMN - 3.48 KSI MAX - 6.43 KSI A - 3.78 KSI
 B - 4.07 KSI C - 4.37 KSI D - 4.66 KSI E - 4.95 KSI
 F - 5.25 KSI G - 5.55 KSI H - 5.84 KSI I - 6.14 KSI



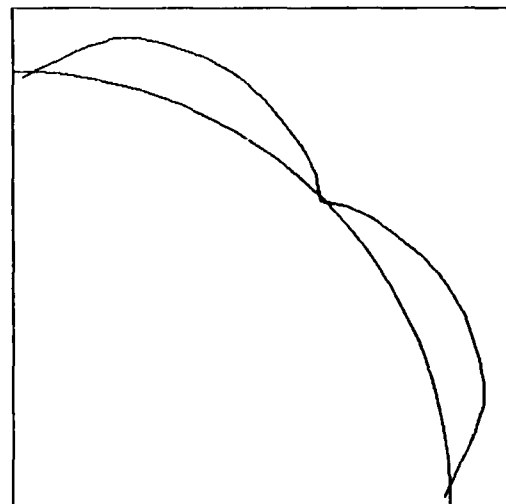
f) Maximum Shear Stress

INTERFACE NORMAL STRESSES
 TEMP - 854. DEG C MZIS - .00 N INCREMENT NO - 27 PLOT NO. - 27
 SXX - .00 KSI SYY - .00 KSI SZZ - .00 KSI SYZ - .00 KSI
 SXY - .00 KSI SMN - -5.22 KSI MAX - 5.22 KSI



g) Interface Normal Stress

INTERFACE SHEAR STRESSES
 TEMP - 854 DEG C MZIS - .00 N INCREMENT NO - 27 PLOT NO. - 28
 SXX - .00 KSI SYY - .00 KSI SZZ - .00 KSI SYZ - .00 KSI
 SXY - .00 KSI SMN - -3.62 KSI MAX - 3.62 KSI



h) Interface Shear Stress

Figure 34 (continued). Stress-Strain State of the Isotropic Carbon Matrix Model at 854°C, Maximum Normal Stress Failure Criterion, Thermal Loading.

eight available sets of information are plotted in Figure 34. In particular, note the octahedral shear stress contour values plotted in Figure 34a. The maximum octahedral shear stress is 37.6 MPa (5.45 ksi), well above the assumed octahedral shear ultimate strength of 20.3 MPa (2.95 ksi) at 854°C. However, as the maximum normal stress failure criterion was used rather than the octahedral shear failure criterion, no failures took place. The maximum normal stress contours, plotted in Figure 34c, indicate a maximum normal stress of 37.9 MPa (5.50 ksi), again located in the region of closest fiber spacing. This stress is approximately 90 percent of the matrix tensile strength at 804°C. Thus, during the next cooling increment, matrix elements began to fail. As in the previous thermal cooling case, stress redistribution following failure of an element caused additional elements to fail. This resulted in cracks propagating along the fiber-matrix interface, leading to total failure of the model.

Although use of the two different failure criteria resulted in total model failure at two different temperatures, the net result was that the modeled carbon-carbon unidirectional fiber bundle did not survive thermally-induced residual processing stresses using the assumed constituent material properties. Thus, if these indicated high thermal residual stresses were actually present in the fiber bundles, the assumed strength allowables had to be too low. Unfortunately, no data in the literature supported using larger strength allowables, based on examinations of test data for ATJ-S graphite and other carbons [61,62,67,71,72].

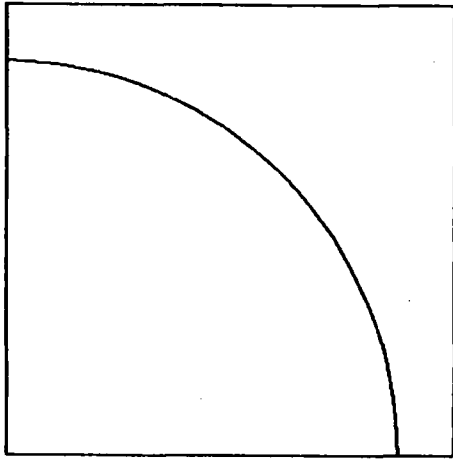
Unidirectional carbon-carbon fiber bundles can be fabricated and cooled to room temperature. If inelastic or viscoelastic material behavior does not relieve the thermally-induced residual stresses, then the assumed mismatch in thermal expansion coefficients between fiber and matrix must be too large. Matrix thermal expansion data taken from Reference [13] were derived from measurements reported in Reference [62] for ATJ-S graphite. These data and the corresponding thermal expansion coefficient were plotted versus temperature in Figures 22 and 23. As was stated previously in this present report, assumed fiber transverse thermal expansion coefficient data also showed fair agreement with very limited experimental radial thermal strain measurements [13,60].

However, fiber transverse thermal expansion coefficients are not easily measured over the temperature ranges used in this analysis. The values used in Reference [13] and in this analysis for fiber transverse thermal expansion coefficient were educated guesses. Therefore there is considerable room for adjustment.

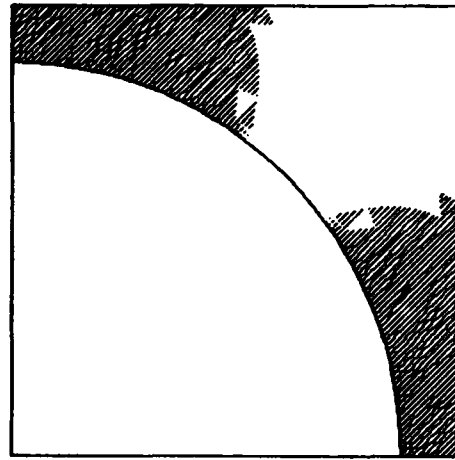
The thermal expansion mismatch ratio α_{22}/α_m between the transverse fiber thermal expansion coefficient and the isotropic carbon matrix thermal expansion coefficient as plotted in Figures 19 and 23 is approximately three. Parametric variations of this mismatch ratio showed that the isotropic carbon matrix model could survive the fabrication temperature excursion if the ratio was reduced to approximately two. This was done by arbitrarily reducing the transverse fiber thermal expansion coefficient. The matrix thermal expansion coefficient could also have been increased or both values could have been changed.

Model status plots for a simulated cooling of the isotropic carbon matrix model are shown in Figure 35. A stress free temperature of 2204°C was again assumed. Cooling increments of -50°C were also used. At 2154°C all matrix elements are still within the elastic range, as shown in Figure 35a. At 1954°C many of the matrix elements are predicted to be inelastic, as noted by the shaded regions. At 1854°C, Figure 35c, all matrix elements are inelastic. The first element failures, marked by black in Figure 35d, occur at 104°C. Elements in the highly stressed regions of closest fiber spacing fail and cracks begin to propagate around the fiber-matrix interface. No further cracking occurs in the final two temperature increments during cooling to room temperature.

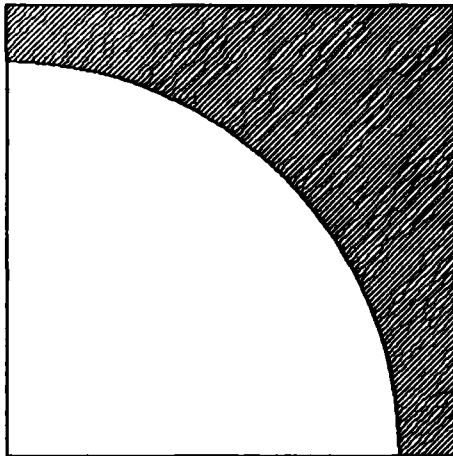
The model was, at this point, providing answers which corresponded to real world unidirectional carbon-carbon composite material behavior in that the model has survived the fabrication temperature excursion. These materials experience microcracking during fabrication, but obviously they can be fabricated. Thermal residual stresses are induced during fabrication of real carbon-carbon materials and may be quite high. These stresses are relieved by a combination of inelastic material deformation and microcracking. In order to complete the micromechanics analysis of carbon-carbon fiber bundles material behavior, all further computations were performed using a reduced α_{22}/α_m thermal expansion coefficient mismatch ratio, i.e., a ratio of two. Mechanical loads were



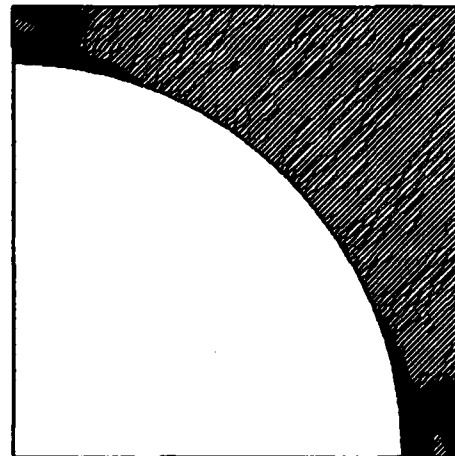
a) Temperature=2154°C



b) Temperature=1954°C



c) Temperature=1854°C



d) Temperature=104°C

Figure 35. Crack Propagation in the Isotropic Carbon Matrix Model Due to Residual Thermal Stresses, $\alpha_{22}/\alpha_m \approx 2$.

then applied in order to predict the thermomechanical response of the carbon-carbon fiber bundles.

4.3 Isotropic Carbon Matrix Micromechanics Model Results

The purpose of this micromechanics analysis was to provide estimates of carbon-carbon fiber bundle stress-strain behavior for use in the three-dimensional minimechanics model. As discussed in Section 3, four types of loading were separately applied to the micromechanics model following completion of the cooldown temperature excursion. These loadings simulated longitudinal tension, transverse tension, longitudinal shear, and transverse shear stresses. The same mechanical loads were simulated at other temperatures by first applying temperature increments to reheat the model prior to application of mechanical loading increments. Mechanical stress-strain behavior of the carbon-carbon fiber bundles was modeled in this present work for three temperatures, viz, room temperature, 815°C, and 1649°C. In all cases, simulated loading increments were applied to the models to achieve ultimate failure.

Longitudinal tension stress-strain curves are plotted for the isotropic carbon matrix model in Figure 36. All three stress-strain plots are linear. The room temperature plot, marked with squares, indicates an elastic tensile modulus of 218 GPa (31.6 Msi). The plotted symbols mark actual stress-strain values as calculated by the micromechanics computer program for each increment of mechanical loading. At 815°C the calculated tensile modulus is 225 GPa (32.7 Msi) for the plot marked with circles in Figure 36. This modulus is slightly greater than the estimated room temperature tensile modulus, reflecting the assumed increase in fiber tensile modulus with increasing temperature, previously shown in Figure 11. As the composite longitudinal tensile modulus is a fiber dominated property, it is to be expected that it will vary with temperature in the same manner as the input constituent fiber tensile modulus. The third stress-strain plot at 1649°C, marked with triangles in Figure 36, indicates a tensile modulus of 198 GPa (28.7 Msi), again following a trend with temperature similar to the fiber tensile modulus.

The micromechanics predictions of cracking patterns reflect the known conclusion that longitudinal tensile behavior is fiber-dominated.

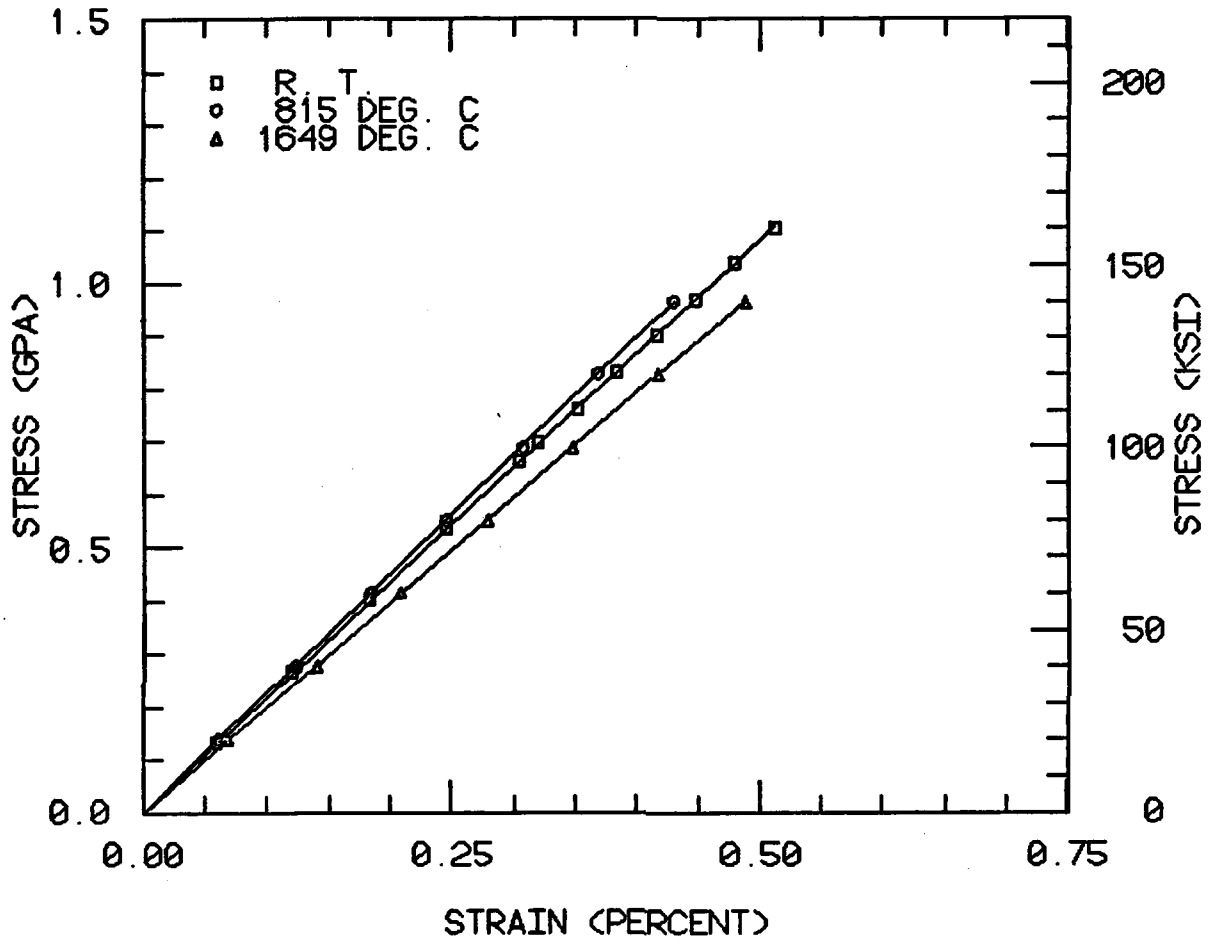


Figure 36. Longitudinal Tension Stress-Strain Response for the Isotropic Carbon Matrix Model.

Four model status plots are shown in Figure 37, for four levels of applied longitudinal tension. Figure 37a shows the model after application of the first longitudinal tension loading increment. The cracking pattern at the end of the thermal cooldown was plotted in the previously discussed Figure 35.

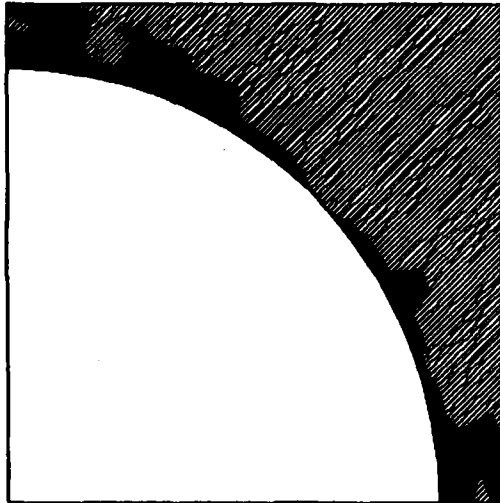
At an applied stress of 263 MPa (38.2 ksi), additional cracking takes place at the fiber-matrix interface as shown in Figure 37a. At 400 MPa (58.0 ksi) substantial cracking occurs, as shown in Figure 37b. When the applied tensile stress reaches approximately 689 MPa (100 ksi), Figure 37c, the matrix has failed and does not contribute to the model longitudinal stiffness. At 1.11 GPa (161 ksi) the fiber and thus the entire model catastrophically fails. As discussed earlier in Section 3, the fiber failure criterion used in this analysis was a maximum longitudinal tensile stress failure criterion. A statistics-based criterion was not used, but could be added to the computer program.

Crack pattern plots for the 815°C and 1649°C longitudinal tension simulations were very similar to those shown in Figure 37 for room temperature loading. Therefore these plots have not been included in this report.

Predicted transverse tension stress-strain response of the isotropic carbon matrix fiber bundle model is shown in Figure 38. The transverse tension stress-strain behavior of the modeled fiber bundle is definitely nonlinear. At room temperature, the initial transverse tensile modulus is 5.30 GPa (0.77 Msi). This transverse modulus is approximately the same at 815°C, 5.2 GPa (0.76 Msi) and increases slightly to 6 GPa (0.88 ksi) at 1649°C.

The nonlinear appearance of these plots is due in part to nonlinear constituent matrix stress-strain behavior. Transverse properties of unidirectional composites are more influenced by the matrix than are the composite longitudinal properties. However, a substantial portion of the nonlinear stress-strain behavior shown in Figure 38 is due to further cracking of the matrix. Four model status plots for room temperature transverse loading are shown in Figure 39. Transverse tension loading causes further matrix cracking during the first loading increment, as illustrated in Figure 39a at a stress level of 4.6 MPa (0.66 ksi). Thus, additional permanent damage, producing nonlinear stress-strain behavior,

FINITE ELEMENT DISPLACEMENT GRID
 TEMP - 21. DEG. C MOD - .00 N INCREMENT NO. - 2 PLOT NO. - 2
 SX - .00 KSI SY - .00 KSI SZ - 39.16 KSI SZ - .00 KSI
 ELASTIC ELEMENTS ARE WHITE PLASTIC ELEMENTS ARE GRAY
 FAILED ELEMENTS ARE BLACK



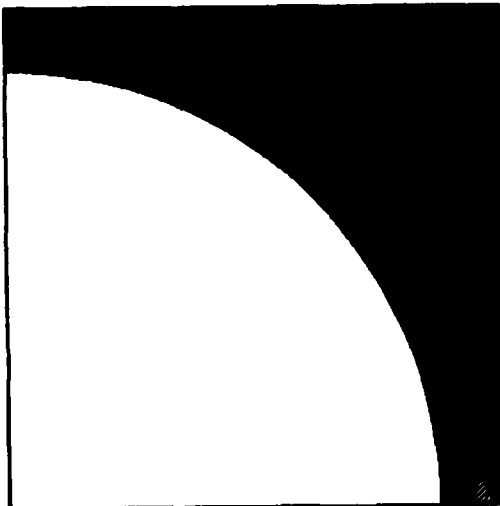
a) Stress = 263 MPa (38.2 ksi)

FINITE ELEMENT DISPLACEMENT GRID
 TEMP - 21. DEG. C MOD - .00 N INCREMENT NO. - 3 PLOT NO. - 3
 SX - .00 KSI SY - .00 KSI SZ - 99.04 KSI SZ - .00 KSI
 ELASTIC ELEMENTS ARE WHITE PLASTIC ELEMENTS ARE GRAY
 FAILED ELEMENTS ARE BLACK



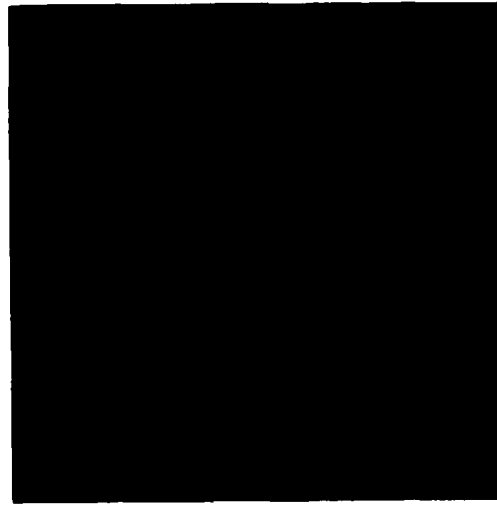
b) Stress = 400 MPa (58.0 ksi)

FINITE ELEMENT DISPLACEMENT GRID
 TEMP - 21. DEG. C MOD - .00 N INCREMENT NO. - 6 PLOT NO. - 6
 SX - .00 KSI SY - .00 KSI SZ - 100.76 KSI SZ - .00 KSI
 ELASTIC ELEMENTS ARE WHITE PLASTIC ELEMENTS ARE GRAY
 FAILED ELEMENTS ARE BLACK



c) Stress = 689 MPa (100.1 ksi)

FINITE ELEMENT DISPLACEMENT GRID
 TEMP - 21. DEG. C MOD - .00 N INCREMENT NO. - 10 PLOT NO. - 10
 SX - .00 KSI SY - .00 KSI SZ - 100.00 KSI SZ - .00 KSI
 ELASTIC ELEMENTS ARE WHITE PLASTIC ELEMENTS ARE GRAY
 FAILED ELEMENTS ARE BLACK



d) Stress = 1.11 GPa (161 ksi)

Figure 37. Crack Propagation in the Isotropic Carbon Matrix Model Due to Longitudinal Tension Loading at Room Temperature.

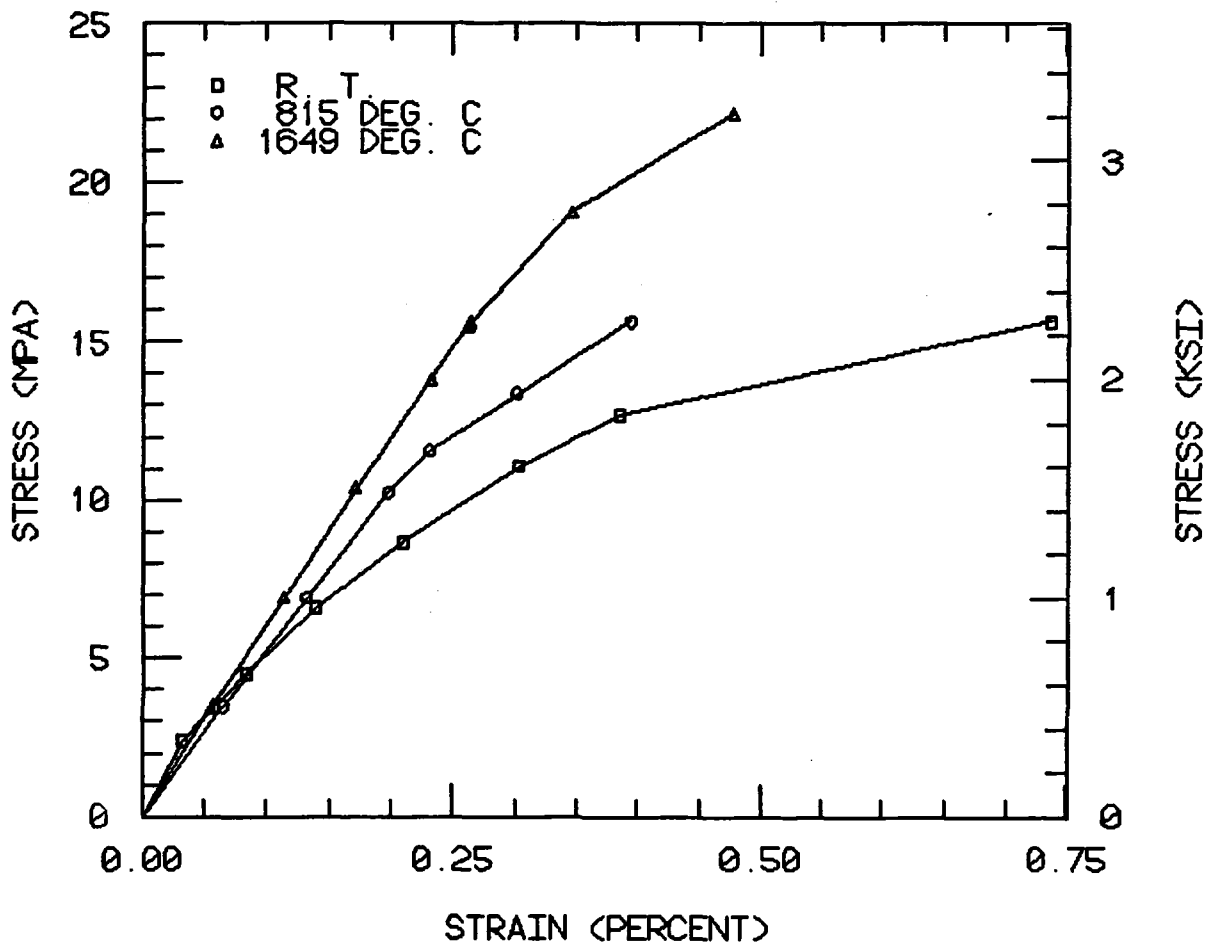
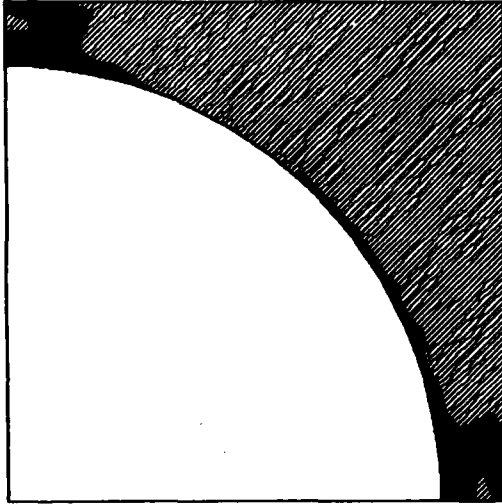


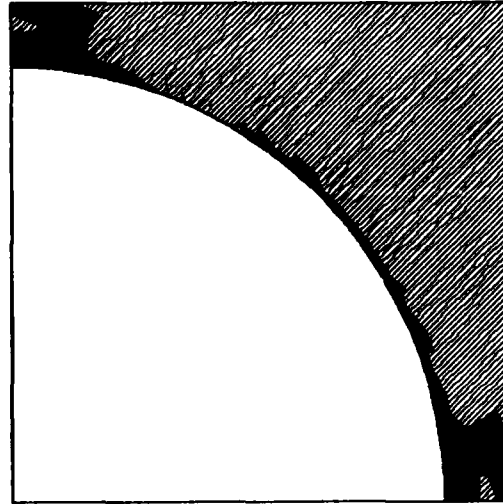
Figure 38. Transverse Tension Stress-Strain Response for the Isotropic Carbon Matrix Model.

FINITE ELEMENT DISPLACEMENT GRID
 TEMP - 21. DEG. C MODS - .00 N INCREMENT NO. - 2 PLOT NO. - 2
 SXX - .00 KSI SYY - .00 KSI SZZ - .00 KSI SYZ - .00 KSI
 SXX - .00 KSI
 ELASTIC ELEMENTS ARE WHITE PLASTIC ELEMENTS ARE GRAY
 FAILED ELEMENTS ARE BLACK



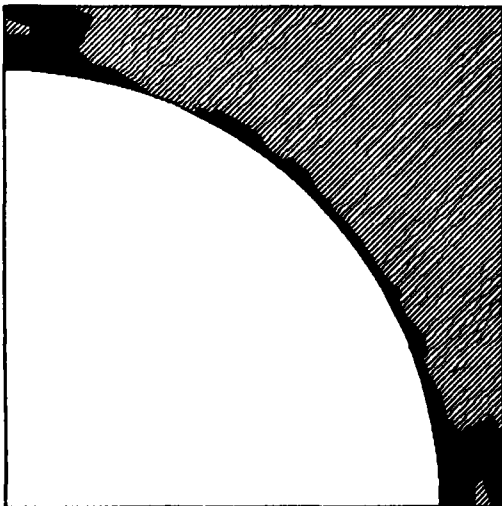
a) Stress = 4.6 MPa (0.66 ksi)

FINITE ELEMENT DISPLACEMENT GRID
 TEMP - 21. DEG. C MODS - .00 N INCREMENT NO. - 4 PLOT NO. - 4
 SXX - 1.26 KSI SYY - .00 KSI SZZ - .00 KSI SYZ - .00 KSI
 SXX - .00 KSI
 ELASTIC ELEMENTS ARE WHITE PLASTIC ELEMENTS ARE GRAY
 FAILED ELEMENTS ARE BLACK



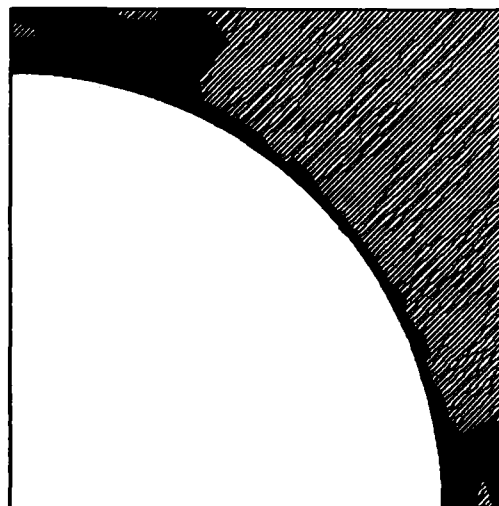
b) Stress = 8.7 MPa (1.26 ksi)

FINITE ELEMENT DISPLACEMENT GRID
 TEMP - 21. DEG. C MODS - .00 N INCREMENT NO. - 6 PLOT NO. - 6
 SXX - 1.60 KSI SYY - .00 KSI SZZ - .00 KSI SYZ - .00 KSI
 SXX - .00 KSI
 ELASTIC ELEMENTS ARE WHITE PLASTIC ELEMENTS ARE GRAY
 FAILED ELEMENTS ARE BLACK



c) Stress = 11.0 MPa (1.60 ksi)

FINITE ELEMENT DISPLACEMENT GRID
 TEMP - 21. DEG. C MODS - .00 N INCREMENT NO. - 7 PLOT NO. - 7
 SXX - 2.27 KSI SYY - .00 KSI SZZ - .00 KSI SYZ - .00 KSI
 SXX - .00 KSI
 ELASTIC ELEMENTS ARE WHITE PLASTIC ELEMENTS ARE GRAY
 FAILED ELEMENTS ARE BLACK



d) Stress = 15.6 MPa (2.27 ksi)

Figure 39. Crack Propagation in the Isotropic Carbon Matrix Due to Transverse Tension Loading at Room Temperature.

has taken place at a low stress level. As the transverse tensile stress increases, further cracking takes place, as shown in Figure 39b for a stress of 8.7 MPa (1.26 ksi), and in Figure 39c for a stress of 11.0 MPa (1.60 ksi). At a stress of 15.7 MPa (2.27 ksi), the cracks join, Figure 39d, separating the model into two pieces, indicating failure of the carbon-carbon fiber bundle. Model status plots for the other two elevated test temperatures were virtually the same, with cracks occurring at slightly different stress levels. The nonlinear character of the stress-strain plots shown in Figure 38 is primarily due to damage propagation in the model rather than inelastic constituent material deformation.

Transverse tensile strength for this isotropic matrix carbon-carbon model increases with increasing temperature, as is apparent in Figure 38. Two factors cause this effect. First, the constituent isotropic carbon matrix strength was assumed to increase slightly with temperature, as was plotted in Figure 30. Second, elevated temperatures tended to relieve part of the thermal residual stress induced during fabrication. A combination of these two factors produced the apparent increase in transverse tensile strength of the unidirectional carbon-carbon fiber bundle.

Longitudinal shear stress-strain curves at room temperature, 815°C, and 1649°C are plotted for the isotropic carbon model in Figure 40. Stress-strain behavior at any of the three temperatures is linear to a "yield" point where the slope of the curve abruptly changes. As can be seen in the room temperature model status plots of Figure 41, this abrupt slope change is due to damage propagation in the model. Some minimal crack extension takes place at 1.5 MPa (220 psi), shown in Figure 41a, and again at 2.3 MPa (340 psi), shown in Figure 41b. At 3.4 MPa (490 psi), the fiber-matrix interface cracks join, resulting in failure of the modeled composite, as shown in Figure 41c. Results for the 815°C and 1649°C longitudinal shear loading cases were very similar. However, at 815°C and 1649°C the final crack extension takes place over two increments instead of just one increment, resulting in the apparent "plastic" deformation shown Figure 41. Note that the longitudinal shear stress levels are relatively low. These modeled carbon-carbon fiber

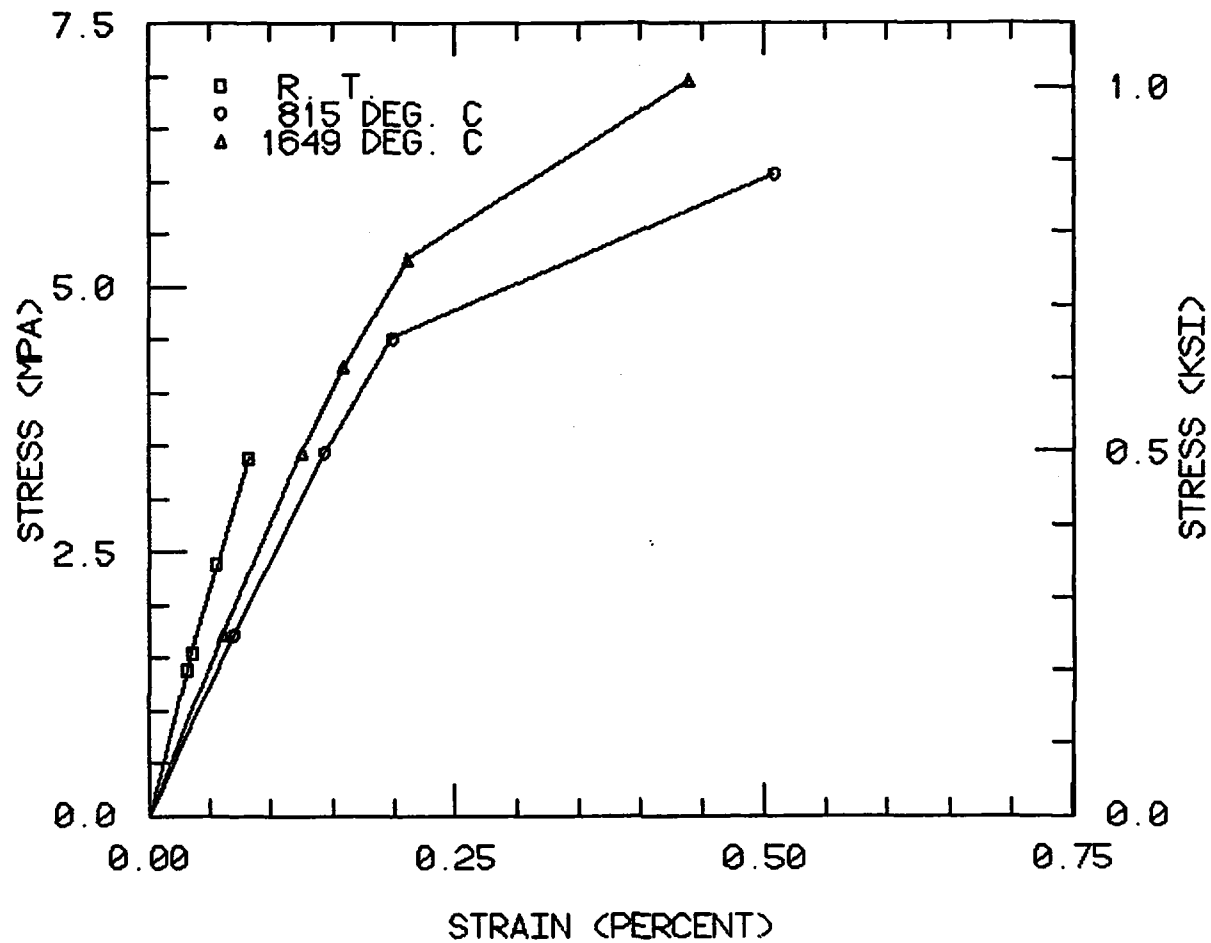
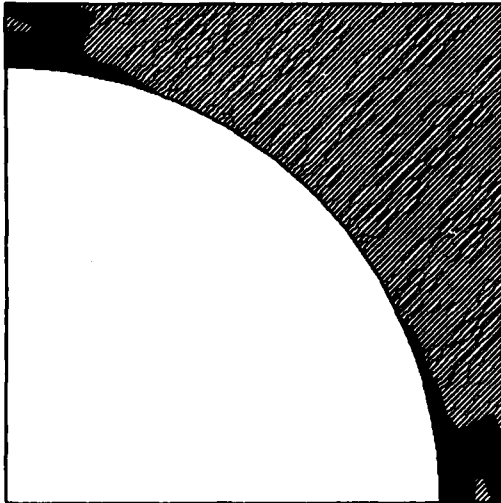


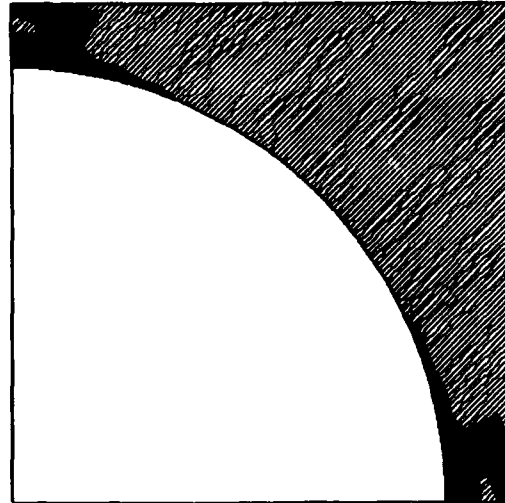
Figure 40. Longitudinal Shear Stress-Strain Response for the Isotropic Carbon Matrix Model.

FINITE ELEMENT DISPLACEMENT GRID
 TEMP - 21. DEG. C MODS - .00 N INCREMENT NO. - 2 PLOT NO. - 2
 SXX - .00 KSI SYY - .00 KSI SZZ - .00 KSI SYZ - .00 KSI
 SXZ - .22 KSI
 ELASTIC ELEMENTS ARE WHITE PLASTIC ELEMENTS ARE GRAY
 FAILED ELEMENTS ARE BLACK



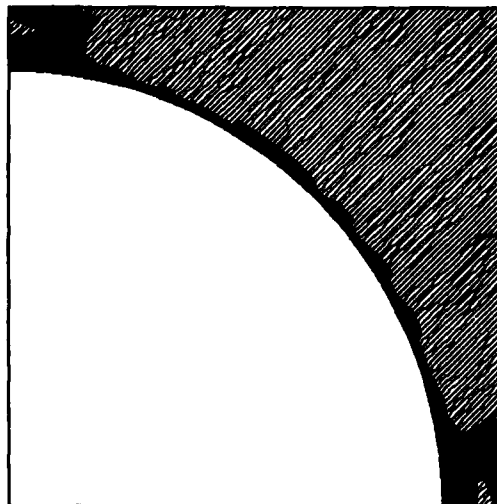
a) Stress = 1.5 MPa (0.22 ksi)

FINITE ELEMENT DISPLACEMENT GRID
 TEMP - 21. DEG. C MODS - .00 N INCREMENT NO. - 3 PLOT NO. - 3
 SXX - .00 KSI SYY - .00 KSI SZZ - .00 KSI SYZ - .00 KSI
 SXZ - .34 KSI
 ELASTIC ELEMENTS ARE WHITE PLASTIC ELEMENTS ARE GRAY
 FAILED ELEMENTS ARE BLACK



b) 2.3 MPa (0.34 ksi)

FINITE ELEMENT DISPLACEMENT GRID
 TEMP - 21. DEG. C MODS - .00 N INCREMENT NO. - 4 PLOT NO. - 4
 SXX - .00 KSI SYY - .00 KSI SZZ - .00 KSI SYZ - .00 KSI
 SXZ - .49 KSI
 ELASTIC ELEMENTS ARE WHITE PLASTIC ELEMENTS ARE GRAY
 FAILED ELEMENTS ARE BLACK



c) 3.4 MPa (0.49 ksi)

Figure 41. Crack Propagation in the Isotropic Carbon Matrix Model Due to Longitudinal Shear Loading at Room Temperature.

bundles have very little shear strength as compared to other composite materials.

Transverse shear stress-strain plots are shown in Figure 42, with associated room temperature model status plots shown in Figure 43. Nonlinear stress-strain behavior is evident in all three curves plotted in Figure 42. Transverse shear strength tends to increase with increasing temperature due to relaxation of the thermal residual stresses with elevated temperature. This tends to delay matrix crack propagation until higher applied mechanical stress levels are achieved.

As shown in Figure 43a, crack propagation takes place virtually throughout the loading history. Elements progressively fail, as shown in Figures 43a, 43b, and 43c for transverse shear stress levels of 3.3 MPa (0.48 ksi), 5.4 MPa (0.79 ksi) and 6.6 MPa (0.95 ksi), respectively. This cracking results in the nonlinear appearance of the room temperature transverse shear stress-strain plot shown in Figure 42.

Thermal expansion coefficients were calculated by applying temperature increments rather than mechanical loading increments. Note, this was a reheating of the model which had already been cooled from the final processing temperature. Thus, the modeled thermal expansion included effects of processing-induced thermal residual stress cracks. The longitudinal thermal strains resulting from this reheating are plotted in Figure 44. As can be seen in Figure 44, the model initially contracts due to a temperature increase, but then expands with increasing temperature. Thermal strains were regression fit with a parabolic equation in temperature. Differentiation of this equation results in a longitudinal thermal expansion coefficient that is linear in temperature, as plotted in Figure 45.

Transverse thermal strain and thermal expansion coefficient are plotted in Figures 46 and 47, respectively. Again, a parabolic equation in temperature was used to represent the thermal strain response, resulting in a transverse thermal expansion coefficient that varies linearly with temperature.

Elastic properties, thermal expansion coefficients, and strengths predicted for the isotropic carbon matrix model are listed in Table 7. Values are listed for all three transverse material constants, i.e., the transverse tensile modulus E_{22} , Poisson's ratio ν_{23} , and shear modulus

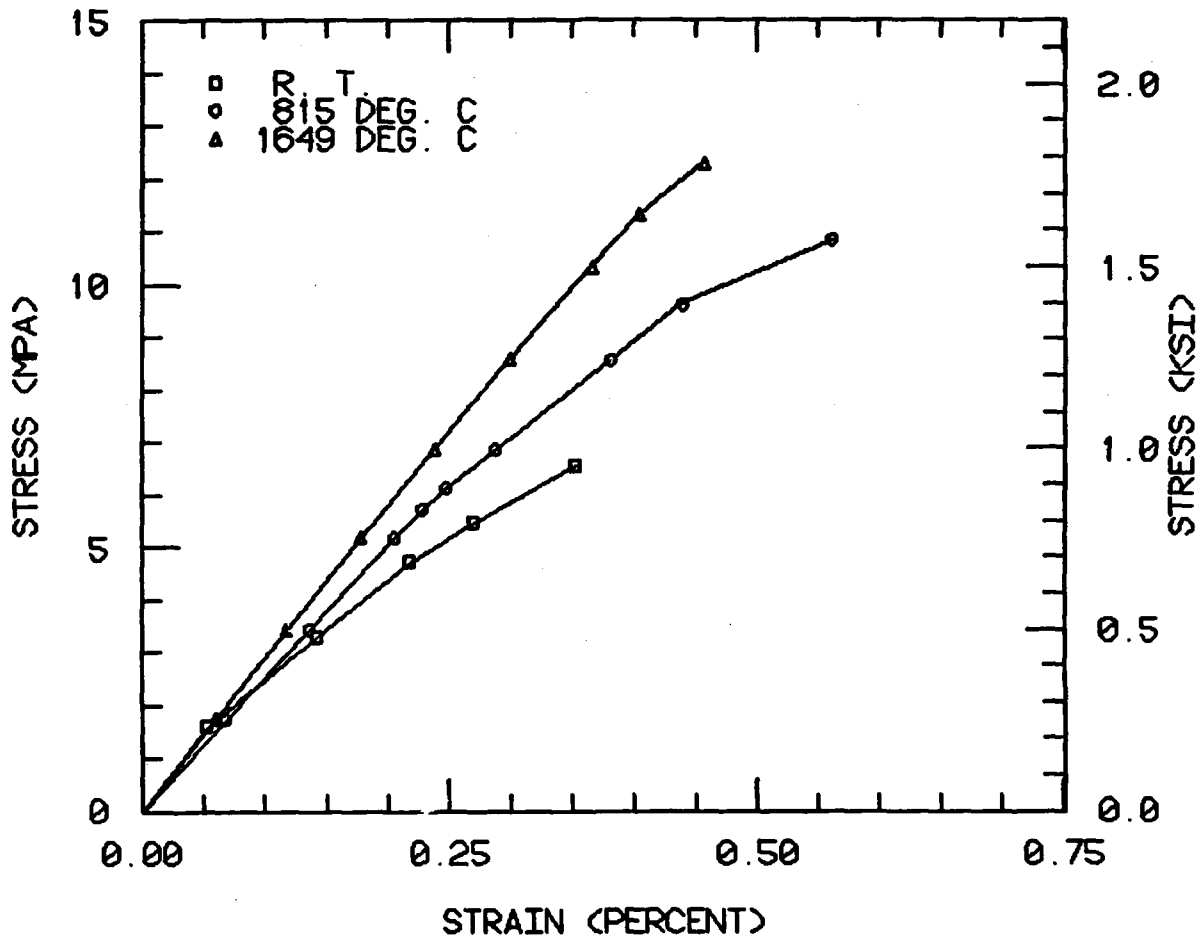
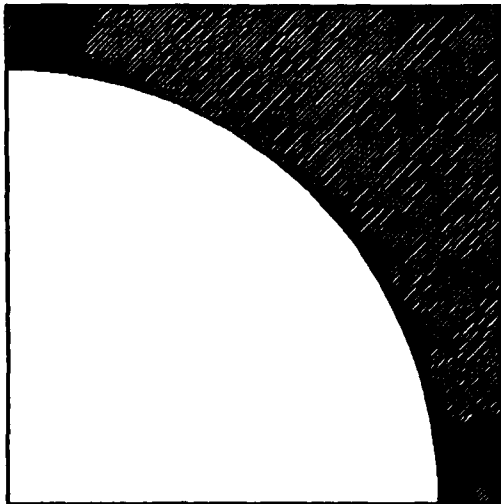


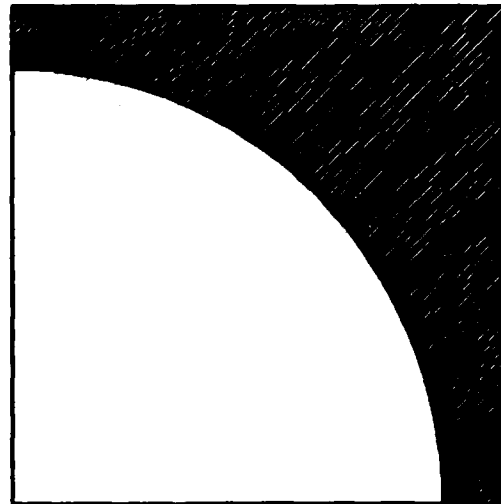
Figure 42. Transverse Shear Stress-Strain Response for the Isotropic Carbon Matrix Model.

FINITE ELEMENT DEFORMATION GRID
 TEMP - 21.000 C MODS - .00 S INCREMENT NO. - 2 PLOT NO. - 2
 SXX - .00 MIE SYY - -.00 MIE SZZ - .00 MIE SXZ - .00 MIE
 SXY - .00 MIE
 ELASTIC ELEMENTS ARE WHITE PLASTIC ELEMENTS ARE GRAY
 FAILED ELEMENTS ARE BLACK



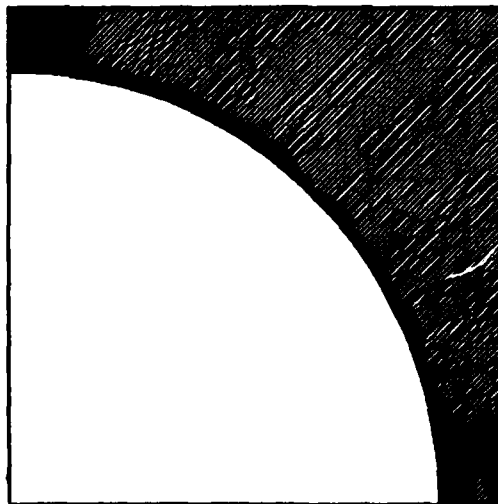
a) Stress = 3.3 MPa (0.48 ksi)

FINITE ELEMENT DEFORMATION GRID
 TEMP - 21.000 C MODS - .00 S INCREMENT NO. - 4 PLOT NO. - 4
 SXX - .70 MIE SYY - -.70 MIE SZZ - .00 MIE SXZ - .00 MIE
 SXY - .00 MIE
 ELASTIC ELEMENTS ARE WHITE PLASTIC ELEMENTS ARE GRAY
 FAILED ELEMENTS ARE BLACK



b) Stress = 5.4 MPa (0.79 ksi)

FINITE ELEMENT DEFORMATION GRID
 TEMP - 21.000 C MODS - .00 S INCREMENT NO. - 6 PLOT NO. - 6
 SXX - .00 MIE SYY - -.00 MIE SZZ - .00 MIE SXZ - .00 MIE
 SXY - .00 MIE
 ELASTIC ELEMENTS ARE WHITE PLASTIC ELEMENTS ARE GRAY
 FAILED ELEMENTS ARE BLACK



c) Stress = 6.6 MPa (0.95 ksi)

Figure 43. Crack Propagation in the Isotropic Carbon Matrix Model Due to Transverse Shear Loading at Room Temperature.

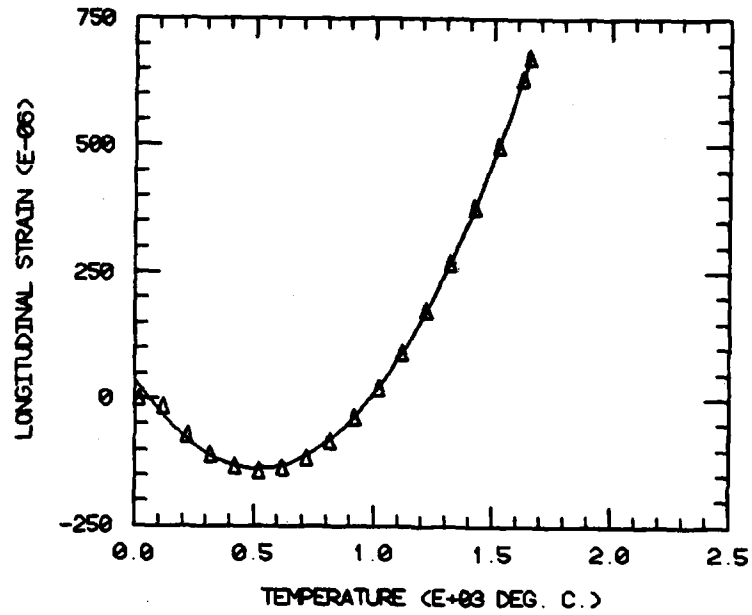


Figure 44. Longitudinal Thermal Strain for the Isotropic Carbon Matrix Model.

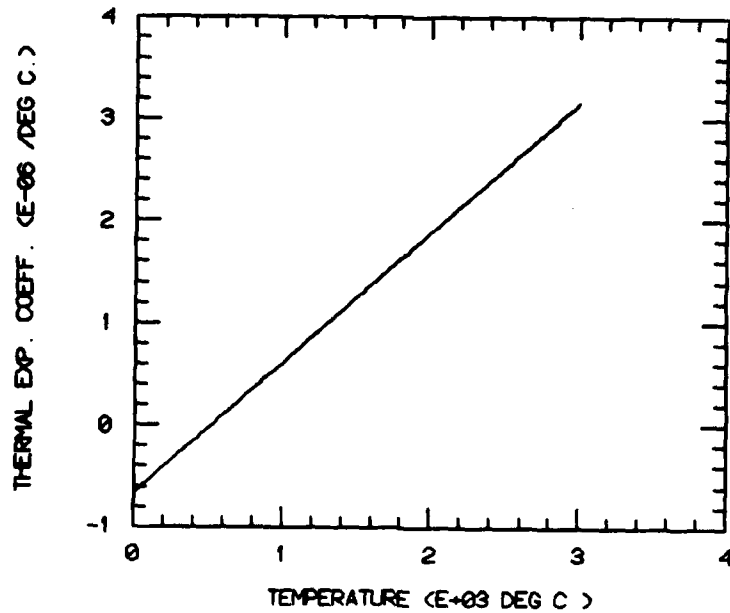


Figure 45. Longitudinal Thermal Expansion Coefficient for the Isotropic Carbon Matrix Model.

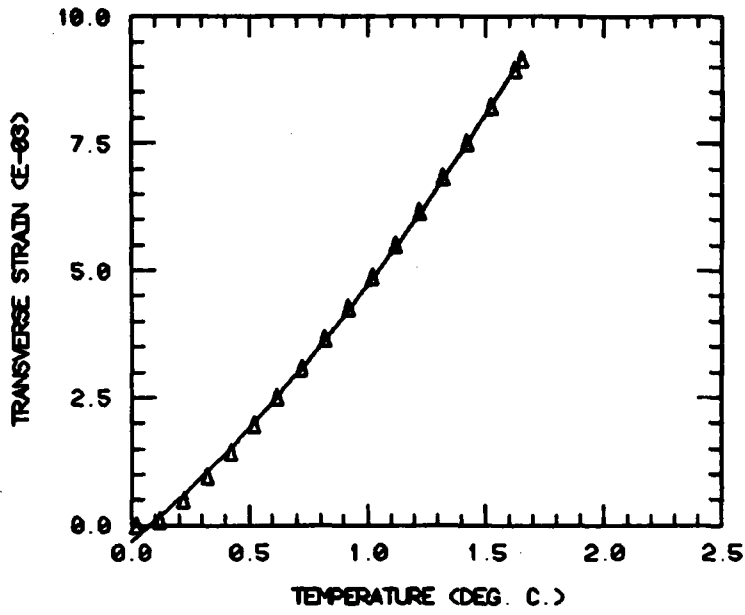


Figure 46. Transverse Thermal Strain for the Isotropic Carbon Matrix Model.

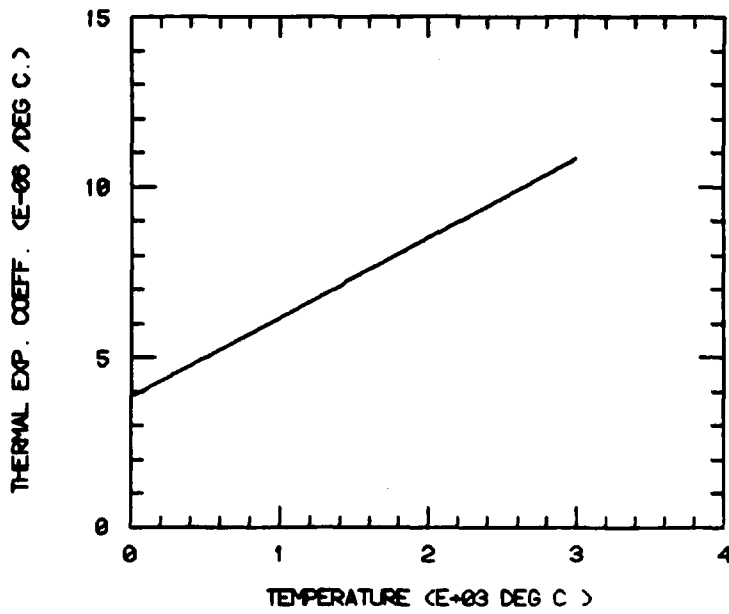


Figure 47. Transverse Thermal Expansion Coefficient for the Isotropic Carbon Matrix Model.

TABLE 7

Micromechanics Predictions of Thermomechanical Properties for a Unidirectional Carbon-Carbon Fiber Bundle, Isotropic Carbon Matrix Model

Temperature (°C)	Tensile Moduli			Shear Moduli			Poisson's Ratios			
	E ₁₁ (GPa)	E ₂₂ (GPa)	E ₂₂ (Msi)	G ₁₂ (GPa)	G ₁₂ (Msi)	G ₂₃ (GPa)	ν ₁₂	ν ₂₃		
21	218	31.6	5.3	0.77	4.3	0.63	3.0	0.43	0.21	0.22
815	225	32.7	5.2	0.76	2.5	0.36	2.6	0.37	0.19	0.14
1649	198	28.7	6.1	0.88	2.8	0.41	2.9	0.42	0.23	0.16

Temperature (°C)	Tensile Strengths			Shear Strengths			
	S ₁₁ ^{ut} (GPa)	S ₂₂ ^{ut} (MPa)	S ₂₂ ^{ut} (ksi)	S ₁₂ ^{us} (MPa)	S ₁₂ ^{us} (ksi)	S ₂₃ ^{us} (MPa)	S ₂₃ ^{us} (ksi)
21	1.11	161	2.27	3.4	0.49	6.6	0.95
815	0.93	135	2.27	6.1	0.88	10.8	1.57
1649	0.98	142	3.22	7.0	1.01	12.3	1.79

Thermal Expansion α₁₁ = -0.664 + 0.00133T

Coefficient (10⁻⁶/°C) α₂₂ = 3.85 + 0.00233T

G_{23} . These constants are not independent if the unidirectional composite is globally transversely isotropic. The presence of cracks does disrupt that assumption, however. As can be seen in Table 7, the three constants do tend to obey the transverse isotropy assumption for all three modeled temperatures. These constants listed in Table 7 were used to define carbon-carbon fiber bundle properties used in the micromechanics model discussed in Section 5 of this report.

4.4 Axial Sheath Micromechanics Model Results

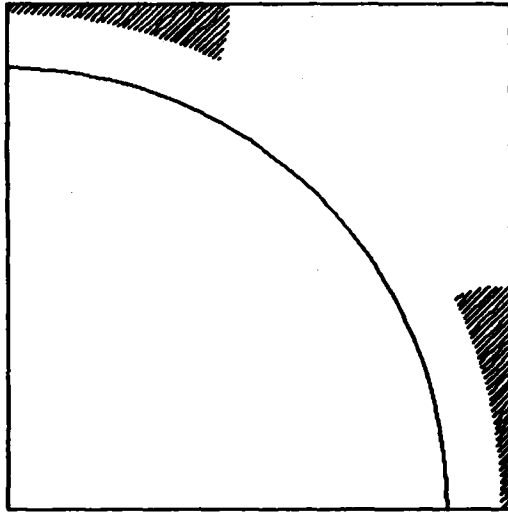
During processing of carbon-carbon composite materials, an oriented sheath of carbon matrix typically forms around individual fibers within the fiber bundle. This sheath tends to orient its stiffer material direction parallel to the fiber, in effect producing a composite with a larger volume fraction of fiber. In order to model this sheath material with the micromechanics analysis, the finite element mesh previously shown as Figure 7 in Section 3 was used.

The sheath region was modeled as a separate constituent material. For this axial sheath analysis; sheath properties were assumed to be the same as those of the fiber, with two exceptions. First, the longitudinal strength of the sheath was arbitrarily assumed to be 50 percent that of the longitudinal fiber strength. In-plane (plane of transverse isotropy) strengths of the sheath were assumed to be the same as the matrix strengths. A Tsai-Hill [73] failure criterion was used to define failures in the sheath. The matrix region was again assumed to be isotropic.

A fiber volume fraction of 60 percent was also used in this axial sheath model, the same fiber volume fraction as was used in the isotropic carbon matrix model. The sheath region occupied 16 percent of the volume, leaving a matrix volume content of 24 percent.

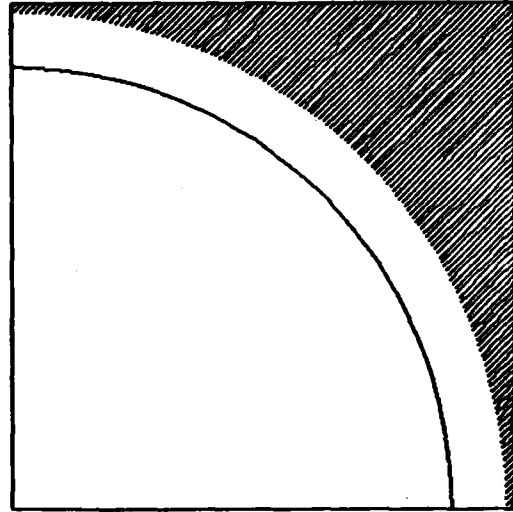
Thermal residual stresses were also included in this model, using an initial stress-free temperature of 2204°C and cooling increments of 50°C. Model status plots during cooling are shown in Figure 48. Inelastic material behavior occurs in the matrix material at 2004°C, as shown in Figure 48a. The entire matrix has undergone inelastic deformation at 1904°C, as shown in Figure 48b. Cracks begin to form in the matrix material near the axial sheath-matrix interface at 204°C, as shown in Figure 48c, resulting in the final room temperature state of

FINE ELEMENT DEFORMATION GRID
 TEMP - 204. DEG. C NOD - 80 S JOINT NO. - 4 PLOT NO. - 4
 SX - .80 ME SY - .80 ME SZ - .80 ME SE - .80 ME
 SEZ - .80 ME
 ELASTIC ELEMENTS ARE WHITE PLASTIC ELEMENTS ARE GRAY
 FAILED ELEMENTS ARE BLACK



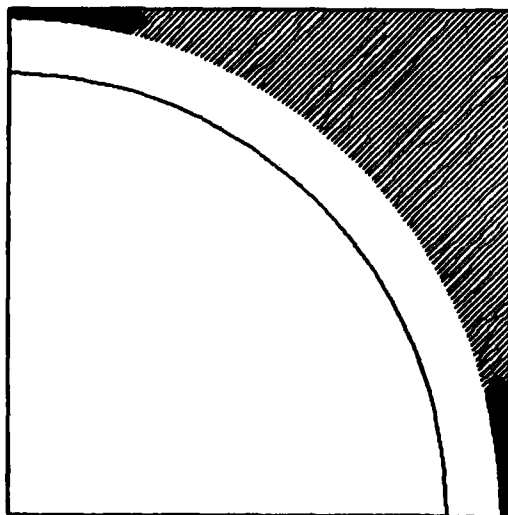
a) Temperature=2004°C

FINE ELEMENT DEFORMATION GRID
 TEMP - 204. DEG. C NOD - 80 S JOINT NO. - 80 PLOT NO. - 80
 SX - .80 ME SY - .80 ME SZ - .80 ME SE - .80 ME
 SEZ - .80 ME
 ELASTIC ELEMENTS ARE WHITE PLASTIC ELEMENTS ARE GRAY
 FAILED ELEMENTS ARE BLACK



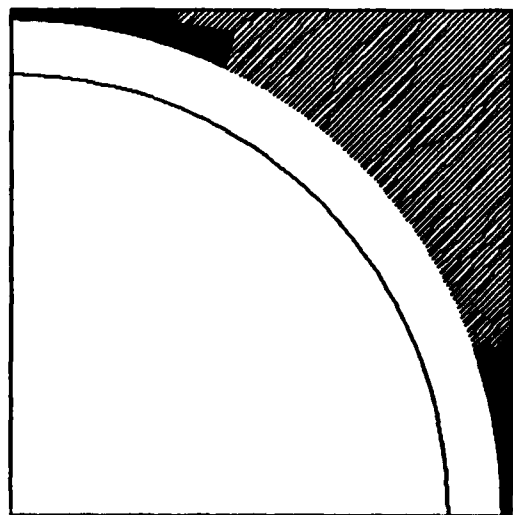
b) Temperature=1904°C

FINE ELEMENT DEFORMATION GRID
 TEMP - 204. DEG. C NOD - 80 S JOINT NO. - 40 PLOT NO. - 40
 SX - .80 ME SY - .80 ME SZ - .80 ME SE - .80 ME
 SEZ - .80 ME
 ELASTIC ELEMENTS ARE WHITE PLASTIC ELEMENTS ARE GRAY
 FAILED ELEMENTS ARE BLACK



c) Temperature=204°C

FINE ELEMENT DEFORMATION GRID
 TEMP - 21. DEG. C NOD - 80 S JOINT NO. - 41 PLOT NO. - 41
 SX - .80 ME SY - .80 ME SZ - .80 ME SE - .80 ME
 SEZ - .80 ME
 ELASTIC ELEMENTS ARE WHITE PLASTIC ELEMENTS ARE GRAY
 FAILED ELEMENTS ARE BLACK



d) Temperature=Room Temperature

Figure 48. Crack Propagation in the Axial Sheath Model Due to Thermal Residual Stresses, $\alpha_{22}/\alpha_m \approx 2.0$.

the model shown in Figure 48d. Although cracks are present at room temperature, the model is not divided into two separate regions. Therefore, mechanical loads may still be applied. The same mechanical stresses, i.e., longitudinal tension, transverse tension, longitudinal shear, and transverse shear were applied to this model. Modeled environments were room temperature, 815°C, and 1649°C.

Longitudinal stress-strain plots for the axial sheath model are shown in Figure 49. The stress-strain behavior shown in Figure 49 is not linear; there is a point on each curve at which the curve abruptly changes slope. The initial elastic modulus of the room temperature curve, marked with squares, is 274 GPa (39.7 Msi), decreasing at approximately 765 MPa (111 ksi) to a value of 272 GPa (39.4 Msi). The slope change is due to failure of the axial sheath, as can be seen in the model status plots shown in Figure 50. Figure 50a shows the model at an applied longitudinal tensile stress of 400 MPa (58 ksi). Some matrix cracking is present. At 641 MPa (93 ksi), further cracking of the matrix takes place, as shown in Figure 50b. Essentially all of the matrix has failed. However, failure of the matrix produces no apparent stiffness reduction in the room temperature stress-strain plot of Figure 49. At 765 MPa (111 ksi), the sheath totally fails, as shown in Figure 50c, reducing the apparent stiffness of the modeled carbon-carbon fiber bundle and producing the slope change of the plot in Figure 49. At 1.14 GPa (165 ksi) the entire model fails abruptly when the fiber fails, as shown in Figure 50d.

Transverse tension stress-strain behavior is also nonlinear, as shown in Figure 51. Final failure of the model takes place due to cracking in the matrix material, as shown for the room temperature loading case in Figure 52. A small number of sheath elements also fail near the 45° diagonal of the model, as indicated in Figures 52c and 52d.

Longitudinal shear stress-strain plots are shown in Figure 53. The corresponding crack propagation plots for the room temperature environment are shown in Figure 54. As can be seen in Figure 54, considerable cracking takes place in the sheath near the 45° diagonal of the model. The 45° diagonal is the region in which fibers are farthest apart for the assumed square fiber packing array.

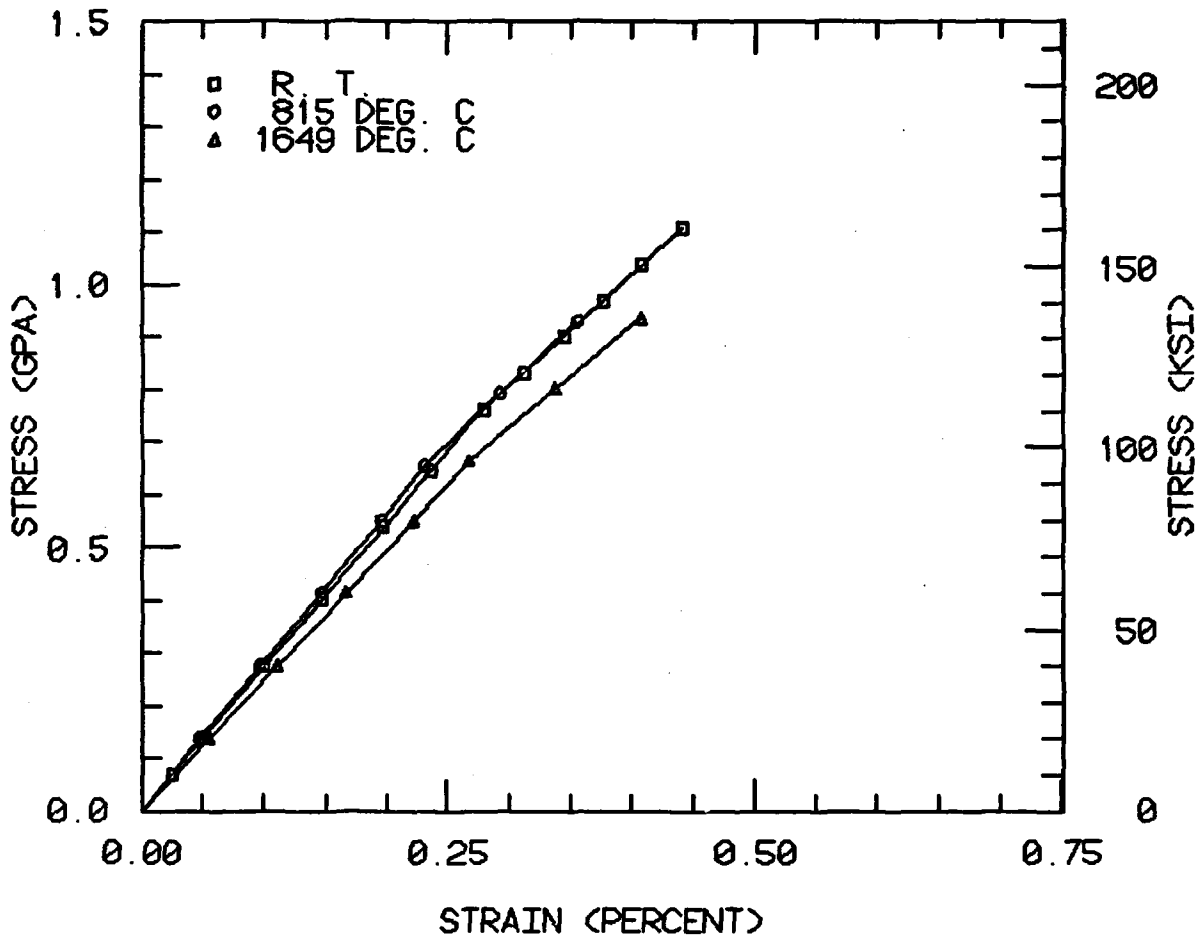
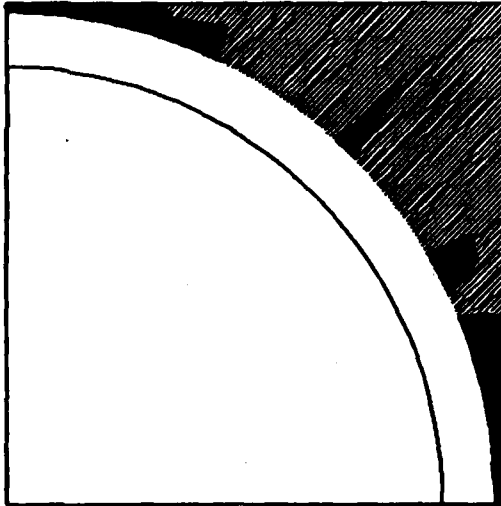


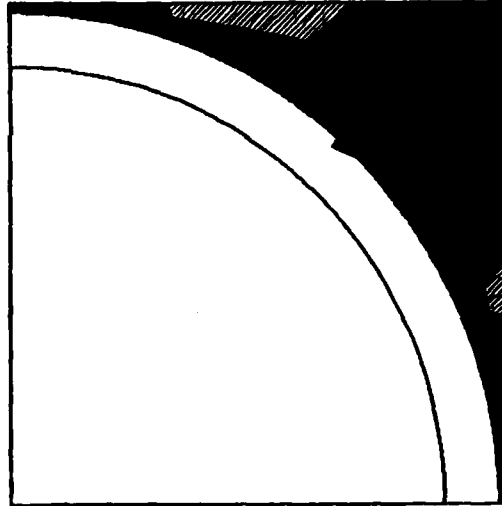
Figure 49. Longitudinal Tension Stress-Strain Response for the Axial Sheath Model.

FINE ELEMENT DEFORMATION GRID
 TEMP - 21. DEG. C MOD - .00 S INCREMENT NO. - 4 PLOT NO. - 4
 DRX - .00 MIE DRY - .00 MIE SZZ - 00.01 MIE SYZ - .00 MIE
 SZX - .00 MIE
 ELASTIC ELEMENTS ARE WHITE PLASTIC ELEMENTS ARE GRAY
 FAILED ELEMENTS ARE BLACK



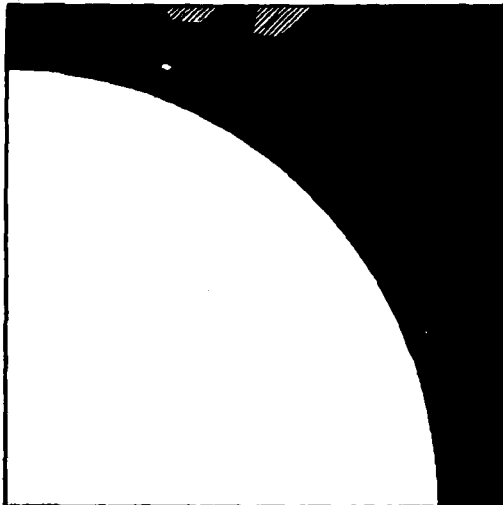
a) Stress = 400 MPa (58 ksi)

FINE ELEMENT DEFORMATION GRID
 TEMP - 21. DEG. C MOD - .00 S INCREMENT NO. - 6 PLOT NO. - 6
 DRX - .00 MIE DRY - .00 MIE SZZ - 00.42 MIE SYZ - .00 MIE
 SZX - .00 MIE
 ELASTIC ELEMENTS ARE WHITE PLASTIC ELEMENTS ARE GRAY
 FAILED ELEMENTS ARE BLACK



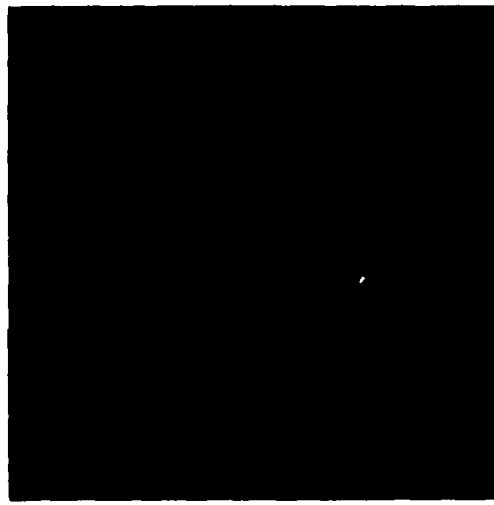
b) Stress = 641 MPa (93 ksi)

FINE ELEMENT DEFORMATION GRID
 TEMP - 21. DEG. C MOD - .00 S INCREMENT NO. - 7 PLOT NO. - 7
 DRX - .00 MIE DRY - .00 MIE SZZ - 110.70 MIE SYZ - .00 MIE
 SZX - .00 MIE
 ELASTIC ELEMENTS ARE WHITE PLASTIC ELEMENTS ARE GRAY
 FAILED ELEMENTS ARE BLACK



c) Stress = 765 MPa (111 ksi)

FINE ELEMENT DEFORMATION GRID
 TEMP - 21. DEG. C MOD - .00 S INCREMENT NO. - 20 PLOT NO. - 20
 DRX - .00 MIE DRY - .00 MIE SZZ - 100.00 MIE SYZ - .00 MIE
 SZX - .00 MIE
 ELASTIC ELEMENTS ARE WHITE PLASTIC ELEMENTS ARE GRAY
 FAILED ELEMENTS ARE BLACK



d) Stress = 1.13 GPa (165 ksi)

Figure 50. Crack Propagation in the Axial Sheath Model Due to Longitudinal Tension Loading at Room Temperature.

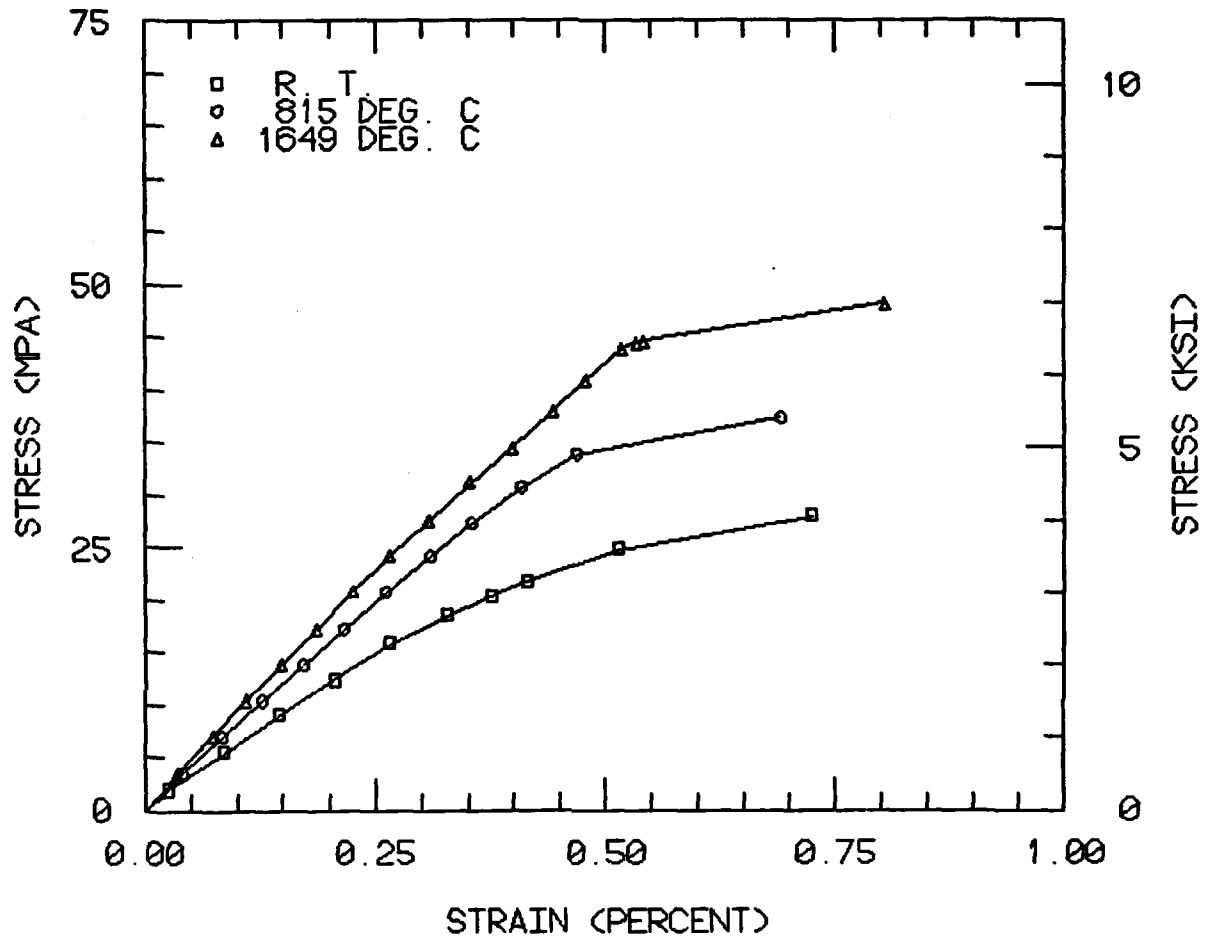
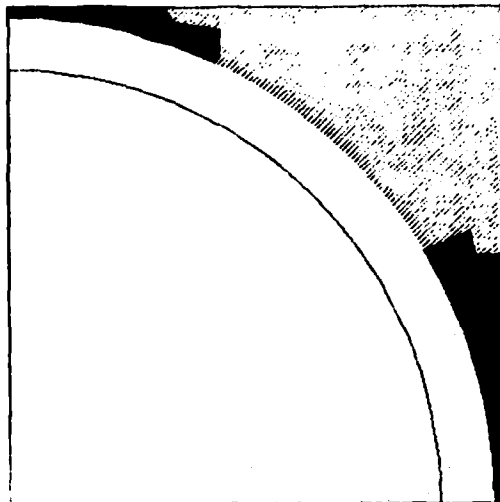


Figure 51. Transverse Tension Stress-Strain Response for the Axial Sheath Model.

FINITE ELEMENT DISPLACEMENT GRID
 TEMP - 21. DEG. C MODS - .00 N INCREMENT NO - 2 PLOT NO - 2
 SX1 - 70 KSI SY1 - .00 KSI SZ1 - .00 KSI SX2 - .00 KSI
 SY2 - .00 KSI SZ2 - .00 KSI
 ELASTIC ELEMENTS ARE WHITE PLASTIC ELEMENTS ARE GRAY
 FAILED ELEMENTS ARE BLACK



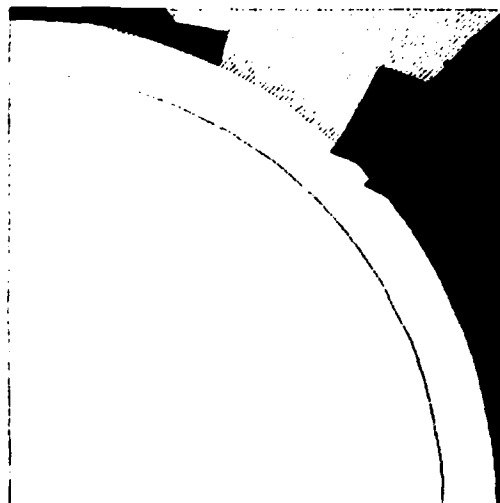
a) Stress = 5.4 MPa (0.79 ksi)

FINITE ELEMENT DISPLACEMENT GRID
 TEMP - 21. DEG. C MODS - .00 N INCREMENT NO - 6 PLOT NO - 6
 SX1 - 140 KSI SY1 - .00 KSI SZ1 - .00 KSI SX2 - .00 KSI
 SY2 - .00 KSI SZ2 - .00 KSI
 ELASTIC ELEMENTS ARE WHITE PLASTIC ELEMENTS ARE GRAY
 FAILED ELEMENTS ARE BLACK



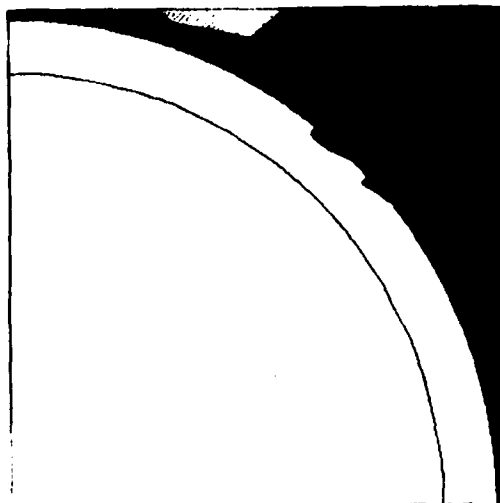
b) Stress = 18.4 MPa (2.67 ksi)

FINITE ELEMENT DISPLACEMENT GRID
 TEMP - 21. DEG. C MODS - .00 N INCREMENT NO - 9 PLOT NO - 9
 SX1 - 210 KSI SY1 - .00 KSI SZ1 - .00 KSI SX2 - .00 KSI
 SY2 - .00 KSI SZ2 - .00 KSI
 ELASTIC ELEMENTS ARE WHITE PLASTIC ELEMENTS ARE GRAY
 FAILED ELEMENTS ARE BLACK



c) Stress = 24.8 MPa (3.59 ksi)

FINITE ELEMENT DISPLACEMENT GRID
 TEMP - 21. DEG. C MODS - .00 N INCREMENT NO - 10 PLOT NO - 10
 SX1 - 4.04 KSI SY1 - .00 KSI SZ1 - .00 KSI SX2 - .00 KSI
 SY2 - .00 KSI SZ2 - .00 KSI
 ELASTIC ELEMENTS ARE WHITE PLASTIC ELEMENTS ARE GRAY
 FAILED ELEMENTS ARE BLACK



d) Stress = 27.9 MPa (4.04 ksi)

Figure 52. Crack Propagation in the Axial Sheath Model Due to Transverse Tension Loading at Room Temperature.

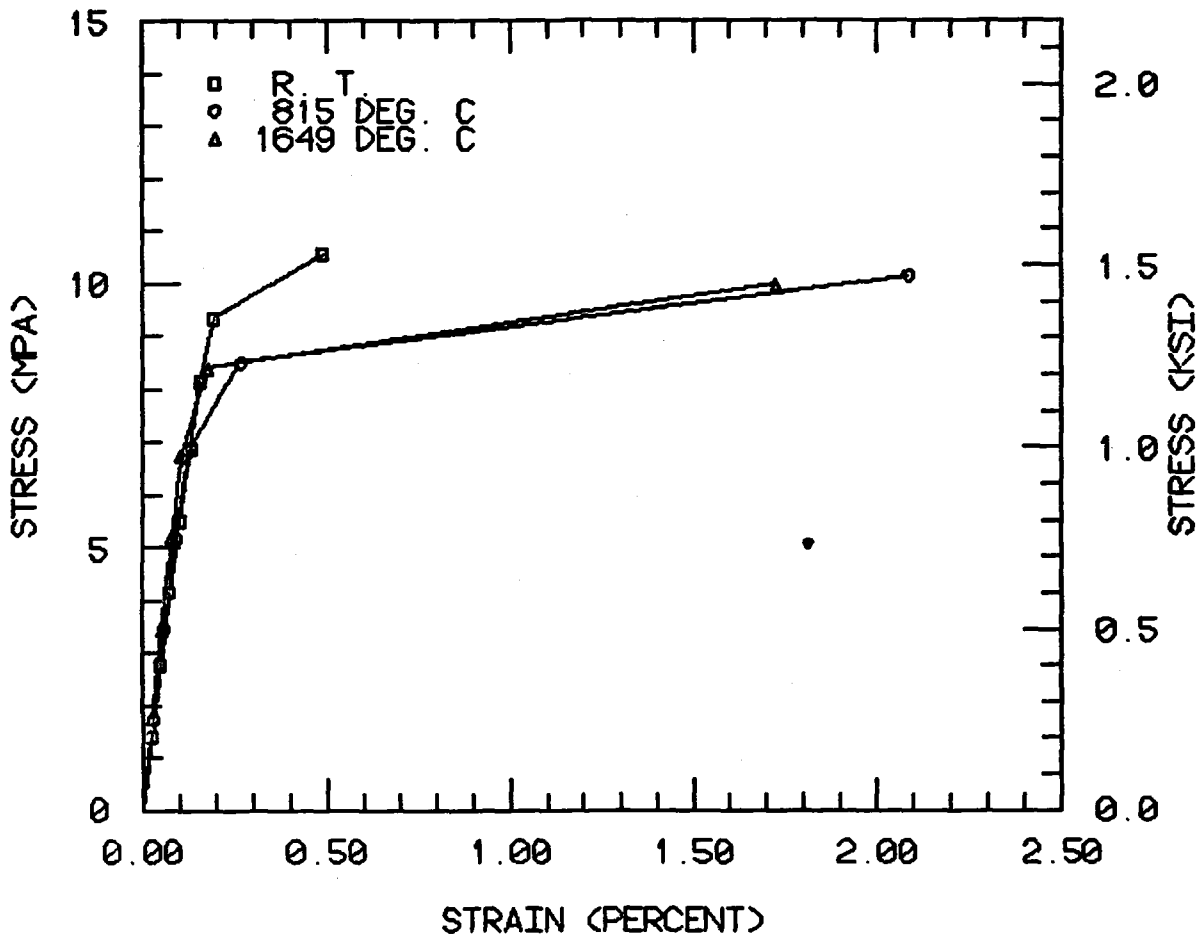
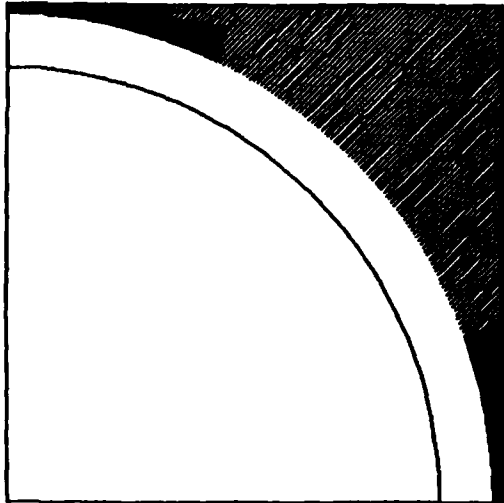


Figure 53. Longitudinal Shear Stress-Strain Response for the Axial Sheath Model.

FINITE ELEMENT DISPLACEMENT GRID
 TEMP - 21. DEG. C MOD - .00 N INCREMENT NO. - 2 PLOT NO. - 2
 SXX - .00 MEG SYY - .00 MEG SZZ - .00 MEG SYZ - .00 MEG
 SXX - .00 MEG SYY - .00 MEG SZZ - .00 MEG SYZ - .00 MEG
 ELASTIC ELEMENTS ARE WHITE PLASTIC ELEMENTS ARE GRAY
 FAILED ELEMENTS ARE BLACK



a) Stress = 2.8 MPa (0.40 ksi)

FINITE ELEMENT DISPLACEMENT GRID
 TEMP - 21. DEG. C MOD - .00 N INCREMENT NO. - 6 PLOT NO. - 6
 SXX - .00 MEG SYY - .00 MEG SZZ - .00 MEG SYZ - .00 MEG
 SXX - .00 MEG SYY - .00 MEG SZZ - .00 MEG SYZ - .00 MEG
 ELASTIC ELEMENTS ARE WHITE PLASTIC ELEMENTS ARE GRAY
 FAILED ELEMENTS ARE BLACK



b) Stress = 8.1 MPa (1.18 ksi)

FINITE ELEMENT DISPLACEMENT GRID
 TEMP - 21. DEG. C MOD - .00 N INCREMENT NO. - 7 PLOT NO. - 7
 SXX - .00 MEG SYY - .00 MEG SZZ - .00 MEG SYZ - .00 MEG
 SXX - .00 MEG SYY - .00 MEG SZZ - .00 MEG SYZ - .00 MEG
 ELASTIC ELEMENTS ARE WHITE PLASTIC ELEMENTS ARE GRAY
 FAILED ELEMENTS ARE BLACK



c) Stress = 9.4 MPa (1.36 ksi)

FINITE ELEMENT DISPLACEMENT GRID
 TEMP - 21. DEG. C MOD - .00 N INCREMENT NO. - 8 PLOT NO. - 8
 SXX - .00 MEG SYY - .00 MEG SZZ - .00 MEG SYZ - .00 MEG
 SXX - .00 MEG SYY - .00 MEG SZZ - .00 MEG SYZ - .00 MEG
 ELASTIC ELEMENTS ARE WHITE PLASTIC ELEMENTS ARE GRAY
 FAILED ELEMENTS ARE BLACK



d) Stress = 10.5 MPa (1.53 ksi)

Figure 54. Crack Propagation in the Axial Sheath Model Due to Longitudinal Shear Loading at Room Temperature.

Results for transverse shear loading of the axial sheath model are shown in Figures 55 and 56. Again, cracking takes place in the matrix regions near the horizontal and vertical axes of the model, but the sheath fails near the 45° diagonal, as shown in Figure 56.

Thermal strains and thermal expansion coefficients are plotted for the axial sheath model in Figures 57 through 60. As was done for the isotropic matrix model, parabolic polynomials in temperature were regression fit to the thermal strain data, Figures 57 and 59. The linear derivatives thus represent the thermal expansion coefficients α_{11} and α_{22} plotted in Figures 58 and 60, respectively.

Predicted properties for the axial sheath model are tabulated in Table 8. Trends with temperature are similar to the trends predicted with the isotropic carbon matrix model, listed previously in Table 7.

Comparing results between Tables 7 and 8, it can be seen that the longitudinal stiffness of the axial sheath model is higher at all temperatures than corresponding values predicted with the isotropic carbon matrix model. This is to be expected due to the added longitudinal stiffness of the sheath. Transverse tensile and longitudinal shear moduli of the axial sheath model are also higher. The transverse shear moduli for the axial sheath model and the isotropic carbon matrix model are similar.

Predicted longitudinal tensile strengths are the same for both models. As this strength is dominated by the strength of the fiber, this result is also expected. Transverse tensile strengths and shear strengths for the axial sheath model are greater than those predicted for the isotropic carbon matrix model.

Thermal expansion results from the two models are also similar, as can be seen by comparing Figures 57 through 60 for the axial sheath model and Figures 44 through 47 for the isotropic carbon matrix model.

Some limited experimental results were available to compare with the fiber bundle predicted properties presented here. As summarized in a previous report [3], single axial fiber bundles were extracted from FMI Billet No. 2208 and tested in tension. Measured tensile moduli values were quite scattered, but were consistently greater than calculated "rule-of-mixture" values for carbon-carbon fiber bundle composites with no sheath. Thus, the stiffening effect of the sheath was again

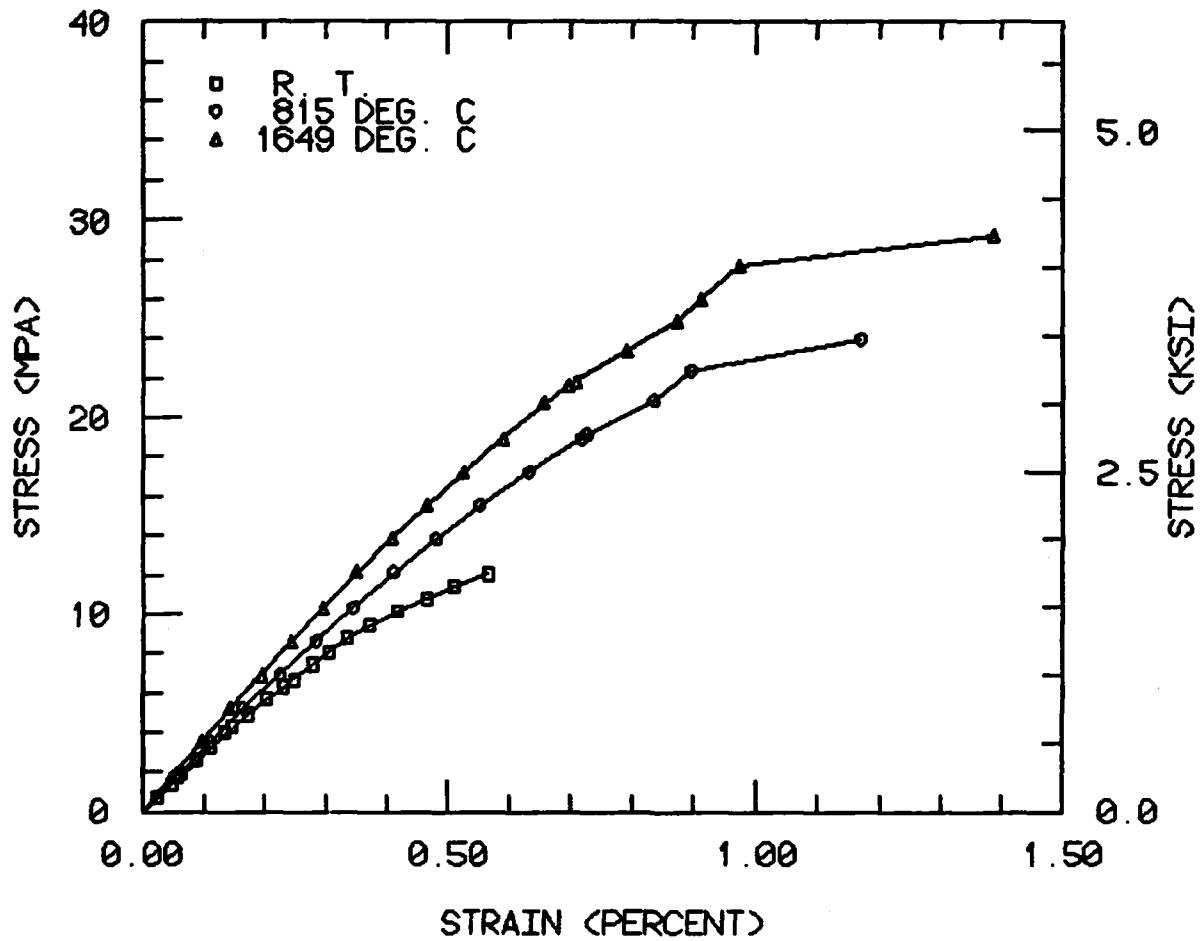
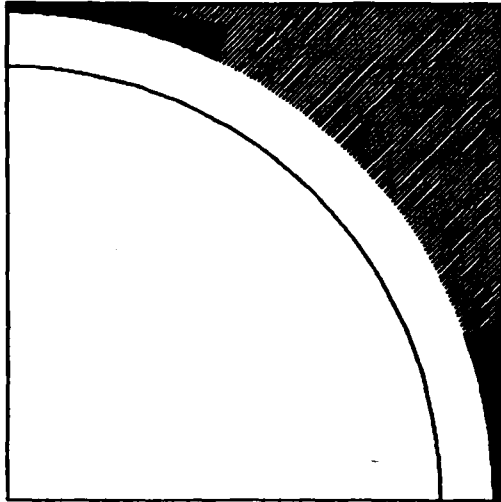


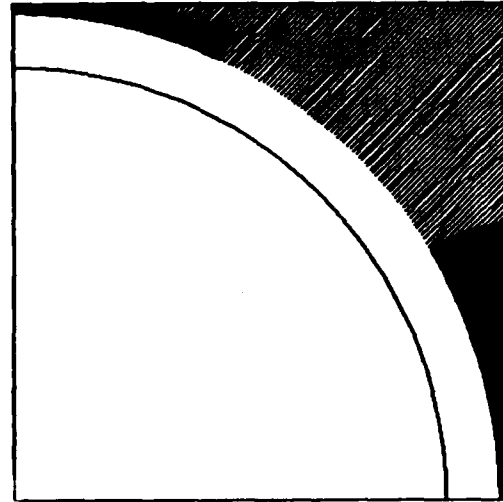
Figure 55. Transverse Shear Stress-Strain Response for the Axial Sheath Model.

FINITE ELEMENT DISPLACEMENT GRID
 TEMP - 21 DEG C MODS - 00 N INCREMENT NO - 2 PLOT NO - 2
 SXX - .20 KSI SYY - -.20 KSI SZZ - .00 KSI SYZ - .00 KSI
 SZX - .00 KSI
 ELASTIC ELEMENTS ARE WHITE PLASTIC ELEMENTS ARE GRAY
 FAILED ELEMENTS ARE BLACK



a) Stress = 1.4 MPa (0.20 ksi)

FINITE ELEMENT DISPLACEMENT GRID
 TEMP - 21 DEG C MODS - 00 N INCREMENT NO - 8 PLOT NO - 8
 SXX - .71 KSI SYY - -.71 KSI SZZ - .00 KSI SYZ - .00 KSI
 SZX - .00 KSI
 ELASTIC ELEMENTS ARE WHITE PLASTIC ELEMENTS ARE GRAY
 FAILED ELEMENTS ARE BLACK



b) Stress = 4.9 MPa (0.71 ksi)

FINITE ELEMENT DISPLACEMENT GRID
 TEMP - 21 DEG C MODS - 00 N INCREMENT NO - 17 PLOT NO - 17
 SXX - 1.46 KSI SYY - -1.46 KSI SZZ - .00 KSI SYZ - .00 KSI
 SZX - .00 KSI
 ELASTIC ELEMENTS ARE WHITE PLASTIC ELEMENTS ARE GRAY
 FAILED ELEMENTS ARE BLACK



c) Stress = 10.1 MPa (1.46 ksi)

FINITE ELEMENT DISPLACEMENT GRID
 TEMP - 21 DEG C MODS - 00 N INCREMENT NO - 20 PLOT NO - 20
 SXX - 1.75 KSI SYY - -1.75 KSI SZZ - .00 KSI SYZ - .00 KSI
 SZX - .00 KSI
 ELASTIC ELEMENTS ARE WHITE PLASTIC ELEMENTS ARE GRAY
 FAILED ELEMENTS ARE BLACK



d) Stress = 12.1 MPa (1.75 ksi)

Figure 56. Crack Propagation in the Axial Sheath Model Due to Transverse Shear Loading at Room Temperature.

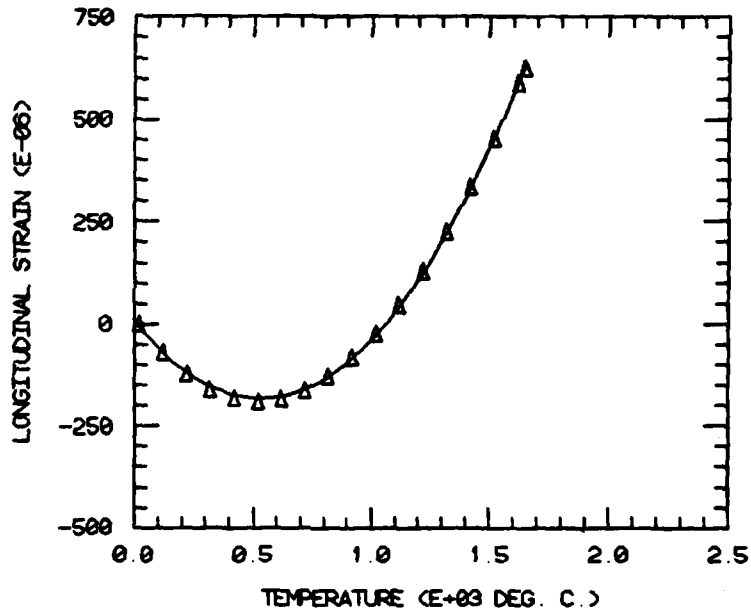


Figure 57. Longitudinal Thermal Strain for the Axial Sheath Model.

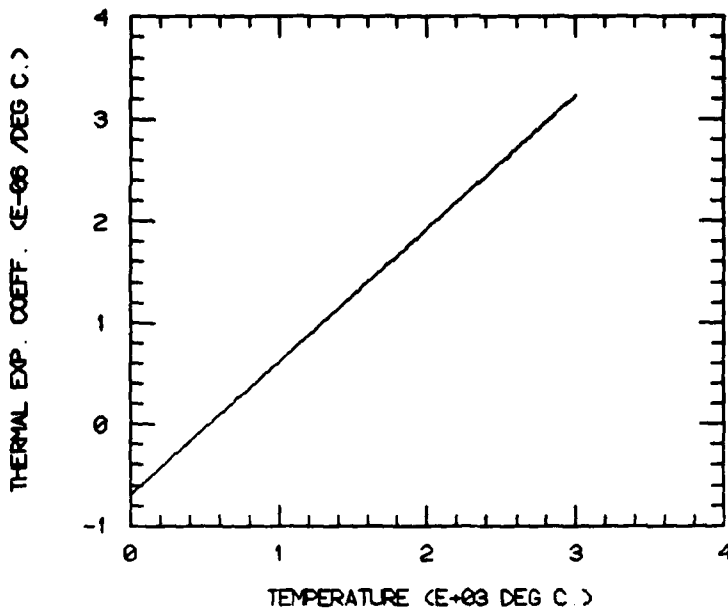


Figure 58. Longitudinal Thermal Expansion Coefficient for the Axial Sheath Model.

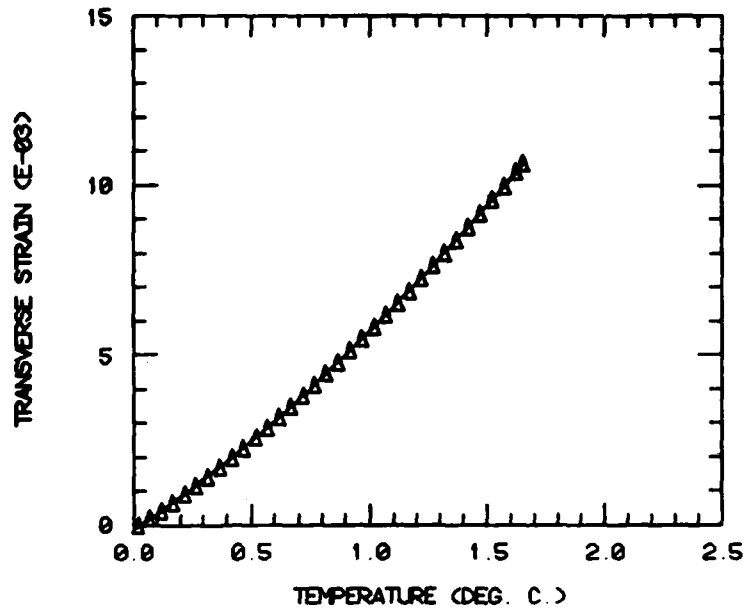


Figure 59. Transverse Thermal Strain for the Axial Sheath Model.

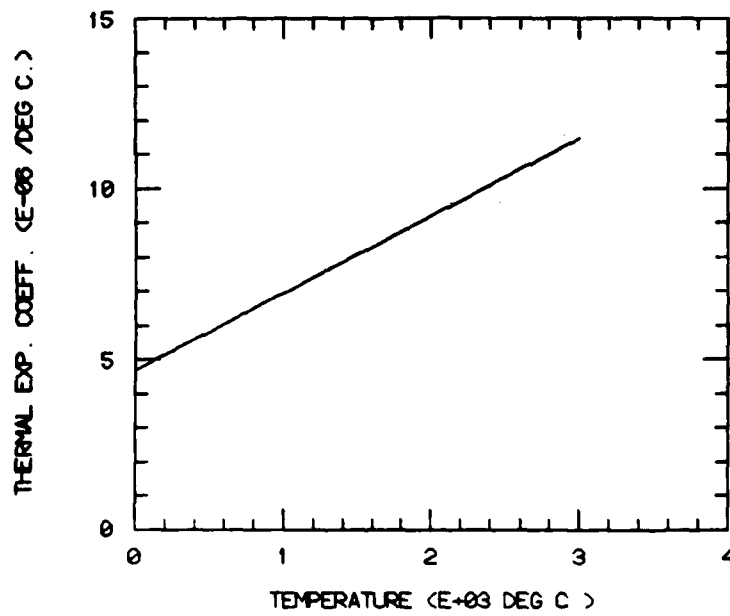


Figure 60. Transverse Thermal Expansion Coefficient for the Axial Sheath Model.

TABLE 8

Micromechanics Predicted Thermomechanical Properties for a Unidirectional Carbon-Carbon Fiber Bundle, Axial Sheath Model

Temperature (°C)	Tensile Moduli			Shear Moduli			Poisson's Ratios			
	E ₁₁ (GPa)	E ₁₁ (Msi)	E ₂₂ (GPa)	E ₂₂ (Msi)	G ₁₂ (GPa)	G ₁₂ (Msi)	G ₂₃ (GPa)	G ₂₃ (Msi)	ν ₁₂	ν ₂₃
21	274	39.7	7.7	1.11	5.4	0.78	3.0	0.43	0.23	0.24
815	283	41.1	8.2	1.19	5.7	0.83	3.2	0.46	0.22	0.14
1649	248	36.0	9.5	1.38	6.6	0.95	3.6	0.52	0.27	0.16

Temperature °C	Tensile Strengths			Shear Strengths		
	S ₁₁ ^{ut} (GPa)	S ₁₁ ^{ut} (ksi)	S ₂₂ ^{ut} (MPa)	S ₁₂ ^{us} (ksi)	S ₁₂ ^{us} (MPa)	S ₂₃ ^{us} (ksi)
21	1.12	162	27.8	4.04	10.5	1.53
815	0.93	135	37.2	5.40	10.1	1.47
1649	0.98	142	48.1	6.98	9.9	1.44

Thermal Expansion α₁₁ = -0.699 + 0.00131T

Coefficients (10⁻⁶/°C) α₂₂ = 4.704 + 0.00225T

demonstrated. The average longitudinal tensile modulus for fiber bundles tested during previous years of this present research was 287 GPa (41.6 Msi), with values ranging from a low of 179 GPa (25.9 Msi) to a high of 400 GPa (58.0 Msi). The 287 GPa (41.6 Msi) measured tensile modulus compares favorably with the room temperature 274 GPa (39.7 Msi) predicted tensile modulus using the axial sheath model. Unfortunately, transverse and shear test data for these fiber bundles were not available. Thus, longitudinal tension results were the only comparisons available for this present analytical work.

Properties listed in Tables 7 and 8, along with stress-strain plots shown in this present section of the report were used to define the fiber bundle material properties used in the three-dimensional minimechanics analysis. The minimechanics analysis data preparation and results are described in Section 5.

SECTION 5

MINIMECHANICS UNIT CELL ANALYSIS

5.1 Effective Material Properties

Inelastic material behavior is described within the three-dimensional finite element analysis by use of an effective stress-effective strain relation, previously described in Eqs. (4) and (5). The anisotropy parameters F, G, H, L, M, and N are calculated from Eq. (13) based on six "yield" stress values. The implication of this type of constitutive relation is that the six uniaxial stress-strain relations (four for a transversely isotropic material) can be described by a single effective stress-effective strain equation with proper choices for the anisotropy parameters. A discrepancy in this present minimechanics unit cell analysis was that the four micromechanics generated stress-strain relations could not be represented by a single effective stress-effective strain equation.

Micromechanics generated room temperature stress-strain data for the no-sheath fiber bundle model are plotted as effective stress versus effective strain in Figures 61 and 62. Figure 62 shows the initial portions of the curves plotted in Figure 61 on expanded scales. As can be easily seen in Figures 61 and 62, the four stress-strain plots representing longitudinal tension, transverse tension, longitudinal shear, and transverse shear do not merge into a single effective stress-effective strain plot. By appropriate selection of the "yield" strengths and therefore the anisotropy parameters, the initial slopes of the curves can be merged into one plot, as shown in Figure 62. However, variations in the anisotropy parameters do not change the basic shape of an individual stress-strain plot. Thus, the linear longitudinal tension plot remains linear. Nonlinear transverse tension, longitudinal shear, and transverse shear stress-strain plots remain nonlinear. It can be argued that an effective stress-effective strain constitutive relation should fail because nonlinearity exhibited by the stress-strain curves for individual loading modes occurs due to cracking. There is a need for further study of appropriate constitutive relations for all types of composite materials, as well as for carbon-carbon.

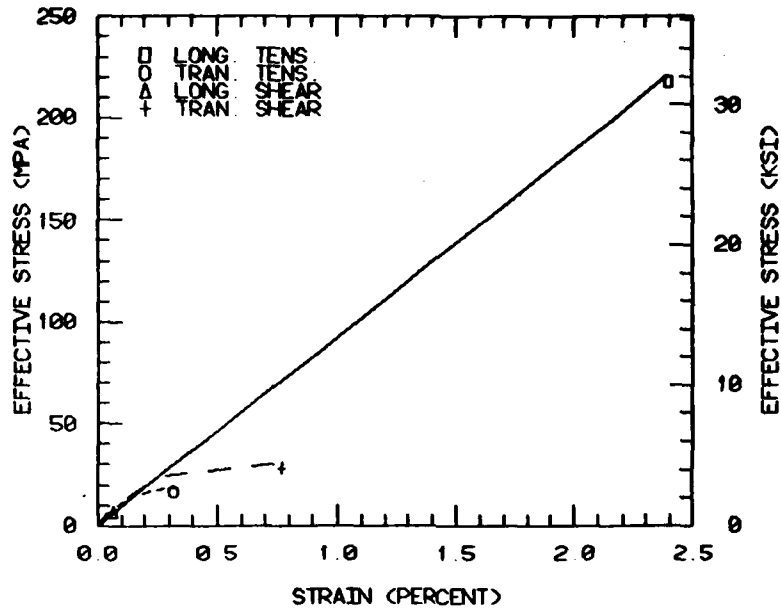


Figure 61. Effective Stress Versus Effective-Strain Plots for the Isotropic Carbon Matrix Fiber Bundle Model at Room Temperature.

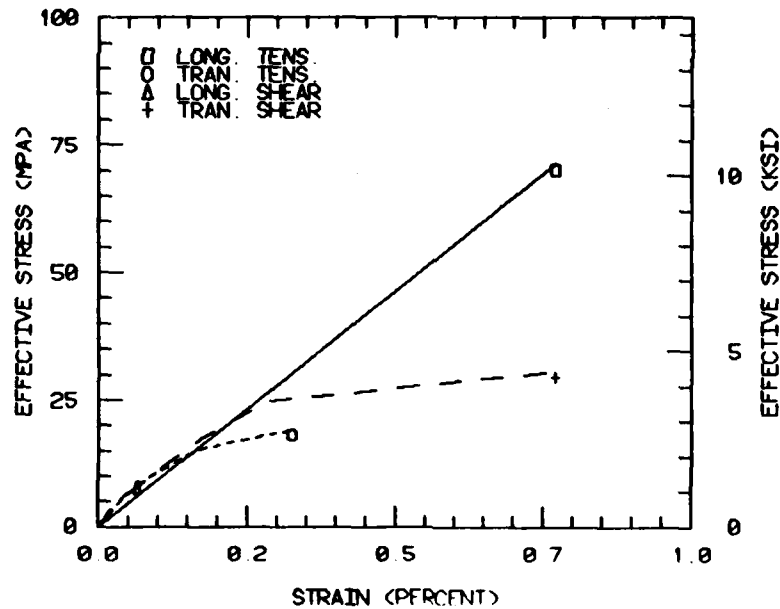


Figure 62. Initial Portions of the Effective Stress Versus Effective Strain Plots for the Isotropic Carbon Matrix Fiber Bundle Model at Room Temperature.

In the present analysis it was still possible to include the influence of nonlinear stress-strain behavior via an effective stress-effective strain constitutive relation. Fiber bundles in the unit cell micromechanics model, were oriented parallel to the x, y, and z coordinate directions, as previously shown in Figure 8. When the unit cell was subjected to a particular type of uniaxial applied stress, the stress state in an individual fiber bundle was dominated by one stress component. For example, when the unit cell model was subjected to an applied normal stress σ_x , the x-fiber bundle were primarily loaded in longitudinal tension. The y-fiber bundle and z-fiber bundle are primarily subjected to transverse tension. In order to include at least partial estimates of nonlinear fiber bundle behavior, two effective stress-effective strain equations were used to model fiber bundle constitutive behavior in the present analysis. One equation modeled axial response of the fiber bundle and one equation modeled transverse tension and shear behavior. Effective stress-effective strain constitutive plots used to represent the isotropic carbon matrix fiber bundle model, the fiber bundle with no sheath material, are shown in Figure 63.

Similar behavior is exhibited in results from the axial sheath fiber bundle micromechanics model, as plotted in Figures 64 and 65. Figure 65 shows initial portions of the plots shown in Figure 64 plotted on expanded scales. Again the four modeled loading cases could not be represented by a single effective stress-effective strain plot. Longitudinal tension stress-strain results for the axial sheath model are nonlinear, as shown in Figure 64, due to failure of the sheath material. However, effective stress-effective strain representation still requires use of two separate constitutive relations as is done for the isotropic carbon matrix fiber bundle. Effective stress-effective strain plots defining longitudinal and transverse behavior of the axial sheath fiber bundles are shown by the room temperature case in Figure 66.

Similar plots were constructed for the elevated temperature data generated using the micromechanics analysis. As the results were similar to the room temperature plots, the elevated temperature effective stress-effective strain plots were not included here. As for the room

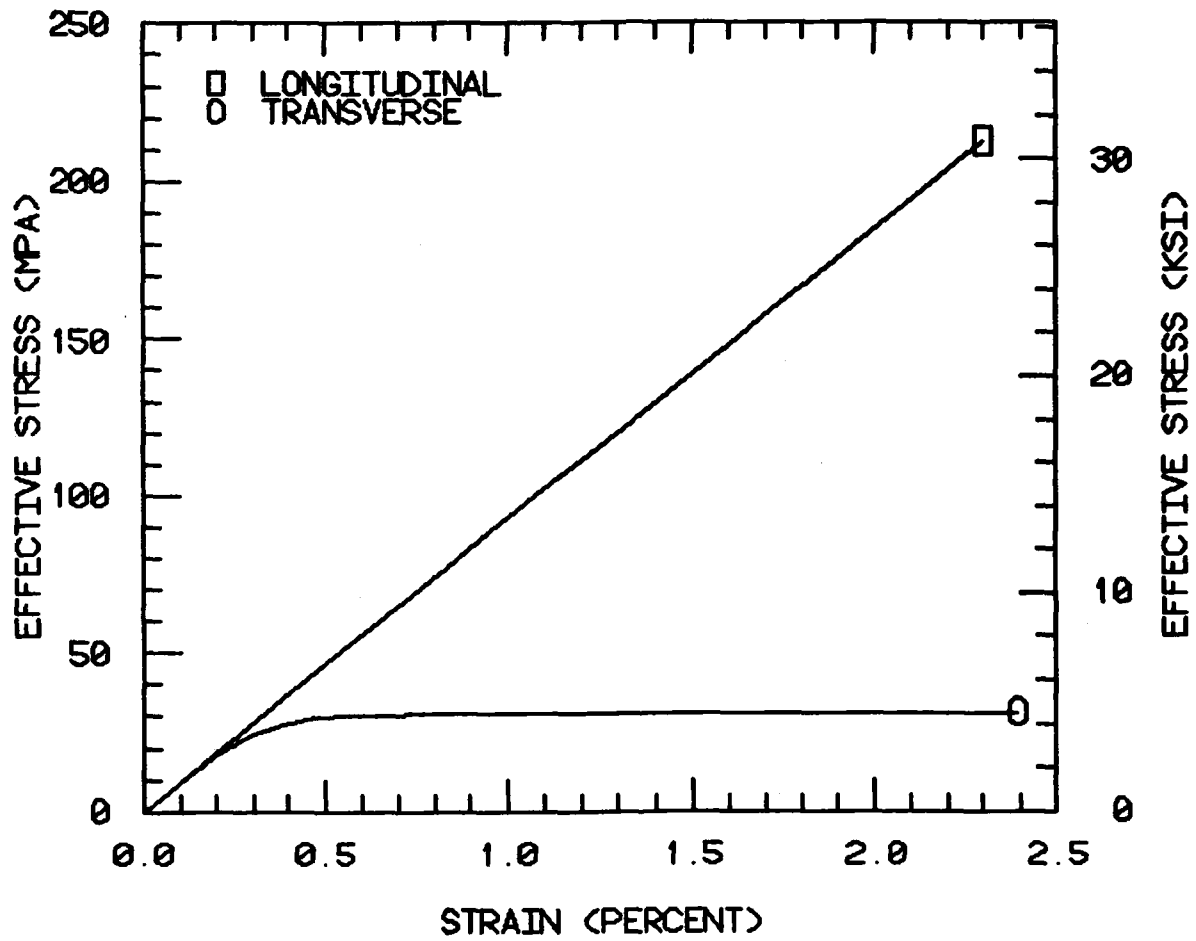


Figure 63. Effective Stress-Effective Strain Plots Used to Define Constitutive Behavior for the Isotropic Carbon Matrix Fiber Bundle at Room Temperature.

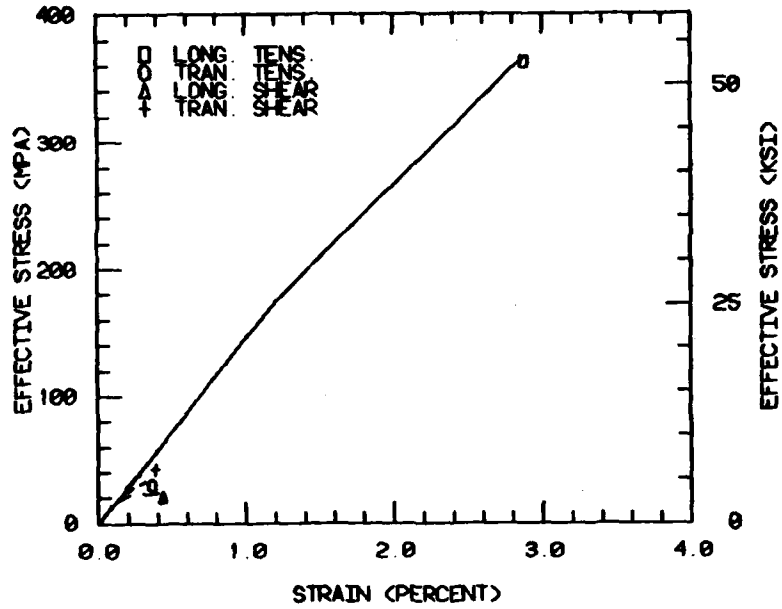


Figure 64. Effective Stress-Effective Strain Plots for the Axial Sheath Fiber Bundle Model at Room Temperature.

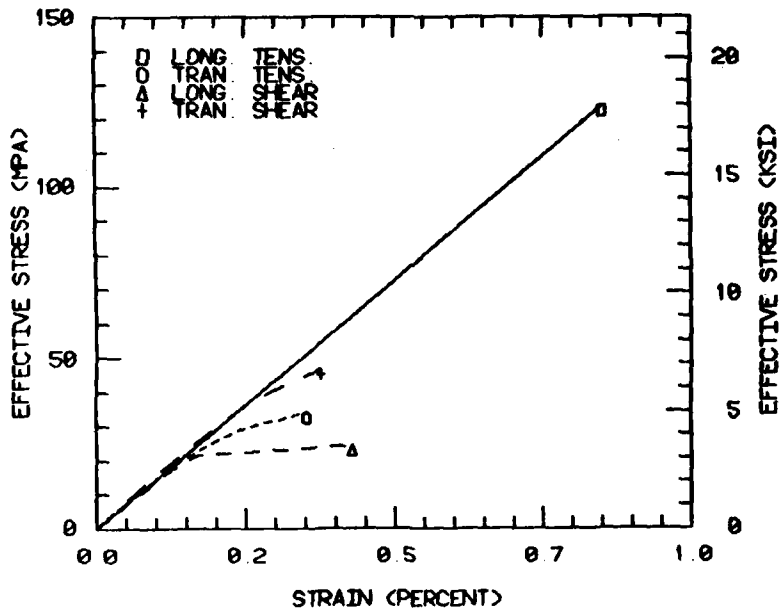


Figure 65. Initial Portions of the Effective Stress-Effective Strain Plots for the Axial Sheath Fiber Bundle Model at Room Temperature.

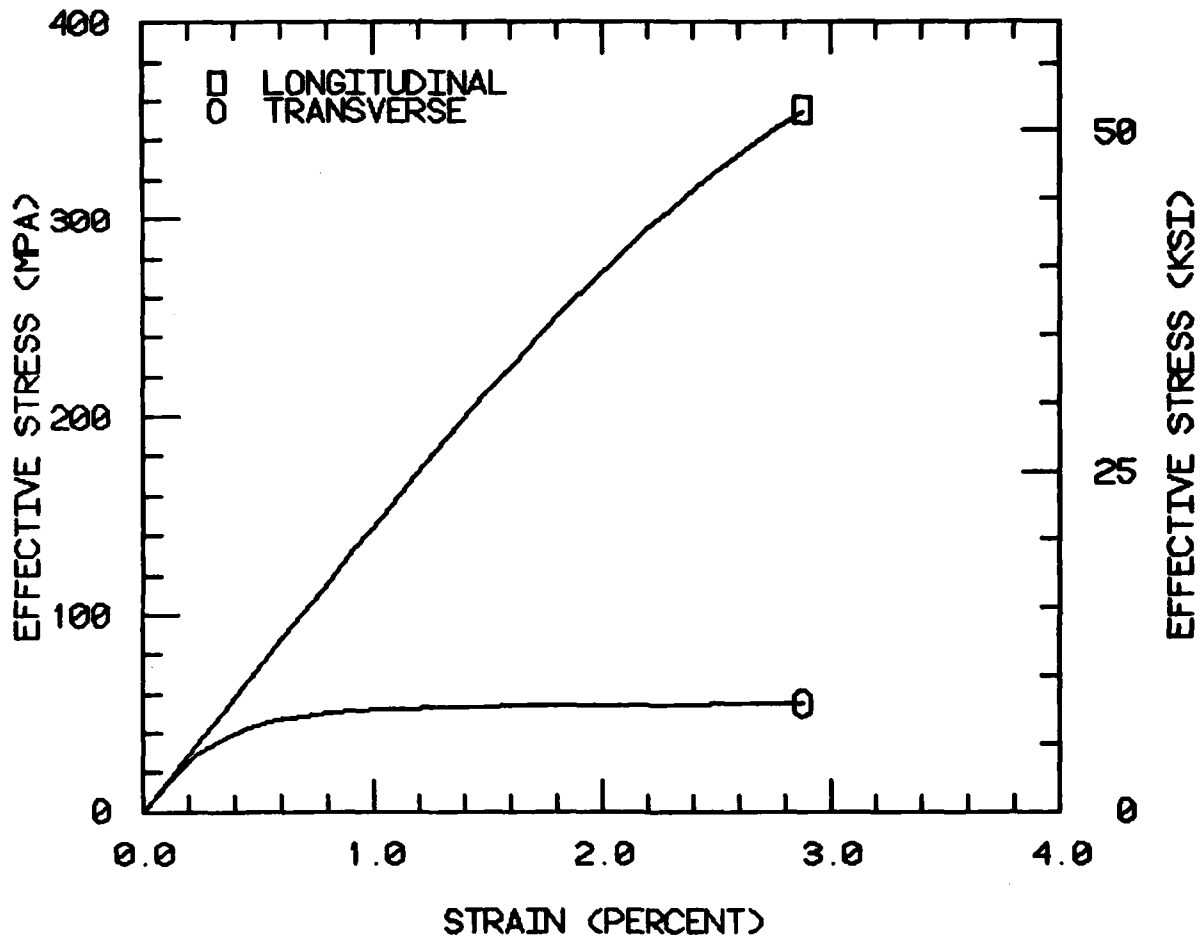


Figure 66. Effective Stress-Effective Strain Plots Used to Define Constitutive Behavior for the Axial Sheath Fiber Bundle at Room Temperature.

temperature results, representation of the effective stress-effective strain constitutive relations required two separate equations depending on the type of loading present. Stress values used to compute the anisotropy parameters defining effective stress-effective strain behavior at the three modeled temperatures are listed in Table 9 for both fiber bundle models. Note that shear values listed in Table 9 are greater than corresponding shear strengths listed in Tables 7 and 8. However, use of the predicted shear strength values produces no correlation of effective stress-effective strain behavior between the various loading modes.

Analytical weakness in modeling nonlinear fiber bundle stress-strain behavior pertains only to the nonlinear portions of constitutive behavior. Linear elastic functions in the three-dimensional finite element analysis worked well. An attempt was made to include nonlinear orthotropic material behavior into this micromechanics unit cell analysis, in order to include effects of microcracking within the fiber bundles.

Elastic constants calculated with the micromechanics analysis, listed in Table 7 and 8, were regression fit to polynomial functions of temperature in the same manner as constituent properties were entered into the generalized plane strain micromechanics analysis. Regression coefficients for the fiber bundle properties used in the present unit cell analysis are listed in Tables 10 and 11 for the no-sheath and axial sheath fiber bundle models, respectively. Two different sets of Richard-Blacklock parameters "yield" stress values are shown in Tables 10 and 11. The two sets of data represent two different effective stress-effective strain constitutive relations. The parameters marked as axial define the axial stress dominated effective constitutive relation. Parameters marked as transverse define transverse tension and shear dominated effective constitutive behavior. Stress values from Tables 10 and 11 were used to calculate the anisotropy parameters via equation (13).

Material properties written as polynomial equations in temperature in Table 10 and 11 define the fiber bundle properties used. Isotropic carbon material properties listed in Table 6 were used to represent carbon material within the unit cell interstitial matrix pockets.

TABLE 9

"Yield" Values Used to Calculate the Anisotropy Parameters F, G, H, L, M, and N
for the Fiber Bundle Constitutive Relations

Model	Temperature (°C)	Longitudinal Tension (MPa)	Longitudinal Tension (ksi)	Transverse Tension (MPa)	Transverse Tension (ksi)	Longitudinal Shear (MPa)	Longitudinal Shear (ksi)	Transverse Shear (MPa)	Transverse Shear (ksi)
<u>Isotropic Carbon Matrix Fiber Bundle Model</u>									
	R.T.	345	50.0	59	8.5	24	3.6	28	4.0
	815	345	50.0	69	10.0	28	4.0	27	3.9
	1649	345	50.0	76	11.0	31	4.5	26	3.7
<u>Axial Sheath Fiber Bundle Model</u>									
	R.T.	345	50.0	66	9.5	24	3.5	34	5.0
	815	345	50.0	72	10.5	26	3.8	34	5.0
	1649	345	50.0	79	11.5	28	4.0	34	5.0

TABLE 10

Thermomechanical Properties of the Isotropic Carbon Matrix Fiber
Bundle Model as Functions of Temperature ($^{\circ}\text{C}$)

$$\text{Property} = C_0 + C_1T + C_2T^2$$

Property	C_0	C_1	C_2
E_{11} (psi)	3.15×10^7	4.56×10^3	3.80×10^0
$E_{22} = E_{33}$ (psi)	7.72×10^5	-9.29×10	9.61×10^{-2}
$\nu_{12} = \nu_{13}$	2.11×10^{-1}	-6.28×10^{-5}	4.49×10^{-8}
ν_{23}	2.23×10^{-1}	-1.65×10^{-4}	7.66×10^{-8}
$G_{12} = G_{13}$ (psi)	6.41×10^5	-5.45×10^2	2.46×10^{-1}
α_{11} ($^{\circ}\text{C}^{-1}$)	-6.64×10^{-7}	1.27×10^{-9}	-
α_{22} ($^{\circ}\text{C}^{-1}$)	3.85×10^{-6}	2.33×10^{-9}	-
<u>Axial Properties</u>			
E_R (psi)	1.32×10^6	1.08×10^3	-3.83×10^{-1}
n	1.00×10	-	-
σ_0 (psi)	1.00×10^5	-	-
S_1	5.00×10^4		
$S_2 = S_3$ (psi)	8.45×10^3	2.24×10^0	-4.24×10^{-4}
$S_{12} = S_{13}$ (psi)	4.00×10^3	-1.94×10^{-1}	5.57×10^{-6}
S_{23} (psi)	3.59×10^3	4.55×10^{-1}	5.88×10^{-5}
<u>Transverse Properties</u>			
E_R (psi)	1.32×10^6	1.08×10^3	-3.83×10^{-1}
n	2.00×10^0		
σ_0 (psi)	4.92×10^3	3.87×10^0	-1.11×10^{-4}
S_1 (psi)	1.53×10^3	-9.95×10^{-2}	2.90×10^{-5}
$S_2 = S_3$ (psi)	1.68×10^3	2.84×10^0	-7.84×10^{-4}
$S_{12} = S_{13}$ (psi)	4.00×10^3	1.63×10^0	1.08×10^{-4}
S_{23} (psi)	2.38×10^5	1.03×10^2	-4.10×10^{-2}

TABLE 11

Thermomechanical Properties of the Axial Sheath Fiber Bundle Model
as Functions of Temperature ($^{\circ}\text{C}$)

$$\text{Property} = C_0 + C_1 T + C_2 T^2$$

Property	C_0	C_1	C_2
E_{11} (psi)	3.96×10^7	5.81×10^3	-4.84×10^0
$E_{22} = E_{33}$ (psi)	1.11×10^6	3.55×10	7.80×10^{-2}
$\nu_{12} = \nu_{13}$	2.31×10^{-1}	-4.98×10^{-5}	4.45×10^{-8}
ν_{23}	2.44×10^{-1}	-2.03×10^{-4}	9.21×10^{-8}
$G_{12} = G_{13}$ (psi)	7.79×10^5	2.14×10	4.97×10^{-2}
α_{11} ($^{\circ}\text{C}^{-1}$)	-7.01×10^{-7}	1.31×10^{-9}	-
α_{22} ($^{\circ}\text{C}^{-1}$)	4.69×10^{-6}	2.26×10^{-9}	-
<u>Axial Properties</u>			
E_R (psi)	2.10×10^6	9.68×10^2	-3.30×10^{-1}
n	3.0×10^0		
σ (psi)	6.98×10^4	9.68	-2.78×10^{-4}
S_1 (psi)	5.00×10^5	-	-
$S_2 = S_3$ (psi)	9.47×10^3	1.29	-3.71×10^{-5}
$S_{12} = S_{13}$ (psi)	5.0×10^3	-	-
S_{23} (psi)	3.49×10^3	3.22×10^{-1}	-9.27×10^{-6}
<u>Transverse Properties</u>			
E_R (psi)	2.10×10^6	9.68×10^2	-3.30×10^{-1}
n	2.0×10^0	-	-
σ_o (psi)	7.92×10^3	3.87×10^0	-1.11×10^{-4}
S_1 (psi)	1.63×10^5	-5.58×10	2.60×10^{-2}
$S_2 = S_3$ (psi)	4.76×10^2	6.63×10^{-1}	-2.06×10^{-4}
$S_{12} = S_{13}$ (psi)	4.76×10^2	6.63×10^{-1}	-2.06×10^{-4}
S_{23} (psi)	9.28×10^2	1.05	2.60×10^{-2}

5.2 Thermal Residual Stresses

An attempt was made in this analysis to model cracking within the unit cell due to processing-induced thermal residual stresses. During cooling, cracks developed at the interfaces between fiber bundles and at the interfaces between fiber bundles and the interstitial carbon matrix pockets. As cooling continued, these cracks extended, relieving a portion of the thermal residual stresses. The extent of such cracking has been studied in detail by Batdorf, et al. [74]. Recall that investigators at Materials Science Corporation included the effect of these cracks by use of a "unit cell efficiency" parameter which described the extent of such cracking [11-13].

It was hoped that the analysis used in this present work would be able to predict the extent of interfacial cracking. A unit cell efficiency parameter could then have been predicted, rather than back calculated from test data. Some minimal testing would still have been necessary to verify results, of course.

Unfortunately, the three-dimensional finite element analysis was, unable to completely model cracking in the present unit cell models. The unit cell model used in this work, previously shown in Figure 9, was relatively coarse in terms of the number of finite elements. The entire unit cell was represented by 425 nodes and only 64 elements. In regions of large stress gradients, a small number of elements made accurate representation of the stress state difficult. By using higher order elements, quadratic elements in this analysis, the accuracy of the analysis was improved. A more finely divided unit cell model would be desirable. However, the size of problem defined by the model of Figure 9 approached the maximum problem size which could be solved.

The computer program used in this analysis could only model crack propagation for one or two increments beyond crack initiation. Crack propagation by node division appeared to work correctly. However, after cracking at a few separated nodes in the unit cell models, problem solution became unstable and the analysis produced erroneous results. Difficulties were encountered in redistributing nodal forces during crack propagation in order to maintain equilibrium. Failure at a node in the coarse models required redistribution of larger force components. For these brittle materials, large redistribution forces produced

unstable crack extension and failure of the entire model. A finely divided model loaded in small incremental steps would be much more desirable than a coarse model loaded with large stress increments. Work is currently underway to make the three-dimensional finite element computer program more efficient in order to alleviate size and computation time restrictions.

Given limitations on problem size and computation time, it was not possible to calculate a unit cell efficiency parameter by modeling damage progression. Preliminary results indicated that extensive interfacial damage occurred due to fabrication-induced thermal residual stresses. This interfacial damage resulted in an essentially stress-free unit cell after temperature changes of only a few hundred degrees. Therefore, unit cell analysis for this present work was assumed to begin at a stress-free state for all modeled temperatures.

5.3 Thermoelastic Property Predictions

Elastic coefficients and stress-strain behavior for two carbon-carbon unit cell models were predicted by simulating σ_x and σ_z tensile normal stress loadings as well as τ_{xz} and τ_{xy} shear stress loadings. The same finite element mesh, previously shown in Figure 9, was used for both models. Only fiber bundle properties varied. Thus, three-dimensionally reinforced carbon-carbon unit cell properties were predicted using fiber bundles modeled with no oriented sheath around individual filaments, and for fiber bundles containing an oriented sheath material. As was done in the micromechanics analysis, mechanical loads were simulated at room temperature, 815°C and 1649°C.

Tensile normal stress-strain plots for the no sheath fiber bundle unit cell model are shown in Figures 67 and 68 for σ_x and σ_z applied stresses, respectively. Elevated temperature does not significantly affect stress-strain behavior of the no-sheath unit cell model for either σ_x or σ_z applied stress. Young's modulus in the x-direction is 42 GPa (6.1 Msi) at room temperature, 49 GPa (7.1 Msi) at 815°C, and 40 GPa (5.8 Msi) at 1649°C. Tensile moduli tend to increase with increasing temperature, then decrease at yet higher temperatures. This behavior is similar to that predicted for the x-direction fiber bundles themselves. Because x-direction stiffness is dominated by the x-direction fiber bundle, it is to be expected that such similar trends occur.

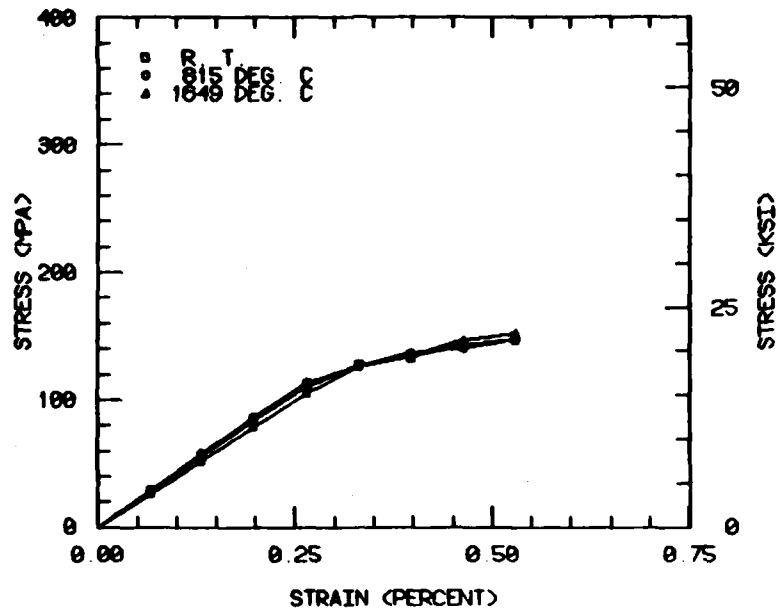


Figure 67. Tensile Stress-Strain Response for σ_x Loading of the No-Sheath Unit Cell Model.

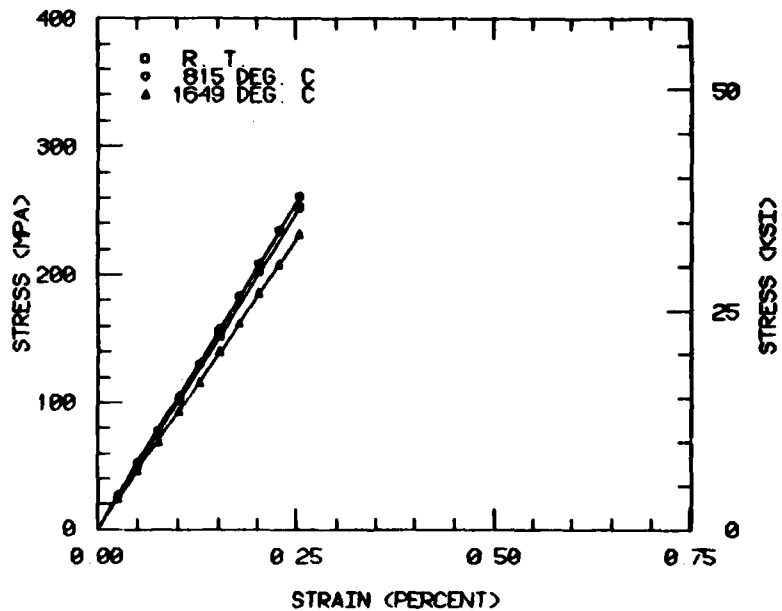


Figure 68. Tensile Stress-Strain Response for σ_2 Loading of the No-Sheath Unit Cell Model.

Elastic tensile moduli for the z-direction also increase, then decrease with progressively elevated temperatures. Tensile moduli in the z-direction for this no-sheath unit cell model are 100 GPa (14.5 Msi) at room temperature, 102 GPa (14.9 Msi) at 815°C, and 92 GPa (13.3 Msi) at 1649°C. Stiffness in the z-direction is dominated by the z-fiber bundle. Elastic moduli in the z-direction are approximately 2.3 times greater than x-direction elastic moduli, reflecting a higher proportion of graphite filaments oriented in the z-direction of the unit cell. In the actual FMI Billet No. 2696 modeled here, the ratio of z-oriented graphite filaments to x-oriented graphite filaments is 15000/6000, or 2.5/1.

Stress-strain plots for σ_x loading shown in Figure 67 are nonlinear but could be described as bilinear. Stress-strain plots for σ_z loading shown in Figure 68 are linear. This difference in shape between plots for the two applied stresses results from modeled nonlinearity in transverse constituent fiber bundle properties. For an x-direction applied stress, the z-fiber bundles were subjected to transverse tension and shear stresses. These transverse fiber bundles contributed to the stiffness of the unit cell until a "yield stress" for the most critical stress component was attained. At that point the analysis treated this transverse fiber bundle as an inelastic material obeying the transverse effective stress-effective strain relation shown in Figure 63. Transverse fiber bundles ceased to contribute to the stiffness of the unit cell, undergoing large increases in strain for only small increases in stress. Thus the x-direction fiber bundle had to withstand a proportionally larger share of the increasing applied stress with little load bearing contribution from transverse fiber bundles or interstitial matrix pockets. Recall that nonlinearity of the transverse fiber bundle properties was primarily caused by microcracking within the fiber bundles as predicted by the generalized plane strain micromechanics analysis. Therefore, even though the node separation technique was not currently being used to model gross damage propagation in the unit cell, damage occurring within constituent materials was included.

Stress-strain behavior in the z-direction is linear because transverse fiber bundles (the x- and y-fiber bundles) did not attain

stress values in excess of their respective yield strengths. Thus no changes in slope are apparent in the stress-strain plots of Figure 68.

Shear stress versus shear strain plots for the model are shown in Figures 69 and 70 for τ_{xz} and τ_{xy} applied shear stresses, respectively. Shear moduli tend to decrease as temperature increases from room temperature to 815°C. The G_{xz} shear moduli for shear stress-shear strain curves plotted in Figure 69 are 4.0 GPa (0.58 Msi) at room temperature and 2.8 GPa (0.41 Msi) at 815°C. The G_{xz} shear modulus at 1649°C increases to 3.2 GPa (0.46 ksi). This trend of decreasing then increasing shear modulus with increasing temperature reflects the shear stiffness behavior predicted for the no sheath fiber bundles as well as for the isotropic carbon matrix material. Shear stiffnesses for τ_{xy} applied stress exhibit similar behavior with temperature as do the G_{xz} shear moduli. At room temperature the G_{xy} shear modulus is 3.6 GPa (0.52 Msi), decreasing to 2.8 GPa (0.41 Msi) at 815°C, then increasing to 3.2 GPa (0.47 Msi) at 1649°C.

Elastic properties for the material tests simulated in Figures 67 through 69 are listed in Table 12. Poisson's ratios were calculated from strains predicted during modeling of σ_x and σ_z normal tensile applied stresses. Note that the Poisson's ratio values listed in Table 12 are quite low as compared to other engineering materials. These low lateral contractions reflect high lateral stiffnesses due to three-dimensional reinforcement of the unit cell and poor load transfer between constituent parts of the unit cell.

Tensile stress-strain predictions for the axial sheath unit cell model are plotted in Figures 71 and 72. Only small differences due to elevated temperature are apparent in the σ_x plots shown in Figure 71 or the σ_z plots shown in Figure 72. Both the σ_x and σ_z stress-strain plots exhibit nonlinear material behavior. This is due to modeled nonlinearity of transverse tensile and shear behavior for transverse oriented fiber bundles. However, σ_z stress-strain results also show an effect due to failure of the axial sheath, which was included as nonlinear behavior in the axial sheath fiber bundle tensile response, as previously shown in Figure 66.

Shear stress-shear strain plots for τ_{xz} and τ_{xy} applied stress are shown for the axial sheath unit cell model in Figures 73 and 74. Shear

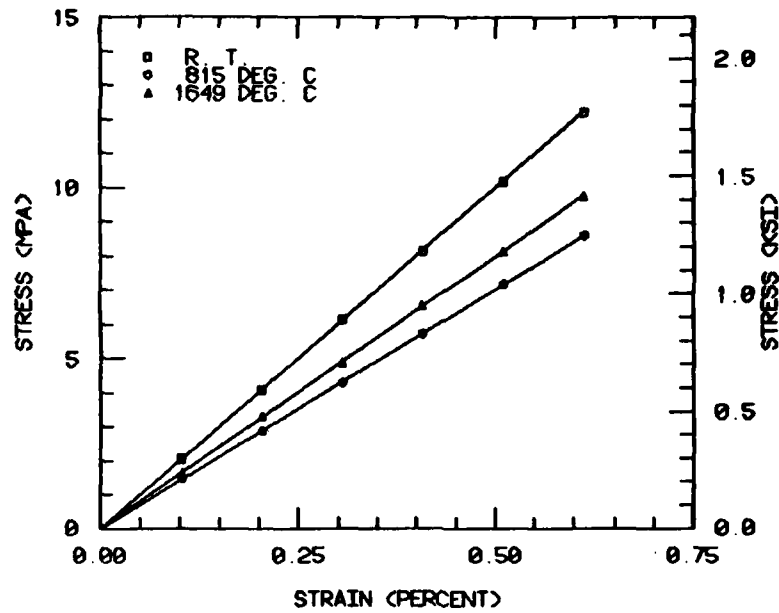


Figure 69. Shear Stress-Shear Strain Response for τ_{xz} Loading of the No-Sheath Unit Cell Model.

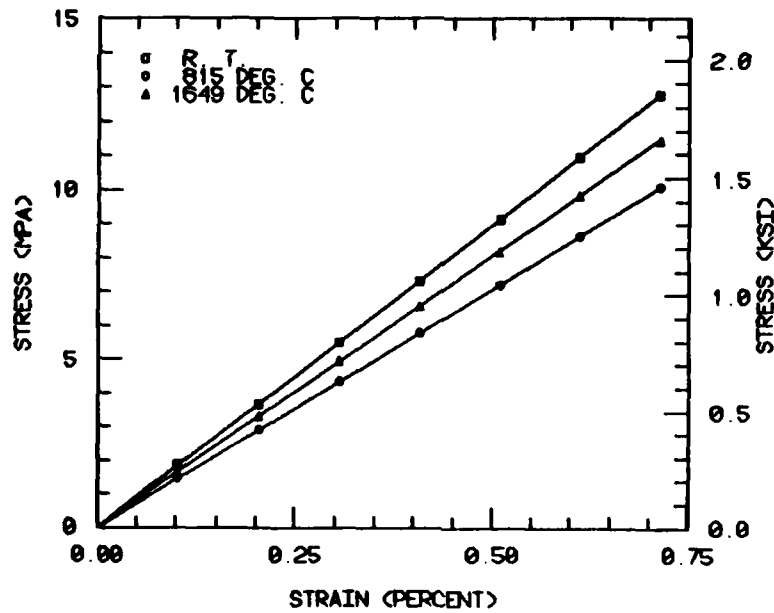


Figure 70. Shear Stress-Shear Strain Response for τ_{xy} Loading of the No-Sheath Unit Cell Model.

TABLE 12

Minimechanics Predicted Thermomechanical Properties for the No-Sheath
Unit Cell Model

Temperatures (°C)	E_{xx} (GPa)(Msi)	E_{zz} (GPa)(Msi)	G_{xz} (GPa)(Msi)	G_{xy} (GPa)(Msi)	ν_{xy}	ν_{xz}	$\nu_{zx} - \nu_{zy}$
Room Temperature	42.2 6.12	100 14.5	4.0 0.58	3.6 0.52	0.031	0.013	0.031
815	48.8 7.08	102 14.9	2.8 0.41	2.8 0.41	0.023	0.011	0.026
1649	39.6 5.75	92 13.3	3.2 0.46	3.2 0.47	0.035	0.017	0.039

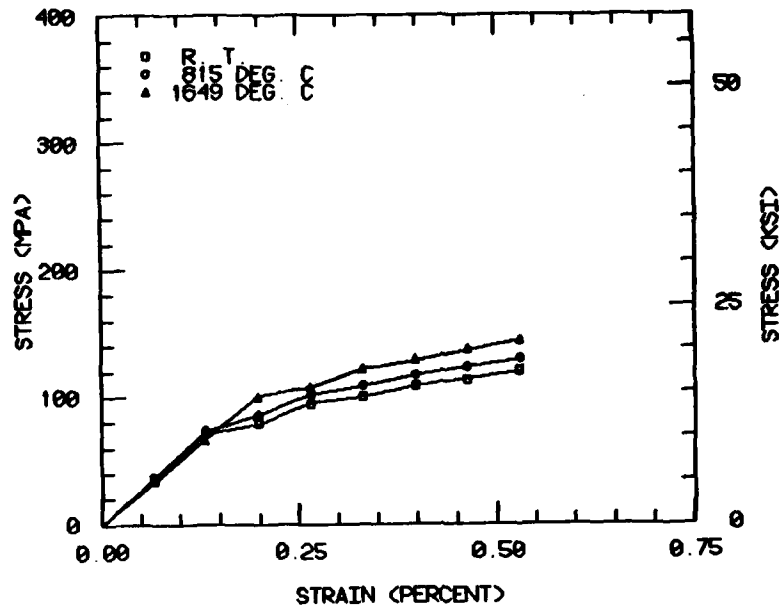


Figure 71. Tensile Stress-Strain Response for σ_x Loading of the Axial Sheath Unit Cell Model.

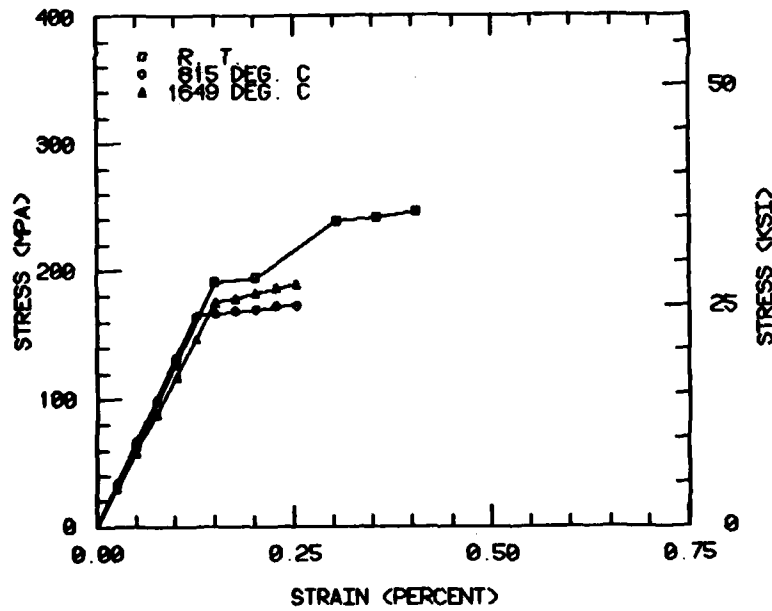


Figure 72. Tensile Stress-Strain Response for σ_z Loading of the Axial Sheath Unit Cell Model.

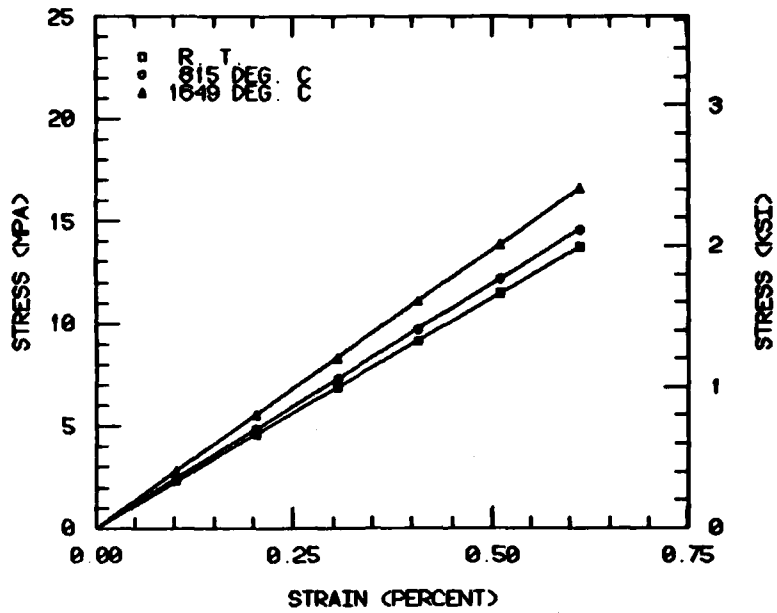


Figure 73. Shear Stress-Shear Strain Response for τ_{xz} Loading of the Axial Sheath Unit Cell Model.

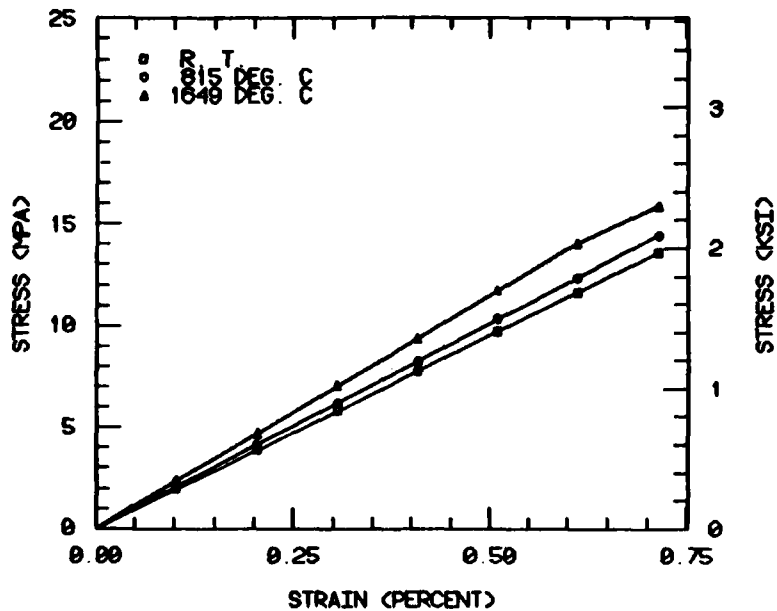


Figure 74. Shear Stress-Shear Strain Response for τ_{xy} Loading of the Axial Sheath Unit Cell Model.

moduli for both applied shear stresses tend to increase with increasing temperature, as reflected in Figures 73 and 74.

Elastic coefficients predicted for the carbon-carbon unit cell using axial sheath fiber bundle properties are listed in Table 13. Poisson's ratio values are again quite low, similar to the no-sheath unit cell results.

5.4 Comparison of Predicted Properties

Room temperature σ_x and σ_z normal stress-strain results for the no-sheath and axial sheath carbon-carbon unit cell models are plotted together in Figures 75 and 76. The curves marked with squares show results using the no-sheath fiber bundle properties, i.e., a fiber bundle containing only isotropic carbon as a matrix material. The curves marked with circles show results using the axial sheath fiber bundle properties. As can be seen in Figure 75, the axial sheath material is initially stiffer than the material containing no oriented sheath, as would be expected. The predicted no-sheath unit cell tensile modulus E_x is 42 GPa (6.1 Msi), and 53 GPa (7.7 Msi) for the axial sheath model, as listed in Tables 12 and 13. The greater tensile modulus of the axial sheath unit cell is due to the stiffening effect of sheath material oriented in the x-direction of the unit cell. Note the sharp slope change in the axial sheath model stress-strain curve which takes place when the x-direction sheath material fails. In the no sheath case, slope changes are more gradual because stiffness changes (cracking) in the y- and z-direction fiber bundles occur less abruptly. These transverse property changes also have less influence on the overall unit cell stress-strain response. Both stress-strain curves shown in Figure 75 become relatively flat at approximately 137 MPa (20 ksi), with the no-sheath material reaching a slightly greater stress than the axial sheath material. From the shapes of the curves it can be seen that an x-direction ultimate tensile strength estimate for either carbon-carbon unit cell model must on the order of 137 MPa (20 ksi).

Room temperatures tensile tests performed on FMI Billet No. 2696 during previous years of this research study showed an average x-direction strength of 128 GPa (18.5 ksi) and an x-direction elastic modulus of 47 GPa (6.8 Msi) [2]. Results shown in Tables 12 and 13 and

TABLE 13

Minimechanics Predicted Thermomechanical Properties for the Axial Sheath
Unit Cell Model

Temperatures (°C)	E_{xx} (GPa)(Msi)	E_{zz} (GPa)(Msi)	G_{xz} (GPa)(Msi)	G_{xy} (GPa)(Msi)	ν_{xy}	ν_{xz}	$\nu_{zx} = \nu_{zy}$
Room Temperature	53.3 7.73	125 18.2	4.5 0.65	3.8 0.55	0.024	0.016	0.026
815	55.2 8.01	130 18.8	4.8 0.69	4.1 0.59	0.028	0.014	0.032
1649	50.5 7.33	115 16.7	5.4 0.79	4.6 0.67	0.042	0.022	0.049

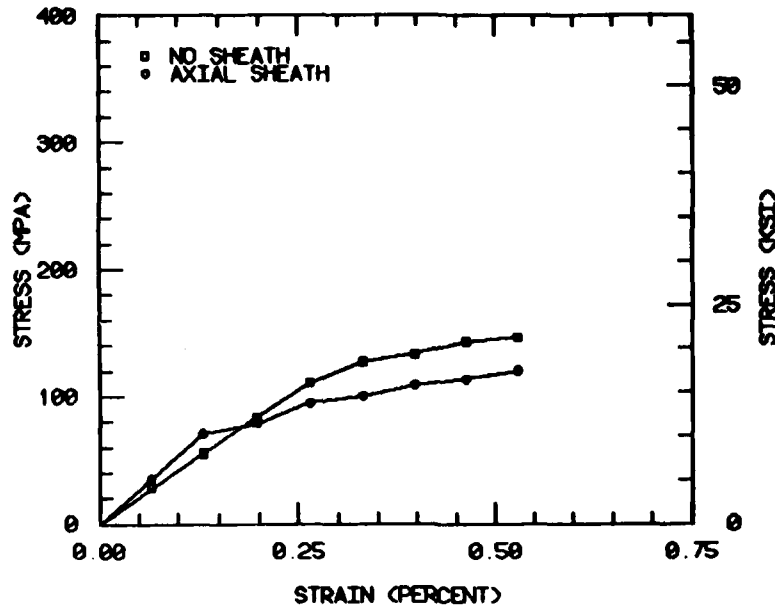


Figure 75. Room Temperature σ_x Tensile Stress-Strain Response for the No-Sheath Unit Cell and the Axial Sheath Unit Cell Models.

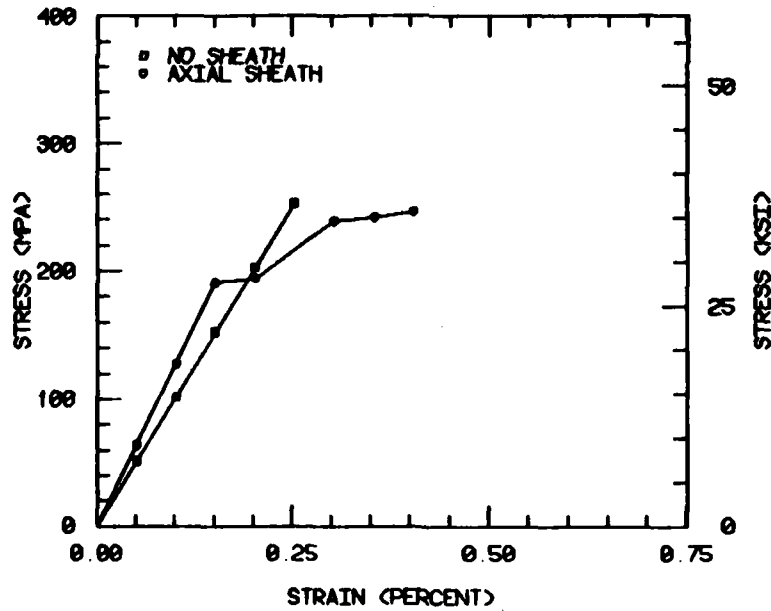


Figure 76. Room Temperature σ_z Tensile Stress-Strain Response for the No-Sheath Unit Cell and the Axial Sheath Unit Cell Models.

in Figure 75 compare favorably with the measurements reported in Reference [2].

A comparison of predicted room temperature σ_z tensile stress-strain behavior for unit cells using the two different fiber bundles is shown in Figure 76. As for the x-direction tensile stress results, the axial sheath unit cell model is axially stiffer than the no-sheath model, i.e., 125 GPa (18.2 Msi) as compared to 100 GPa (14.5 Msi). A major difference in results obtained for the two models is that the no-sheath curve is linear and the curve predicted using fiber bundles with an axially oriented sheath is nonlinear. For the no sheath case, transverse fiber bundles and interstitial matrix regions are not stressed beyond their respective "yield" values, therefore no nonlinear material behavior is exhibited. The linear elastic no sheath z-direction fiber bundle totally dominates σ_z tensile stress-strain behavior. For the axial sheath unit cell model, stress-strain behavior is also dominated by the z-direction fiber bundle. However, longitudinal stress-strain response of axial sheath fiber bundles is nonlinear (bilinear) due to failure of the sheath.

The average tensile modulus in the z-direction measured during previous experimental work was 123 GPa (17.8 Msi) and the average strength was 163 MPa (23.6 ksi) [2]. This measured tensile modulus most closely corresponds to the 125 GPa (18.2 Msi) room temperature z-direction tensile modulus predicted for the axial sheath unit cell model. At approximately 207 GPa (30 ksi), the axial sheath model results show larger inelastic strains, flattening the curve plotted in Figure 76. An ultimate strength for this model must then also be approximately 207 GPa (30 ksi), which compares reasonably well with the 163 GPa (23.6 ksi) average measured z-direction tensile strength reported in Reference [2].

Room temperature τ_{xz} and τ_{xy} shear stress-shear strain results are plotted for the no-sheath and axial sheath unit cell models in Figures 77 and 78, respectively. For both applied shear stress loadings, the axial sheath model is slightly stiffer than the no-sheath model, although the results are quite similar.

Both unit cell models predicted shear moduli that were somewhat greater than shear moduli measured during previous experimental work.

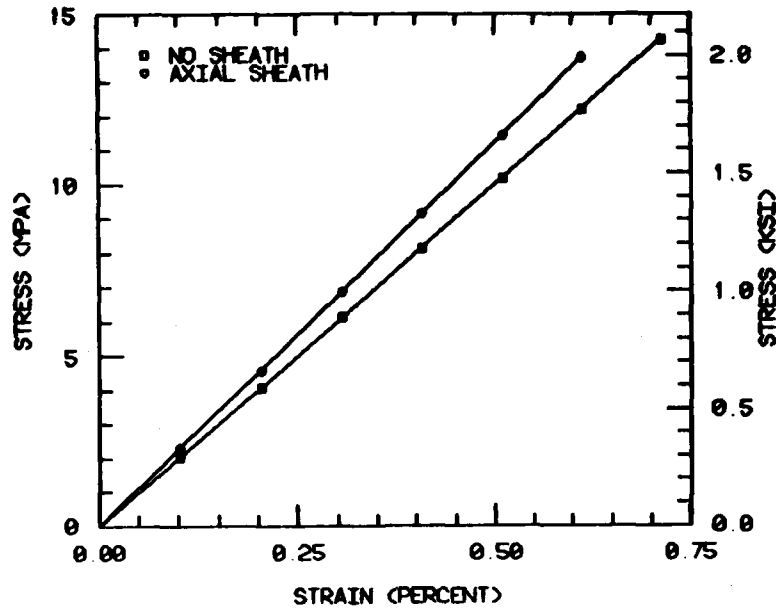


Figure 77. Room Temperature τ_{xz} Shear Stress-Shear Strain Response for the No-Sheath Unit Cell and the Axial Sheath Unit Cell Models.

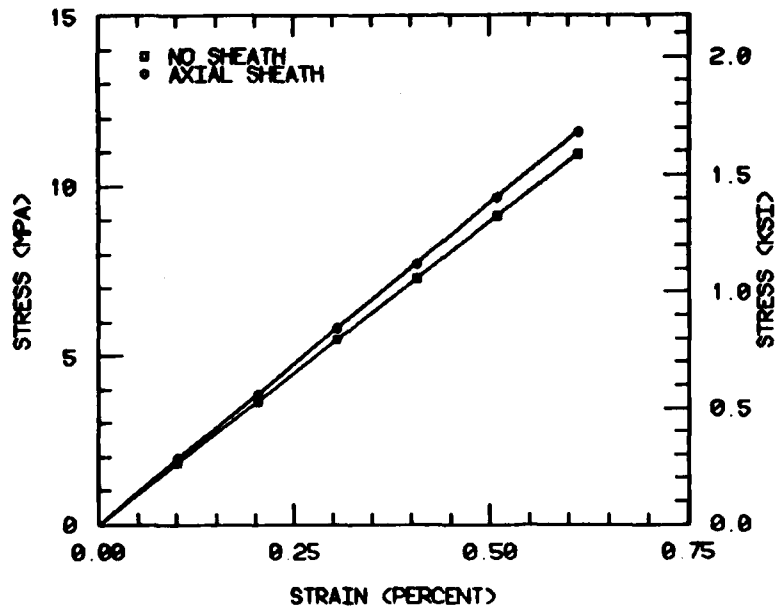


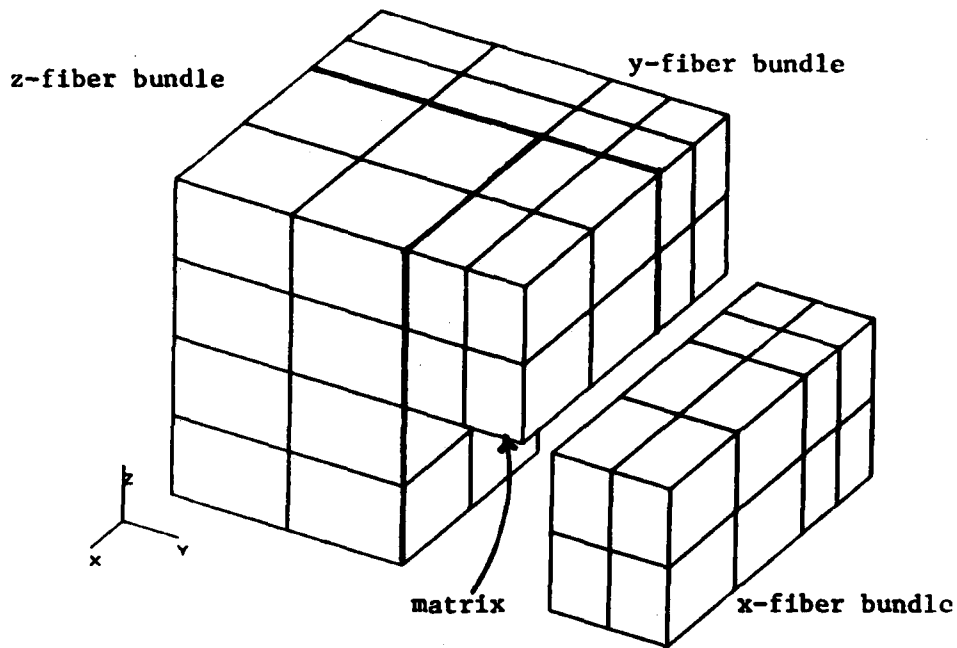
Figure 78. Room Temperature τ_{xy} Shear Stress-Shear Strain Response for the No-Sheath Unit Cell and the Axial Sheath Unit Cell Models.

Shear stiffnesses G_{xz} of 4.0 GPa (0.58 Msi) and 4.5 GPa (0.65 Msi) were predicted for the no-sheath and axial sheath unit cell models, respectively. Room temperature G_{xy} predicted shear moduli were 3.6 GPa (0.52 Msi) and 3.8 GPa (0.55 Msi), as listed in Tables 12 and 13. Average shear moduli reported in References [2,3] as measured with the Iosipescu shear test method were 2.2 GPa (0.32 Msi) for G_{xz} and 2.6 GPa (0.38 Msi) for G_{xy} . Average shear strengths of 16 MPa (2.3 ksi) and 15 MPa (2.2 ksi) for τ_{xz} and τ_{yz} applied stresses were also reported.

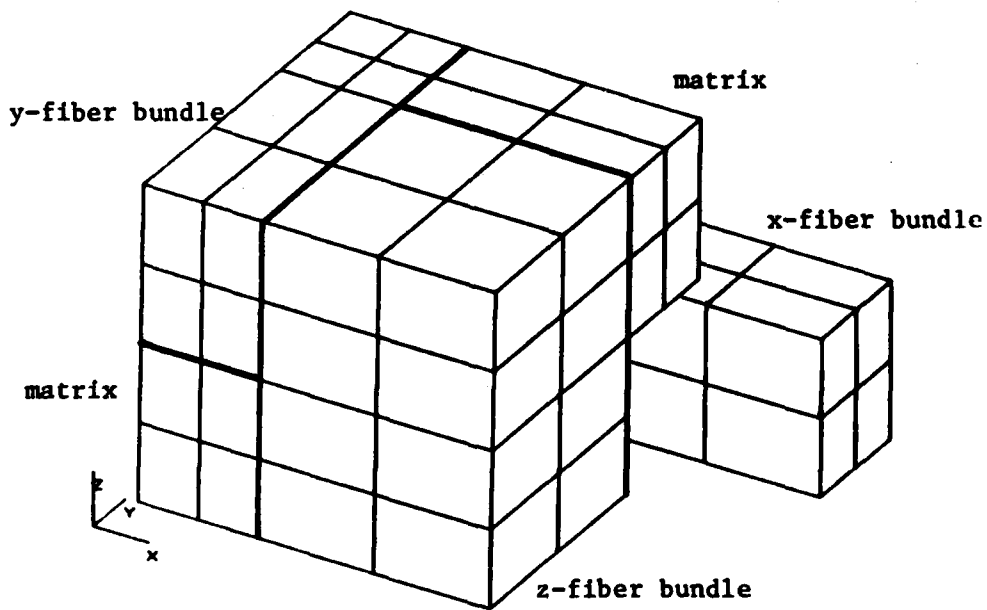
Shear behavior of carbon-carbon materials is dominated by cracking which occurs at the various interfaces within the carbon-carbon unit cell. Because these interfaces were assumed to be initially intact in the present analysis, predicted shear stiffnesses tended to be greater than actual measured values. An attempt to model interface damage in this present work was unsuccessful, for reasons previously described. Steps are currently being taken to improve interfacial damage propagation modeling.

It was possible to use the present analysis to estimate damage initiation within the carbon-carbon unit cell. Crack initiation functions within the computer program worked well. Difficulties existed in the automated crack propagation portions of the program. By use of interactive graphics, a carbon-carbon unit cell model can be "taken apart", as shown in Figure 79, and stresses at the various constituent interfaces examined. In Figure 79a, a unit cell corresponding to the original model of Figure 8 is shown. An x-direction fiber bundle is separated from the unit cell. The model is then rotated to permit viewing of the x-direction fiber bundle interface surfaces, as shown in Figure 79b. All portions of the unit cell except the x-direction fiber bundle are then erased. This interactive graphics software is called PATRAN, marketed by PDA Engineering, Santa Ana, California.

Shear stress contours are plotted on the internal surfaces of this no-sheath x-direction fiber bundle in Figure 80. These τ_{xy} shear stress contours have been normalized by dividing by the $\bar{\tau}_{xy}$ applied shear stress value. As can be seen in Figure 80, shear stresses are relatively uniform within the unit cell. The maximum shear stress contour shown is only 10 percent greater than the applied shear stress. Therefore, overall material shear strength is basically governed by the shear



a) Fiber Bundle Separated



b) Model Rotated to View Internal Surfaces

Figure 79. Three-Dimensionally Woven Carbon-Carbon Unit Cell Model with the x-Direction Fiber Bundle Removed.

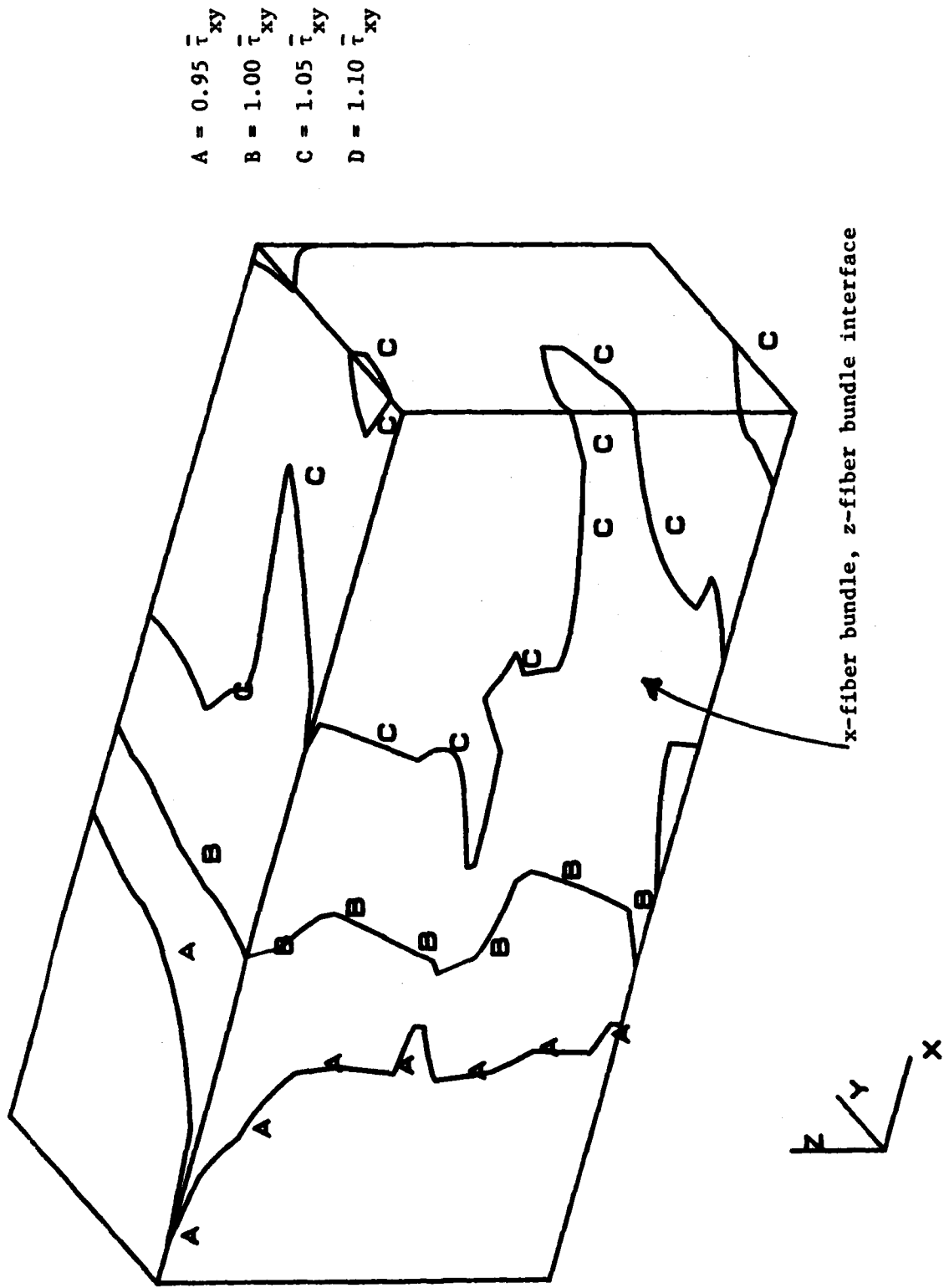


Figure 80. Normalized $\tau_{xy}/\bar{\tau}_{xy}$ Shear Stress Contours in an x-Direction Fiber Bundle from the No. Sheath Unit Cell Model.

strengths of the component parts of the unit cell. Fiber bundle shear strengths predicted using the micromechanics analysis ranged from 3 MPa (0.5 ksi) to 12 MPa (1.8 ksi). These values were in good agreement with measured shear strengths reported in References [2,3]. Because crack propagation did not function properly in the present computer program, post interface shear failure loading of the models was not attempted. Therefore, additional shear load bearing capability due to reorientation of fiber bundles was not included in the analysis.

Overall, the three-dimensional unit cell analysis predicted tensile elastic constants very well, and did an adequate job of predicting elastic shear constants. This finite element analysis differed from linearly elastic analyses in that it was capable of modeling inelastic material behavior and could therefore predict the entire stress-strain response of any modeled composite material for any modeled loading or environment.

The importance of including the presence of oriented matrix material within graphite fiber bundles was again demonstrated. This oriented sheath material is responsible for increased stiffness in the composite. It also contributes to the nonlinear (bimodular) tensile behavior exhibited by carbon-carbon. The fiber bundle-fiber bundle and fiber bundle-interstitial matrix pocket interfaces were also again shown to be important. Unfortunately, computational difficulties made adequate modeling of these interfaces impossible. Presently planned improvements of the computer program, coupled with advances in the size and speed of computer hardware, will make modeling damage propagation feasible.

SECTION 6

SUMMARY AND CONCLUSIONS

The objective of this research program was to develop a combined micromechanics and minimechanics analysis to predict the thermomechanical material properties and stress-strain behavior for three-dimensionally woven carbon-carbon composite materials. A generalized plane strain finite element micromechanics analysis was successfully used to predict thermomechanical behavior of unidirectional carbon-carbon fiber bundles. Two different fiber bundle models were analyzed to determine the influence on fiber bundle properties of an axially oriented orthotropic matrix sheath surrounding individual graphite fibers. This analysis included the influence of nonlinear, temperature-dependent material behavior. Results also included the effects of microcracking damage progression within the fiber bundles. Two sets of fiber bundle properties were then used to predict uniaxial tensile and shear properties for a three-dimensional cartesian-weave carbon-carbon composite. Predicted material properties were compared with room temperature experimental data generated during previous years of this research.

The presence of an oriented axial sheath around individual graphite filaments within fiber bundles was again shown to be an important factor influencing the bulk material response of carbon-carbon composites. This axial sheath provided increased fiber bundle stiffness, thereby increasing the predicted bulk stiffness of the carbon-carbon unit cell. Tensile failure of the sheath also contributed to predicted nonlinear stress-strain behavior in the woven carbon-carbon material.

Damage propagation was also shown to strongly influence mechanical properties. At the micromechanics scale, damage propagation was responsible for a major portion of the predicted nonlinear stress-strain behavior, especially in shear. Unfortunately, computational problems prevented complete damage propagation modeling during the unit cell analysis. Crack initiation models did demonstrate the importance of including this behavior in any analysis of carbon-carbon. With presently continuing improvements to the computer program, such crack propagation modeling will be feasible.

One difficulty encountered during this present investigation was a lack of constituent material properties data. Properties for bulk ATJ-S graphite were used to estimate matrix carbon material behavior. It is unlikely that matrix carbon within carbon-carbon fiber bundles has the same properties at this micromechanics scale as bulk ATJ-S. However, direct determination of in-situ micromechanical matrix carbon properties is difficult.

Overall, the objectives of this program were attained. Many problems still exist with regard to modeling carbon-carbon materials. However, the analytical tools developed here are equally applicable to the study of many other composite materials, including polymer matrix and ceramic matrix composite materials. Although the present research program is concluded, work to further refine the analytical techniques developed during the program is continuing. Analytical and experimental efforts to further explore inelastic constitutive behavior of composite materials will continue also.

REFERENCES

1. Walrath, D. E. and Adams, D. F., "Damage Mechanisms/Failure Mechanics of Carbon-Carbon Composite Materials," Report No. UWME-DR-904-101-1, Department of Mechanical Engineering, University of Wyoming, September 1979.
2. Walrath, D. E. and Adams, D. F., "Test Methods Development for 3D Cylindrical-Weave Carbon-Carbon Composite Materials," Report No. UWME-DR-104-104-1, Department of Mechanical Engineering, University of Wyoming, September 1981.
3. Odom, E. M. and Adams, D. F., "Axial Test Methods Development for 3D Cylindrical-Weave Carbon-Carbon Composite Materials," Report No. UWME-DR-301-104-1, Department of Mechanical Engineering, University of Wyoming, November 1983.
4. Schmidt, D. L., "Carbon/Carbon Composites," SAMPE Journal, Vol. 8, May/June 1972, pp. 9-19.
5. Butler, B. L., Northrop, D. A., and Guess, T. R., "Interfaces in Carbon Fiber/Pyrolytic-Carbon Matrix Composites," Journal of Adhesion, Vol. 5, pp. 161-178, 1973.
6. Perry, J. L., Miller, R. L., and Adams, D. F., "Exploratory Developments Leading to Improved Carbon-Carbon Composite Materials," Final Report, Philco-Ford Corporation, Aeronutronic Division, Newport Beach, California, June 1973.
7. Evangelides, J. S., "Microstructural Characteristic of Crack Propagation and Analytical Modeling of Carbon-Carbon Composites," Proceedings of the U.S. Army Symposium on Solid Mechanics. Composite Materials: The Influence of Mechanics of Failure on Design, Watertown, MA, September 1976.
8. Evangelides, J. S., Chang, D. J., Gyetvey, S. R., "Fiber-Matrix Thermal and Mechanical Properties," Report for the Office of Naval Research, December 1980.
9. Evans, A. G. and Adler, W. F., "Structural Degradation in Fiber Composites by Kinking," Report No. AD/A-042 528, Rockwell International Science Center, Thousand Oaks, California, May 1972.
10. Jortner, J., "The Effects of Weak Interfaces on Thermostructural Behavior of Carbon-Carbon Composites," Report JR&E 8526, Jortner Research and Engineering, Inc., March 1985.
11. Kibler, J. J. and Chatterjee, S. N., "Development of a Minimechanics Model for 3-D Carbon-Carbon Materials," Report No. TFR 7510, Materials Sciences Corporation, July 1975.

12. Chatterjee, S. N., McLaughlin, P. V., and Kibler, J. J., "Development of an Analytical Model for Carbon/Carbon Composite Materials, Phase I, Failure Mechanisms," Report TFR/604/1142, Materials Science Corporation, August 1976.
13. Kibler, J. J., Rosen, B. W., and Chatterjee, S. N., "Development of an Analytical Model for Carbon/Carbon Composite Materials, Phase II: Materials Design," Report No. TFR/703/1142, Materials Science Corporation, March 1977.
14. Hashin, Z., and Rosen, B. W., "The Elastic Moduli of Fiber Reinforced Materials," Journal of Applied Mechanics, Vol. 31, 1964, p. 223.
15. Kibler, J. J. and Buesking, K., "Nosetip and Rocket Nozzle Carbon/Carbon Material Evaluations," Report No. TFR/809/1144, Materials Science Corporation, June 1978.
16. Buesking, K., Kibler, J. J., and Rubinsky, J., "Strategic Missile Materials Technology (SMMT) Program, Nozzle Material Design Study," Report No. MSC TFR/1009/1406, Material Sciences Corporation, August 1979.
17. Eitman, D. A., White, M. J., and Stover, E., R., "Analytical Processing for Improved Composites (APIC), Volume 1, Processing and Characterization," Report No. AFWAL-TR-80-4147, Volume 1, Science Applications, Inc., October 1980.
18. Loomis, W. C., Tso, F. K., Dirling, Jr., R. B., and Heighland, C. N., "Analytical Processing for Improved Composites (APIC), Volume 2, Analytical Modeling," Report No. AFWAL-TR-80-4147 Volume 2, Science Applications, Inc., October 1980.
19. Loomis, W. C., Tso, F. K., Dirling, Jr., R. B., and Hieghtland, C. N., "Analytical Processing for Improved Composites (APIC)," Report No. AFWAL-TR-81-4082, Science Applications, Inc., August 1981.
20. Jortner, J., "Anomalies in 3D Cylindrical Carbon-Carbon Composites," Chemical Propulsion Information Agency Publication No. 324, Johns Hopkins University Applied Physics Laboratory, August 1980.
21. Jortner, J., "Effects of Anomalies on Thermostructural Behavior of 3D Carbon-Carbon Composites," Report No. AFWAL-TR-82-4118, Science Applications, Inc., Irvine, California, October 1982.
22. Pardoen, G. C., "Improved Structural Analysis Techniques for Orthogonal Weave Carbon-Carbon Materials," AIAA Journal, Vol. 13, No. 33, June 1974, pp. 756-761.
23. Pardoen, G. C., "Asymmetric Stress Analysis of Axisymmetric Solids with Anisotropic Material Properties," AIAA Journal, Volume 15, No. 10, 1978, pp. 1498-1500.

24. Geiler, D. E., "Thermostructural Analysis of Three-Dimensionally, Orthogonally Reinforced Carbon-Carbon Materials," Report No. SAMSO-TR-74-164, Aerospace Corporation, El Segundo, California, June 1974.
25. Kotlensky, W. V., "Carbon/Carbon Substrates for Throat Inserts of Solid Propellant Rocket Nozzles," Report No. AFML-TR-77-119, TRW Systems and Energy, Redondo Beach, California, March 1978.
26. Jones, R. M., "Modeling Nonlinear Deformation of Carbon-Carbon Composite Materials," AIAA Journal, Volume 18, August 1980, pp 995-1001.
27. Jones, R. M. and Nelson Jr., D. A. R., "A New Material Model for the Nonlinear Biaxial Behavior of ATJ-S Graphite," Journal of Composite Materials, Volume 9, January 1975, pp. 10-27.
28. Jones, R. M. and Nelson, D. A. R., Jr., "Material Models for Nonlinear Deformation of Graphite," AIAA Journal, Vol. 14, No. 6, June 1976, pp. 709-717.
29. Jones, R. M. and Starrett, H. S., "Nonlinear Deformation of a Thermally Stressed Graphite Annular Disk," AIAA Journal, Volume 15, No. 8, August 1977, pp. 1116-1122.
30. Stanton, E. L. and Kipp, T. E., "Mechanics of Two-Dimensional Nonlinear Carbon-Carbon Composite Structures and Materials," AIAA Journal, Vol. 23, No. 8, August 1985, pp. 1278-1284.
31. Stanton, E. L., and Kipp, T. E., "2-D Material Response, Volume 1," Report No. PDA TR-5567-00-02, PDA Engineering, April 1984.
32. Batdorf, S. B., "A Polyaxial Stress-Strain Law for ATJ-S Graphite," Journal of the American Ceramic Society, Vol. 59, 1976, pp. 308-312.
33. Pollock, P. B. and Sun, C. T., "A Study of Failure in 3-D Carbon-Carbon Composites," Report No. AFRPL TR-84-061, Purdue University, School of Aeronautics and Astronautics, May 1984.
34. Ramberg, W. and Osgood, W. R., "Description of Stress-Strain Curves by Three Parameters," NACA Technical Note Number 902, National Advisory Committee for Aeronautics, July 1943.
35. Waeber, K. R. and Hagen, J. C., "A Review of Damage Mechanisms and Failure Theories for 3-D Carbon-Carbon Composite Material, Memo No. ANSP-185, Johns Hopkins University Applied Physics Laboratory, July 1980.
36. Waeber, K. R. and Hagen, J. C., "The Wu-Tsai Failure Criteria Applied to a 3-D Orthogonal Weave Carbon-Carbon Composite Material," Memo No. ANSP-186, Johns Hopkins University Applied Physics Laboratory, July 1980.

37. Adams, D. F. and Tsai, S. W., "The Influence of Random Filament Packing on the Transverse Stiffness of Unidirectional Composites," Journal of Composite Materials, Vol. 3, July 1969, pp. 368-381.
38. Adams, D. F. and Doner, D. R., "Longitudinal Shear Loading of a Unidirectional Composite," Journal of Composite Materials, Vol. 1, January 1967, pp. 4-17.
39. D. A. Crane and Adams, D. F., "Finite Element Micromechanical Analysis of a Unidirectional Composite Including Longitudinal Shear Loading," Report No. UWME-DR-101-101-1, Department of Mechanical Engineering, University of Wyoming, February 1981.
40. A. K. Miller and D. F. Adams, "Micromechanical Aspects of the Environmental Behavior of Composite Materials," Report No. UWME-DR-701-111-1, Department of Mechanical Engineering, University of Wyoming, January 1977.
41. A. K. Miller and D. F. Adams, "Hygrothermal Microstresses in a Unidirectional Composite Exhibiting Inelastic Material Behavior," Journal of Composite Materials, Vol. 11, No. 3, July 1977, pp. 285-299.
42. Richard, R. M. and Blacklock, R. J., "Finite Element Analysis of Inelastic Structures," AIAA Journal, Vol. 7, No. 3, March 1969, pp. 432-438.
43. Repnau, T. and Adams, D. F., "High Performance Composite Materials for Vehicle Construction: A Finite Element Computer Program for Elastoplastic Analysis of Crack Propagation in a Unidirectional Composite," Report No. R-1070-PR, The Rand Corporation, Santa Monica, California, March 1973.
44. Adams, D. F., "Elastoplastic Crack Propagation in a Transversely Loaded Unidirectional Composite," Journal of Composite Materials, Vol. 8, January 1974, pp. 38-54.
45. Adams, D. F., "Practical Problems Associated with the Application of the Finite Element Method to Composite Material Micromechanical Analysis," Fibre Science and Technology, Vol. 7, No. 2, April 1974, pp. 111-122.
46. Adams, D. F., "A Micromechanical Analysis of Crack Propagation in an Elastoplastic Composite Material," Fibre Science and Technology, Vol. 7, No. 4, October 1974, pp. 237-256.
47. Murphy, D. P. and Adams, D. F., "Energy Absorption Mechanics During Crack Propagation in Metal Matrix Composites," Report No. UWME-DR-901-103-1, Department of Mechanical Engineering, University of Wyoming, October 1979.

48. Adams, D. F. and Murphy, D. P., "Analysis of Crack Propagation as an Energy Absorption Mechanism in Metal Matrix Composites," Report No. UWME-DR-101-102-1, Department of Mechanical Engineering, University of Wyoming, February 1981.
49. Cilensek, R. F., "Analytical/Experimental Correlations of the Mechanical Properties of Unidirectional Composite Materials," Unpublished work, Department of Mechanical Engineering, University of Wyoming, 1984.
50. Hinton, E. and Owen, D. R. J., Finite Element Programming, Academic Press, New York, 1977.
51. Monib, M. M. and Adams, D. F., "Three-Dimensional Elastoplastic Finite Element Analysis of Laminated Composites," Report No. UWME-DR-001-102-1, Department of Mechanical Engineering, University of Wyoming, November 1980.
52. Adams, D. F., Ramkumar, R. L., and Walrath, D. E., "Analysis of Porous Laminates in the Presence of Ply Drop-Offs and Fastener Holes," Report No. NOR-84-113, Northrop Corporation, May 1984.
53. Hill, R., The Mathematical Theory of Plasticity, Oxford University Press, London, England, 1950.
54. Furray, M. J., Variational Calculus in Science and Engineering, McGraw-Hill Book Co., New York, 1968.
55. Zimmerman, R. S., Adams, D. F., and Walrath, D. E., "Investigation of the Relations Between Neat Resin and Advanced Composite Mechanical Properties," Report No. UWME-DR-301-101-1, Volumes 1 and 2, Department of Mechanical Engineering, University of Wyoming, May 1983.
56. Zimmerman, R. S. and Adams, D. F., "Mechanical Properties Testing of Candidate Polymer Matrix Materials for Use in High Performance Composites," Report No. UWME-DR-401-104-1, Department of Mechanical Engineering, University of Wyoming, August 1984.
57. Adams, D. F., Zimmerman, R. S., and Odom, E. M., "Polymer Matrix and Graphite Fiber Interface Study," Report No. UWME-DR-501-102-1, Department of Mechanical Engineering, University of Wyoming, June 1985.
58. Hercules, Inc., "Magnamite Graphite Fibers," Manufacturers Data Sheet, 1978.
59. Lowe, D. L., "Carbon/Graphite Yarn Characterization and Carbon-Carbon Constituent Sensitivity Study," Final Report No. 76S DR 2329, General Electric Company, July 1976.

60. Marinick, W. and Rozploch, F., "Measurement of the Radial Thermal Expansion Coefficient of Carbon Fibres," High Temperatures. High Pressures, Vol. 1, pp. 709-710.
61. Jortner, J., "Multiaxial Behavior of ATJ-S Graphite," Report No. AFML-TR-71-170, McDonnell Douglas Corporation, October 1973.
62. Starrett, H. S. and Pears, C. D., "Probable and Average Properties of ATJ-S (WS) Graphite," Report No. AFML-TR-73-14, Volume 1, Southern Research Institute, February 1973.
63. Blakeslee, O. L., Proctor, D. G., Seldin, E. J., Spence, G. B. and Weng, T., "Elastic Constants of Compression-Annealed Pyrolytic Graphite," Journal of Applied Physics, Vol. 4, No. 8, July 1970, pp. 3373-3382.
64. Zimmer, J. E. and Weitz, R. L., "Disclinations in Carbon-Carbon Composites," Report No. TR-82-24/ATD, Acurex Corporation, Aerotherm Division, September 1982.
65. Zimmer, J. E., and Weitz, R. L., "Disclinations in Carbon-Carbon Composites," Report No. TR-83-21/ATD, Acurex Corporation, Aerotherm Division, September 1983.
66. Zimmer, J. E. and Weitz, R. L., "Disclinations in Carbon-Carbon Composites," Report No. TR-84-17/ATD, Acurex Corporation, Aerotherm Division, September 1984.
67. Peng, T. C., "Oxidation Effects on the Tensile Strength of ATJ-S Graphite and Vitreous Carbon," Carbon, Vol. 17, 1979, pp. 157-174.
68. Feldman, L. A., "Creep of Carbon Yarns and Composites at High Temperature," Report No. TR-0084 (4728-02)-1, Aerospace Corporation, December 1983.
69. Feldman, L. A., "High Temperature Creep of Carbon Yarns: Second Annual Report," Report No. TOR-0084A(5728-02)-1, Aerospace Corporation, July 1985.
70. Quan, D., Sines, G., and Batdorf, S. B., "The Effects of Radial Yarns - Three-Dimensionally Reinforced Carbon-Carbon Composites," Report No. UCLA-ENG-84-22, University of California at Los Angeles, July 1984.
71. Deviney, M. L. and O'Grady, T. M., Petroleum Derived Carbons, American Chemical Society, Washington, D. C., 1976.
72. Mantell, C. L., Carbon and Graphite Handbook, Wiley Interscience, New York, 1968.
73. Tsai, S. E., "Strength Theories of Filamentary Structures," in Schwartz, R. T. and Schwartz, H. S. (eds.), Fundamental Aspects of Fiber Reinforced Plastic Composites, Wiley Interscience, New York, 1968.

74. Sines, G., Batdorf, S. B., Kuhansedgh, B. J. and Ghaffarian, R.,
"Damage Mechanisms and Modeling of Carbon-Carbon Composites,"
Report No. UCLA-ENG-81-26, University of California at Los Angeles,
September 1981.